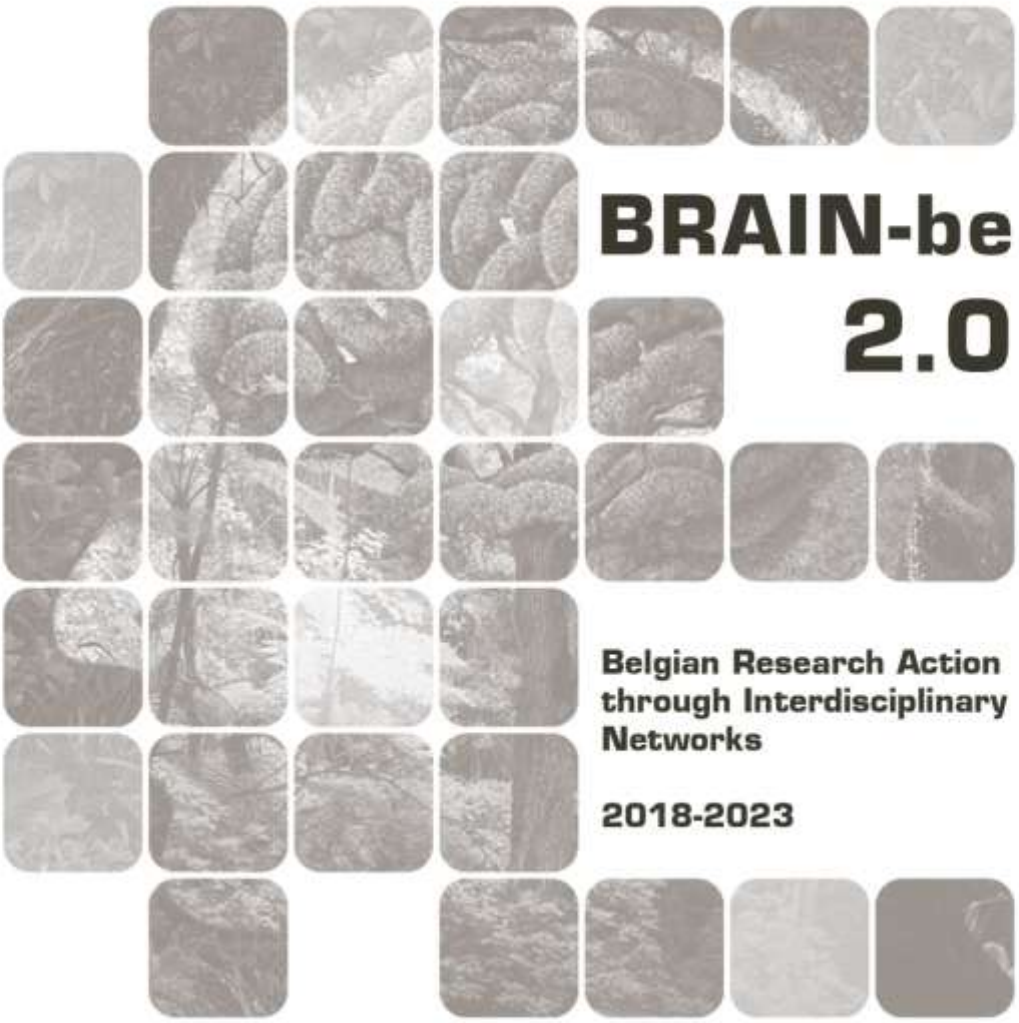

OUTFLOW

Quantifying the cOntribUTion of Fouling fauna to the Local carbon budget of an Offshore Wind farm

Jan Vanaverbeke (RBINS) – Samuel Bodé (UGent) – Pascal Boeckx (UGent) - Ulrike Braeckman (RBINS - UGent) - Esther Cepeda Gamella (RBINS – UGent) - Arthur Capet (RBINS - ULB) -Emil De Borger (UGent) – Geneviève Lacroix (RBINS) – Ivan Lizaga (UGent - IPE-CSIC) - Dries Van den Eynde (RBINS)

belspo .be

NETWORK PROJECT

OUTFLOW

Quantifying the cOntribUTion of Fouling fauna to the Local carbon budget of an Offshore Wind farm

Contract - B2/212/P1/OUTFLOW

FINAL REPORT

PROMOTORS: Jan Vanaverbeke (RBINS)
Pascal Boeckx (UGent)
Ulrike Braeckman (UGent)

AUTHORS: Jan Vanaverbeke (UGent)
Samuel Bodé (UGent)
Pascal Boeckx (UGent)
Ulrike Braeckman (RBINS - UGent)
Esther Cepeda Gamella (RBINS – UGent)
Arthur Capet (RBINS-ULB)
Emil De Borger (UGent)
Geneviève Lacroix (RBINS)
Ivan Lizaga (UGent - IPE-CSIC)
Dries Van den Eynde (RBINS)

Published in 2026by the Belgian Science Policy Office
WTCIII
Simon Bolivarlaan 30 bus 7
Boulevard Simon Bolivar 30 bte 7
B-1000 Brussels
Belgium
Tel: +32 (0)2 238 34 11
http://www.belspo.be
http://www.belspo.be/brain-be

Contact person: Koen Lefever
Tel: +32 (0)2 238 35 51

Jan Vanaverbeke (UGent); Samuel Bodé (UGent); Pascal Boeckx (UGent); Ulrike Braeckman (RBINS - UGent); Esther Cepeda Gamella (RBINS – UGent); Arthur Capet (RBINS-ULB); Emil De Borger (UGent); Geneviève Lacroix (RBINS); Ivan Lizaga (UGent - IPE-CSIC); Dries Van den Eynde (RBINS) - ***Quantifying the cOntribUTion of Fouling fauna to the Local carbon budget of an Offshore Wind farm***. Final Report. Brussels: Belgian Science Policy Office 2026 – xx p. (BRAIN-be 2.0 - (Belgian Research Action through Interdisciplinary Networks))

TABLE OF CONTENTS

ABSTRACT

The OUTFLOW project aimed at increasing the understanding of carbon cycling within and beyond the scale of an offshore wind farm. This report therefore provides an integrated, field-validated, and model-supported assessment of how fouling fauna on offshore wind turbines alter carbon dynamics in and around offshore wind farms (OWFs) in the Belgian Part of the North Sea. Our results reveal that fouling communities create novel trophic pathways that channel water-column production to the seafloor, leading to localised increases in benthic organic matter and measurable changes in food-web structure. However, the fast mineralisation processes in permeable sediments and the dynamic hydrodynamic environment strongly limit long-term carbon storage. While OWFs induce clear ecological and biogeochemical effects at the scale of individual turbines and wind farms, our upscaling efforts suggest a relatively modest broader regional effect on carbon cycling. The findings highlight the importance of considering both physical sediment properties and hydrodynamic processes when assessing the potential of OWFs to influence carbon cycling or contribute to carbon storage.

1. INTRODUCTION

In order to meet the global targets set by the *Paris Agreement,* there is a need to accelerate the transition toward renewable energy sources. Offshore wind energy is expected to play a pivotal role in achieving these goals. By mid-2025, approximately 83 GW of offshore wind capacity was installed worldwide, with projections indicating an additional 441 GW to be developed by the end of 2034 (Williams et al. 2025).

Also in Belgium, offshore wind energy development has contributed to the national renewable energy policy. Currently, the eastern part of the Belgian part of the North Sea (BPNS) hosts nine operational offshore wind farms within a single designated wind farm zone, comprising 399 turbines with a total installed capacity of 2.26 GW (Belgian Federal Public Service Economy 2025). To further expand offshore renewable capacity, the Princess Elisabeth Zone—Belgium's second offshore wind farm area—was designated, with an expected additional capacity of 3.1 to 3.5 GW upon completion.

There is now substantial field-based evidence on the local ecological effects of offshore wind farms on the marine ecosystem. Studies consistently report the development of diverse and abundant colonising communities on turbine foundations, accompanied by changes in soft-sediment benthic assemblages in the surrounding areas (summarised in Degraer et al 2020 and Coolen et al 2022). In addition, increased densities of certain fish species (cod, pouting, plaice) in and around operational wind farms (Reubens et al 2014, Mavraki et al 2021, Buyse et al 2022). For some species (plaice, cod, pouting...) this was explained by the enhanced availability and long-term consumption of food resources associated with the fouling community, combined with the additional shelter and resting space created by the scour protection layer (Buyse et al 2022).

These ecological changes have functional consequences, as the presence of the fouling fauna drives a marked shift toward a strong dominance of suspension feeders. These organisms filter large volumes of seawater (7.5 Olympic swimming pools per day, Voet et al 2022). These arguments also produce substantial quantities of faecal pellets(FP) that are returned to the water column (Mavraki et al 2022) . Current hypotheses propose that these pellets are deposited on the sediment near the turbines, resulting in local organic enrichment. Such enrichment may alter biogeochemical processes and, ultimately, benthic ecosystem functioning in the areas surrounding offshore wind structures.

While some observations indeed reflect an enrichment of the sediment in the vicinity of the turbines (Coates et al 2014, Lefaible et al 2023), quantitative information on the importance and fate of this 'faecel pellet' carbon source in the water column, sediment and faunal groups is lacking to date. OUTFLOW therefore set out to (1) develop and apply the methodology needed to quantify the contribution of different source of organic matter to the total OM pool; (2) follow the potential incorporation of FPs in the benthic food web; (3) describe the biogeochemical processes involved in mineralisation processes in sediments surrounding the turbines on the BPNS; (4) characterise the 'C' footprint of a single turbine and quantify the C-content within that area (5); and upscale the effects of the presence of OWF on marine ecosystem functioning at larger scales.

2. STATE OF THE ART AND OBJECTIVES

It is now widely recognized that the presence of offshore wind turbines, and the abundant communities of suspension-feeding organisms colonising the foundations, significantly alter local carbon processing pathways. Laboratory studies have demonstrated that these epifaunal organisms exploit food resources derived from the water column (Voet et al. 2022, Mavraki et al. 2020), partly converting this material into large quantities of faecal pellets (Mavraki et al. 2022), representing an efficient mechanism for transforming suspended organic matter into rapidly sinking particulate material that ultimately can be deposited on offshore wind farm sediments.

Building on these observations, several modelling studies have explored system-level consequences. These models predict effects on regional primary production (Slavik et al. 2019; Daewel et al. 2022), enhanced deposition of organic matter within offshore wind farms (Ivanov et al. 2021), leading to elevated carbon content in offshore wind farm sediments (De Borger et al. 2021). However, these models remain unvalidated due to the absence of suitable field-based quantification data methods and robust upscaling frameworks. Hence, the link between modelled projections and real-world biogeochemical functioning remains weak.

OUTFLOW project objectives

OUTFLOW aims to resolve this knowledge gap by improving our understanding of how offshore wind farms influence carbon dynamics at both local (individual turbine / wind farm) and broader spatial scales (Belgian Part of the North Sea and potentially the wider southern North Sea). The project will integrate ecological, biogeochemical, and modelling approaches to provide an evidence-based assessment of how carbon cycling is affected by the presence of OWF.

From an **ecological perspective**, OUTFLOW builds directly on field data obtained through the BELSPO-funded FaCE-It project. A food-web analytical framework (Linear Inverse Modelling) will be employed to compare carbon pathways and trophic linkages in offshore wind farm areas with those in reference sites where no turbines are present. This approach will further support the estimation of carbon accumulation in OWF sediments. In addition, experimental work allows to quantify the uptake of deposited faecal pellets produced by turbine inhabiting organisms, to quantify the integration of this additional food source into the local benthic food web.

From a **biogeochemical standpoint**, the project includes the development and application of tracers through stable isotope analysis of amino acids derived from faecal pellets of dominant organisms and zoo- and phytoplankton. This will enable us to estimate the proportional contribution of faecal pellet derived organic matter in the total organic matter pool of the water column within an OWF. Vertical biogeochemical profiles measured in OWF sediments are used in sediment diagenetic models to elucidate mineralisation processes and therefore enhance our understanding of the mechanism driving potential C accumulation in these sediments.

The **modelling component** of OUTFLOW begins with characterizing the faecal pellets (sinking rates, carbon content, production rates) produced by the dominant species living on turbine structures. These lab-derived parameters are incorporated into mechanistic particle-tracking models to predict the deposition footprint—both in magnitude and spatial extent—of faecal pellets around individual turbines. The final stage of the modelling analysis integrates these deposition simulations with

ecological observations and sediment measurements to produce the first estimates of carbon content and accumulation around a single turbine.

Upscaling is achieved through a combination of field-based measurements and modelling frameworks. For the first time ever, both water columns and phytoplankton data were collected simultaneously within and outside the cross-border offshore wind farm zone at the Belgian-Dutch border to investigate whether the modelled effects on phytoplankton can be valorised using field data collected over sufficiently large scale. A 3D biogeochemical upscaling model experiment is also applied at the scale of a wind farm, i.e. resolving spatial scales from 500m to 40km. This unique experiment integrates tidal flow dynamics, pelagic and benthic biogeochemistry, as well as the biofouling filtration and defecation activities and its impact on low-trophic level ecosystem processes (i.e. plankton, detrital loop).

As such, OUTFLOW contributes to

1. The quantification of the effects of OWF on local food-web dynamics
2. The development of cutting-edge methodology to disentangle the composition of bulk organic matter samples
3. The quantification of the organic matter derived from turbine inhabiting organisms
4. The spatial delineation of the C-footprint of a single turbine
5. The quantification of the C-accumulation potential of OWF sediments
6. The validation of model predictions on the effect of OWF on phytoplankton dynamics
7. Detailing the intricacy of the ecological processes at play that sets the net response of the carbon system to OWF induced perturbations at wind farm scale.

3. METHODOLOGY

3.1 Food web methodology

We investigated the food web of an offshore wind farm to understand (1) alterations to local carbon cycling due to the addition of hard substrate species in the food web, (2) functioning of the artificial OWF food web compared to natural food webs in the vicinity, and (3) potential secondary production of fish species. To do this, we used a linear inverse model (LIM) (Soetaert & van Oevelen, 2009; van Oevelen et al. 2010), a flexible modelling framework in which several data types can be implemented, and which results in estimates of the carbon flows between different food web components. This food web can also be used to calculate food web indices, indices based on food web properties that inform about a food web's properties (e.g. stability, connectance) and functioning (e.g. carbon throughput, internal carbon cycling) (Kones et al. 2009).

a. Study area

The specific OWF food web that was modelled was focused around the "C-Power" wind farm (51 32.88 N 2 55.77 E). The food web here describes the species present on the turbine and surrounding suspension protection layer (SPL), and the surrounding soft sediment, which interact with each other depending on the species. Besides the OWF food web, we also constructed food webs of nearby locations: Coarse, a coarse sandy food web typical for sand banks of the Southern Bight, and Fine, a fine sandy sediment location with a rich macrofaunal community Figure 1 (A). The two natural food webs consist only of soft sediments and are therefore straightforward to represent model-wise (the food web is represented as carbon flows per m^{-2} of soft sediment). The OWF food web consists of a proportion of turbine, SPL, and soft sediment each, which were scaled to one m^2 of food web according to the actual surface areas shown in Figure 1 (B).

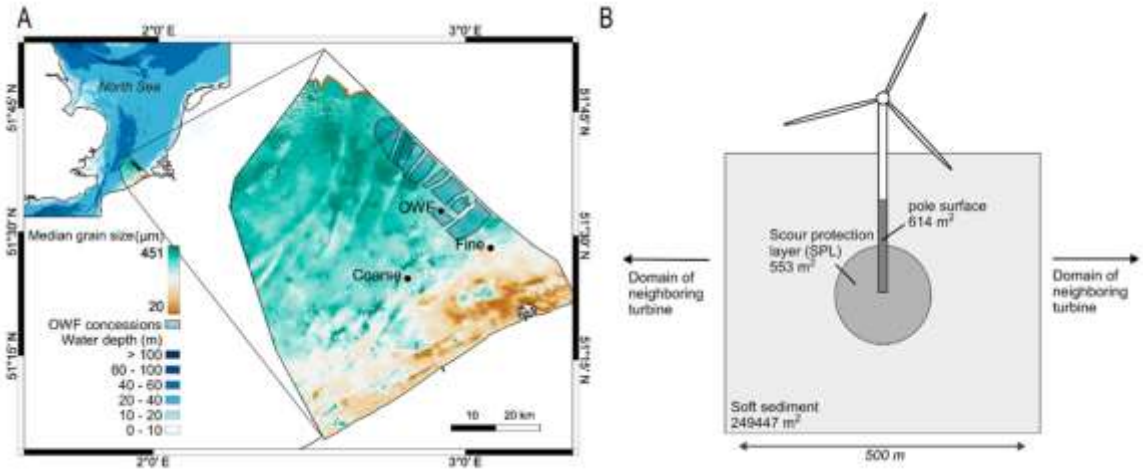

Figure 1 Study domain (A) Location of the three study sites "Coarse" – "Fine" – "OWF" in the Belgian Part of the North Sea, showing median grain size in the study area, and bathymetry in the region (inset bathymetry: GEBCO, 2023, grain size: Verfaille et al.). (B) Structure of the OWF food web unit (grey surfaces) and indication of the surfaces over which species biomass is standardized to m^2. Figure adopted from De Borger et al, 2025).

b. Data availability

In the BELSPO-funded FaCE-It project, extensive sampling of faunal communities was performed, resulting in the availability of abundance and biomass of macrofauna in the soft sediments surrounding the turbine and in the Coarse and Fine food web, values of organic carbon present as detritus in the water column (suspended particulate organic matter) and in the seafloor (sedimentary organic matter), water column chlorophyll a concentrations (to estimate phytoplankton biomass), respiration rates of the sediment community (bacteria + fauna), and isotopic compositions ($\delta^{15}N$) of the majority of food web components - macrofauna, fish species, and organic matter pools in the different individual food webs. Part of these data have previously been reported (Mavraki et al. 2020, 2021; Toussaint et al. 2021). This initial dataset was expanded with fish stock data from trawl fishing available through the WinMon.BE project and provided by ILVO. Literature data was used where needed to complete information on zooplankton biomass, jellyfish biomass, densities and biomass of hard-substrate species, bacterial biomass in water column and sediment, isotopic compositions, and predator prey relations.

c. Linear Inverse Models

We used Linear Inverse Models (LIMs) to estimate unknown carbon flows (mmol C m^{-2} d^{-1}) between food web components. These flows were constrained by observational data described above—biomass stocks, isotopic compositions ($\delta^{15}N$), and literature-derived physiological bounds. In this modelling approach, the food web is expressed as a system of linear equations and inequalities:

$$Ax = b$$

$$Gx \geq h$$

where *x* is a vector of unknown flows. The matrix *A* represents mass-balance and data constraints, while G and *h* define biological limits such as production, assimilation, and respiration rates based on realistic ranges extracted from literature. Whereas all potential trophic interactions between model components are extracted from literature and coded into the model *a priori*, we used isotopic data to constrain realized prey–predator relationships.

Respiration was included for each functional group to calculate biomass production, using the relationship:

$$r = 0.017W^{0.156}$$

where *r* is the biomass-specific respiration rate (d^{-1}) and *W* is the individual biomass (mg C ind^{-1}). We multiplied *r* by species biomass to obtain total respiration (*R*, mmol C m^{-2} d^{-1}), setting lower and upper limits at 0.75×*R* and 1.25×*R*. For fish, we used $r = 0.01$ d^{-1}.

We further constrained total benthic respiration using measured sediment community oxygen consumption (SCOC) from the study sites. This ensured that the sum of macrofaunal and bacterial respiration matched observed oxygen use. Additional inequality constraints for bacterial growth efficiency and faunal assimilation and production efficiencies were taken from the literature.

We solved the underdetermined system (the number of equations was less than the number of flows to be estimated) using least-distance optimization, minimizing the sum of squared flow values to obtain a parsimonious initial solution. We then used this solution to initialize a Markov Chain Monte

Carlo (MCMC) simulation that generated 10,000 possible flow combinations satisfying all constraints. From these, we calculated the mean and standard deviation for each flow. Model convergence was reached after ~2,000 iterations, indicating stability of the solution space.

All LIMs were implemented in R using the *LIM* package (van Oevelen et al. 2010), with the MCMC simulations run on the high-performance computing (HPC) cluster at the Royal Netherlands Institute for Sea Research (NIOZ).

3.2. Faecal pellet marker development

a. Strategy

Offshore industrial development, including wind farms and aquaculture, has largely increased the presence of suspension feeders on artificial structures. These organisms release large amounts of faecal pellets (FP), which can contribute significantly to the surrounding organic matter (OM). However, it is still unclear how much FP is added to the local OM pool, mainly because it is difficult to distinguish FP from natural sources such as phyto- and zooplankton. To address this problem, Compound-Specific Stable Isotope Analysis of Amino Acids (CSIA-AA) was tested as a potential method for identifying and quantifying OM sources. CSIA-AA provides detailed information on nitrogen isotope ratios in individual amino acids (AA), which can be used to trace material through food webs. Although the technique is considered promising , it has not yet been thoroughly tested for complex systems like those around offshore wind farms (OWF), where bulk OM is composed of several overlapping sources.

The artificial mixtures were designed to test and validate this method under controlled conditions. Known amounts of FP from *Mytilus edulis* and *Metridium senile*, together with representative phyto- and zooplankton material, were combined in specific carbon-based proportions. This setup allowed direct comparison between measured isotope signals and known mixture compositions. The main goal was to evaluate how accurately CSSI-AA can identify and quantify the contribution of each source, and to determine which amino acids are most reliable for tracing OM in complex environments. This controlled approach provides a foundation for applying the method to real-world offshore sites and for improving our understanding of how man-made structures influence carbon cycling in marine ecosystems.

b. Faecal pellets of species of interest

FP from the dominant fouling species *Mytilus edulis*, *Metridium senile*, and *Jassa herdmani* associated with offshore wind turbine structures were collected for analysis. Specimens of *M. edulis* and *M. senile* were obtained from turbine foundations by scientific divers or via moorings during 2022. After collection, organisms were maintained in oxygenated seawater at ambient temperature and transported rapidly to the laboratory to minimize stress.

In the laboratory, individuals were incubated in a custom flow-through system supplied with natural seawater collected either concurrently with the specimens or from offshore locations (>30 km) to replicate offshore wind farm conditions (Fig. 2). Each species was housed separately in an upper tank connected to a lower reservoir, ensuring continuous circulation through a pump and gravity flow. Prior to incubation, all specimens were cleaned and allowed to acclimate for 24 h. Fresh FP were collected daily for five consecutive days using a Pasteur pipette, centrifuged, and stored at −80 °C. Tanks were

cleaned and seawater replenished between collections. All FP samples were then freeze-dried for 24 h and stored in a desiccator until further analysis.

Phytoplankton samples were collected on 29 June 2022 using Niskin bottles from depths of −5 m, −10 m, and −20 m. Water from each depth was filtered through Ø47 mm pre-combusted, pre-weighed glass fibre filters (GF/F, 0.7 µm pore size). The filters were immediately frozen on board at −20 °C and later transferred to a −80 °C freezer upon return to the laboratory. Samples were subsequently lyophilized and stored in a desiccator. Zooplankton samples were collected on 4 June 2022 using a WP2 net (200 µm mesh, 1 L cod end). Samples were rinsed, divided into 50 ml tubes, frozen, lyophilized, homogenized, and stored under the same conditions.

All FP, phytoplankton, and zooplankton samples were analysed to characterize the isotopic signatures of each organic matter source and to prepare controlled artificial mixtures. These baseline data were essential for identifying source contributions and evaluating organic matter composition in both experimental and field samples. *Jassa herdmani* was not included in the artificial mixtures due to limited sample availability; however, material collected from this species was still analysed to support signal identification and to compare its isotopic characteristics with those of natural OM.

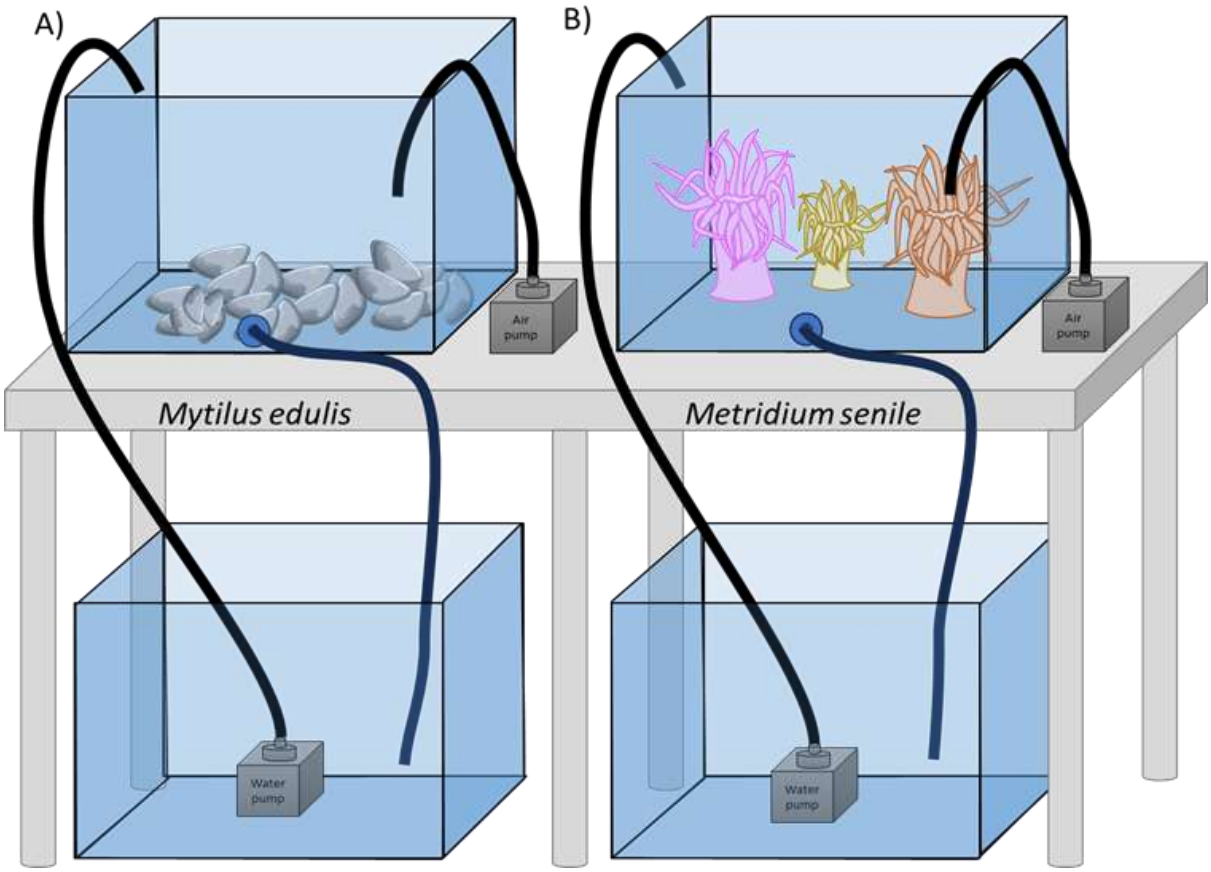

Figure 2. Incubation setup. Water was circulated from the lower to upper tank via a pump and returned by gravity through a plastic tube. All upper tanks were oxygenated. A) Mytilus edulis and B) Metridium senile.

c. Artificial Mixtures

Lyophilised FP and zooplankton samples were gently homogenised using a mortar and pestle. For phytoplankton samples, carbon content was determined from two replicate measurements using glass fibre filters, and the mean value was used as the reference. Carbon content was quantified for each source material to allow the preparation of artificial mixtures based on carbon contribution rather than mass (Table 1). This approach reflects the focus on carbon fluxes and accounts for substantial variability in carbon content among individual samples of the same type. The artificial dataset comprised 16 mixtures composed of two (n = 4), three (n = 11), or four (n = 1) sources. In two-source mixtures, each component contributed equally (50% of the total carbon content). Three-source mixtures included configurations with either one dominant source contributing 60% or 80% of the carbon and two minor sources contributing equally to the remainder, or equal contributions from all three sources (33% each). The single four-source mixture consisted of equal carbon contributions (25% each) from all sources. Each mixture was assigned a standardized label (e.g., Mx_25|25|25|25), where the numbers indicate the percentage contribution of each source in a fixed order: FP *Mytilus* (light blue), FP *Metridium* (coral red), zooplankton (dark blue), and phytoplankton (green). This consistent ordering corresponds to both the layout and colour coding used in Fig. 3, facilitating direct visual interpretation of mixture composition.

Table 1. Composition and carbon-based mass allocation of 16 artificial mixtures combining FP Mussel (light blue), FP 3 Metridium (coral red), phytoplankton (green) and zooplankton (dark blue). For each mixture, targeted carbon contribution (%) and corresponding sample mass (mg) are shown, along with total mixture mass and %C content of each source. Subscripts denote 5 replicate mixtures.

Mixture	Contributing sources									Total mass mixture (mg)
	Mass C measured (%)	10.07		5.83		7.85		11.28		
	n = number of sources	FP Mussel		FP Metridium		Phytoplankton		Zooplankton		
		Actual C basis taken (%)	Mass picked (mg)	Actual C basis taken (%)	Mass picked (mg)	Actual C basis taken (%)	Mass picked (mg)	Actual C basis taken (%)	Mass picked (mg)	
Mx_|--|50|--|50_|	n = 2	-	-	49.9	13.16	-	-	50.27	6.85	20.01
Mx_|50|--|50|--|	n = 2	50.03	5.69	-	-	50	7.25	-	-	12.94
Mx_|50|--|--|50|	n = 2	49.69	10.5	-	-	-	-	49.28	9.3	19.8
Mx_|50|50|--|--|	n = 2	49.85	7.31	50.14	12.7	-	-	-	-	20.01
Mx_|--|20|60|20|	n = 3	-	-	20.18	3.56	60	7.86	20.64	1.88	13.3
Mx_|20|20|--|60|	n = 3	20.15	3.73	19.68	6.29	-	-	59.34	9.8	19.82
Mx_|60|20|--|20|	n = 3	59.7	10.62	20	6.15	-	-	20.4	3.24	20.01
Mx_|10|10|--|80|	n = 3	10.17	2.06	10.15	3.55	-	-	79.3	14.35	19.96
Mx_|10|80|--|10|	n = 3	9.95	1.27	79.75	17.53	-	-	9.73	1.11	19.91
Mx_|80|--|10|10|	n = 3	80.02	45.91	-	-	10	7.36	10.02	5.13	58.41
Mx_|80|10|--|10|	n = 3	80.17	15.09	10.26	3.34	-	-	9.62	1.62	20.05
Mx_|33|33|33|--|	n = 3	32.64	5.41	33.05	9.45	33	7.01	-	-	21.87
Mx_|33|33|--|33|_1	n = 3	33.04	5.53	33.05	9.56	-	-	33.23	4.97	20.06
Mx_|33|33|--|33|_2	n = 3	32.98	5.52	32.74	9.47	-	-	32.81	4.9	19.89
Mx_|33|33|--|33|_3	n = 3	33	5.52	32.98	9.54	-	-	32.99	4.93	19.99
Mx_|25|25|25|25|	n = 4	25.03	5.81	25.6	10.29	25	7.44	25.07	5.19	28.73

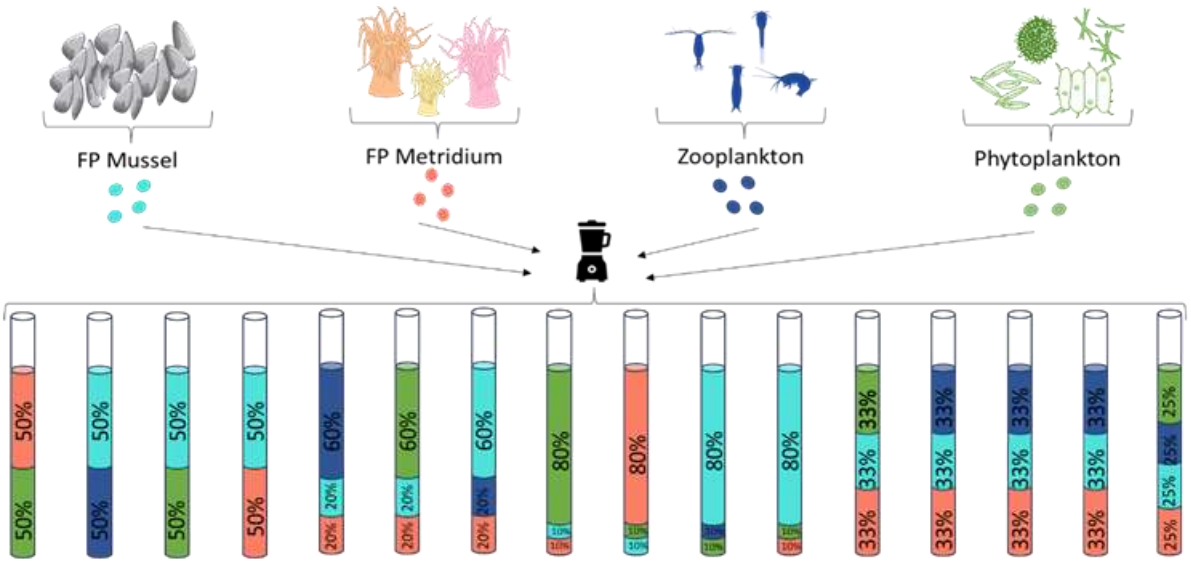

Figure 3. Artificial mixture diagram. Each tube represents one of the 16 mixtures prepared using carbon-based proportions of up to four sources: FP Mussel (light blue), FP Metridium (coral red), zooplankton (dark blue), and phytoplankton (green).

d. Extraction of Amino Acids

Lyophilized samples of individual endmembers and artificial mixtures were processed following a 3-step AA extraction protocol (Popp *et al.*, 2007; Hannides *et al.*, 2009, 2013, 2020). Two reference materials fish muscle tissue (*Salmo salar*) and a mixture of 13 pure AA (Ala, Asp, Glu, Gly, Ile, Leu, Lys, Phe, Pro, Ser, Thr, Tyr and Val), each at 1 µmol N were included. Nor-leucine (1 µmol) was added as a recovery standard. Samples were hydrolysed in 1 ml 6 M HCl at 150 °C for 70 min under N_2. After drying (60 °C, N_2 stream), they were resuspended in 0.01 M HCl and filtered (0.20 µm polyamide filter, CHROMAFIL Xtra PA-20/25, Macherey-Nagel GmbH & Co., Germany). AA were purified via cation exchange (1 g of a cation-exchange resin; Dowex 50WX8form 100 – 200 mesh) solid phase extraction (SPE) columns (pre-rinsed with 0.01 M HCl) and eluted with 4 ml 2 M NH_4OH. The eluate was dried (80 °C, N_2), re-acidified (0.2 M HCl), heated (100 °C, 5 min), and evaporated again. Derivatization to N-acetyl-n-propyl (NAP) forms involved esterification (isopropanol: acetyl chloride, 4:1) and acetylation (methylene chloride: trifluoroacetic anhydride (TFAA), 3:1). Derivatives were purified by solvent extraction with chloroform: P-buffer (0.422 M KH_2PO_4 + 0.578 mol L-1 Na_2HPO_4 in ultrapure water water) (1:2), centrifuged, and dried. Final NAP derivatives were stored in methylene chloride: TFAA (3:1) at –20 °C and redissolved in ethyl acetate prior to analysis.

The δ^{15}N-AA values of individual AA were determined using GC-c-IRMS. The GC (Trace 1310 GC, Thermo Scientific, Bremen, Germany) was equipped with a PTV injector and a GC column containing 5% Phenyl-methylpolysiloxane (DB5-MS, 60 m, 0.25 mm, 0.5 µm, Agilent, Diegem, België). Combustion was performed on a GC-ISOLINK with the combustion reactor maintained at 1000 °C; CO_2 was removed using a coil emerged in liquid nitrogen (trapped CO_2 was flushed out manually every 15 - 20 samples) and transferred via ConFlow IV to a Delta-V Advantage (Thermo Scientific). The PTV started at 50 °C, ramped to 250 °C at 10 °C/s and baked at 315 °C. The oven was held 60 °C for 1.5 min, then increased to 120 °C at 20 °C/min, 180 °C at 2 °C/min, 250 °C at 4 °C/min, and baked at 310 °C for 6 min. Derivatised AA were identified by GC-MS (Trace GC ultra - DSQ MS, Thermo Scientific) using same column and method. Prior GC-c-IRMS analysis, sample were checked on same GC-FID for quantification and solvent adjustment. All samples were run in duplicate. Normalization used three

caffeine references: USGS-61 ($\delta^{15}N$ = –2.87 ± 0.04‰), USGS-62 (+20.17 ± 0.06‰), and USGS-63 (–37.83 ± 0.06‰) vs. AIR, analysed in duplicate every 4-6 injections.

e. Tracer selection

A content-dependent unmixing approach was applied to account for differences in AA concentrations across samples, ensuring that each ^{15}N-AA tracer contributed proportionally to its nitrogen content rather than being over- or underrepresented in the unmixing model. This weighting prevented bias in source contribution estimates and provided a more realistic reflection of each tracer's abundance in the sample. For every sample, $\delta^{15}N$ values and chromatographic peak areas were obtained from replicate measurements, and the nitrogen content of each AA was calculated using Nor-leucine as an internal standard. The resulting AA-N content, expressed relative to the sample's carbon mass, was used in subsequent analyses to maintain consistency between carbon- and nitrogen-based datasets.

To identify the most reliable ^{15}N-AA tracers for distinguishing organic matter sources, three complementary, model-independent methods were applied: the Conservativeness Index (CI), Consensus Ranking (CR), and Consistency-Based Tracer Selection (CTS)(Lizaga et al. 2020a; Latorre et al. 2021). The CI method assessed each tracer's stability and conservativeness across both source and mixture datasets. CR compared the performance of each tracer across multiple random subsets, rewarding those that produced consistent results and penalising those generating divergent estimates. CTS tested all possible tracer combinations to determine which sets produced stable, low-error solutions, retaining only those with a normalised error below 5% of the tracer range. Collectively, these analyses helped detect non-conservative or inconsistent tracers and guided the selection of the most stable and reliable amino acids for unmixing.

To visualise overall tracer performance, CI, CR, and CTS results were combined into a heatmap, with classification thresholds applied to highlight general patterns across mixtures of varying complexity. However, a stricter filtering process was used for actual unmixing, retaining only amino acids that met all three selection criteria (CI > 10, CR > 70%, and CTS error ≤ 0.05). This ensured that only tracers demonstrating high conservativeness, consensus, and consistency were used in quantitative analyses.

Unmixing was performed using three complementary tracer sets: (i) previously identified AA tracers (Ala and Thr), (ii) all available AA tracers, and (iii) those selected through the CI/CR/CTS framework. Source contributions to each artificial mixture were estimated using the validated FingerPro v2 model (FingerPro v2; Lizaga et al. 2018; 2020b), which was applied progressively to mixtures of increasing complexity (two to four sources). To simulate realistic, uncertain environmental conditions, additional "virtual" endmembers with zero contribution were introduced to create overdetermined systems in which the model had to distinguish true sources from absent ones. This approach provided a robust test of the model's resolving power in complex mixing scenarios. The accuracy of unmixing results was evaluated by comparing the estimated source contributions with their known theoretical values using the Root Mean Square Error (RMSE), expressed as a percentage of deviation.

3.3 Quantification of fouling fauna derived OM in field environment

a. Sampling

The study was carried out in the Belgian part of the North Sea at turbine D5 (51°32.87952' N, 2°55.77318' E) within the C-Power offshore wind farm. This site was chosen because of its well-documented gravity-based foundation and the availability of extensive ecological data on local

biological communities. Sampling and deployment of suspended particulate matter (SPM) traps were performed aboard the research vessels *RV Simon Stevin* and *RV Belgica*.

Vertical suspended particulate matter (SPM) traps were custom-built to collect OM. Each trap consisted of a 1 m long PVC tube (Ø 125 mm) with an open top to allow particle entry, and a 3D-printed funnel (ISOFYS–UGent) attached to a 250 mL collection container filled with tap water. Two drainage outlets enabled careful removal of water before unscrewing the container, minimizing sample loss. Traps were mounted on a tripod and positioned 1 m above the sediment–water interface. Tripod-mounted traps were deployed approximately 200 m southwest of turbine D5 for periods ranging from 3 to 12 days. Four field campaigns were carried out: April (RV Simon Stevin, 27–29/04/2022), June (RV Belgica, 27–29/06/2022), July (RV Belgica, 1–13/07/2022), and October (RV Belgica, 17–21/10/2023) (Fig. 4). After retrieval, water was drained through the outlets, overflow was collected to prevent losses, and samples were stored at –20 °C. In the laboratory, material was weighed, homogenized, and divided for subsequent analyses. Half of each sample was preserved with 4% formaldehyde, and the other half was frozen at –20 °C for carbon and CSIA-AA analysis. Frozen SPM trap subsamples were treated to remove residual chlorides originating from seawater, as chloride contamination can interfere with analytical instruments. Samples were centrifuged three times with 0.01 M calcium sulphate solution (5 minutes each), and the supernatant was discarded after every run. The remaining sediment fraction was freeze-dried for 24 hours and stored at –80 °C. The same chloride-removal procedure was applied to zooplankton samples, but not to FP samples, as their collection involved negligible seawater contamination. From the freeze-dried material, 5 mg of each sample were weighed into tin cups for total carbon analysis. For organic carbon determination, 40 mg were placed into silver cups, fumigated with 37% HCl for 24 hours, freeze-dried again, and then repacked into tin cups for measurement using an Elemental Analyzer–Isotope Ratio Mass Spectrometer (EA–IRMS).

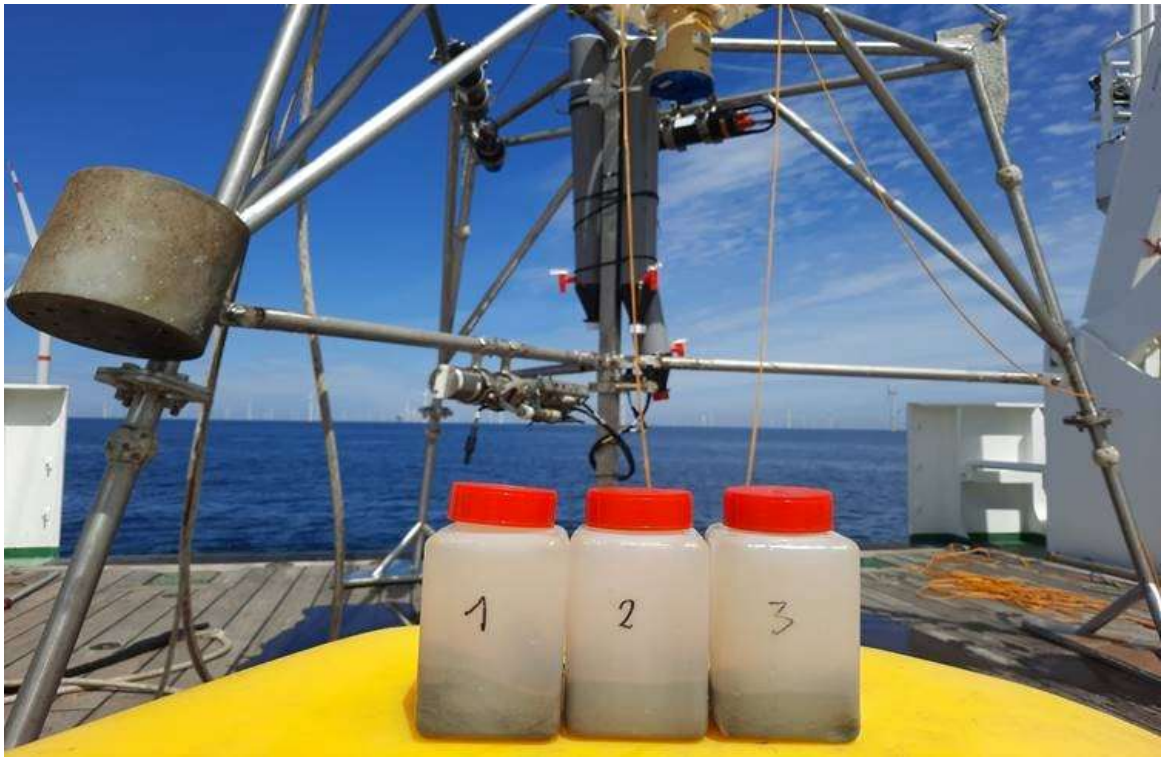

Figure 4. Sediment trap samples retrieved from the SPM trap deployed in June 2022 with RV Belgica.

Phytoplankton samples were collected on 29 June 2022 at depths of 5, 10, and 20 meters using Niskin bottles. Water was filtered through pre-combusted GF/F filters, which were then frozen, lyophilized, and stored for later analysis. Zooplankton samples were taken earlier, on 4 June 2022, with a WP2 net (200 µm mesh) and processed under similar preservation conditions. Benthic and sessile organisms (*Mytilus edulis*, *Metridium senile*, and *Jassa herdmani*) were collected from turbine foundations by divers or retrieved moorings. Specimens were transported in oxygenated seawater and acclimated in laboratory flow-through systems that replicated natural conditions. FP were collected over a five-day period, centrifuged, and stored at –80 °C. All samples were subsequently lyophilized and kept in a desiccator until analysis (Figure 5).

Samples of bulk POM from Niskin bottles were also collected on pre-combusted GF/F filters at the same time as SPMT were deployed. They were then frozen, lyophilized, and stored for later analysis.

Freeze-dried samples from individual endmembers and SPM traps were further processed using a three-step AA extraction protocol developed for artificial mixtures.

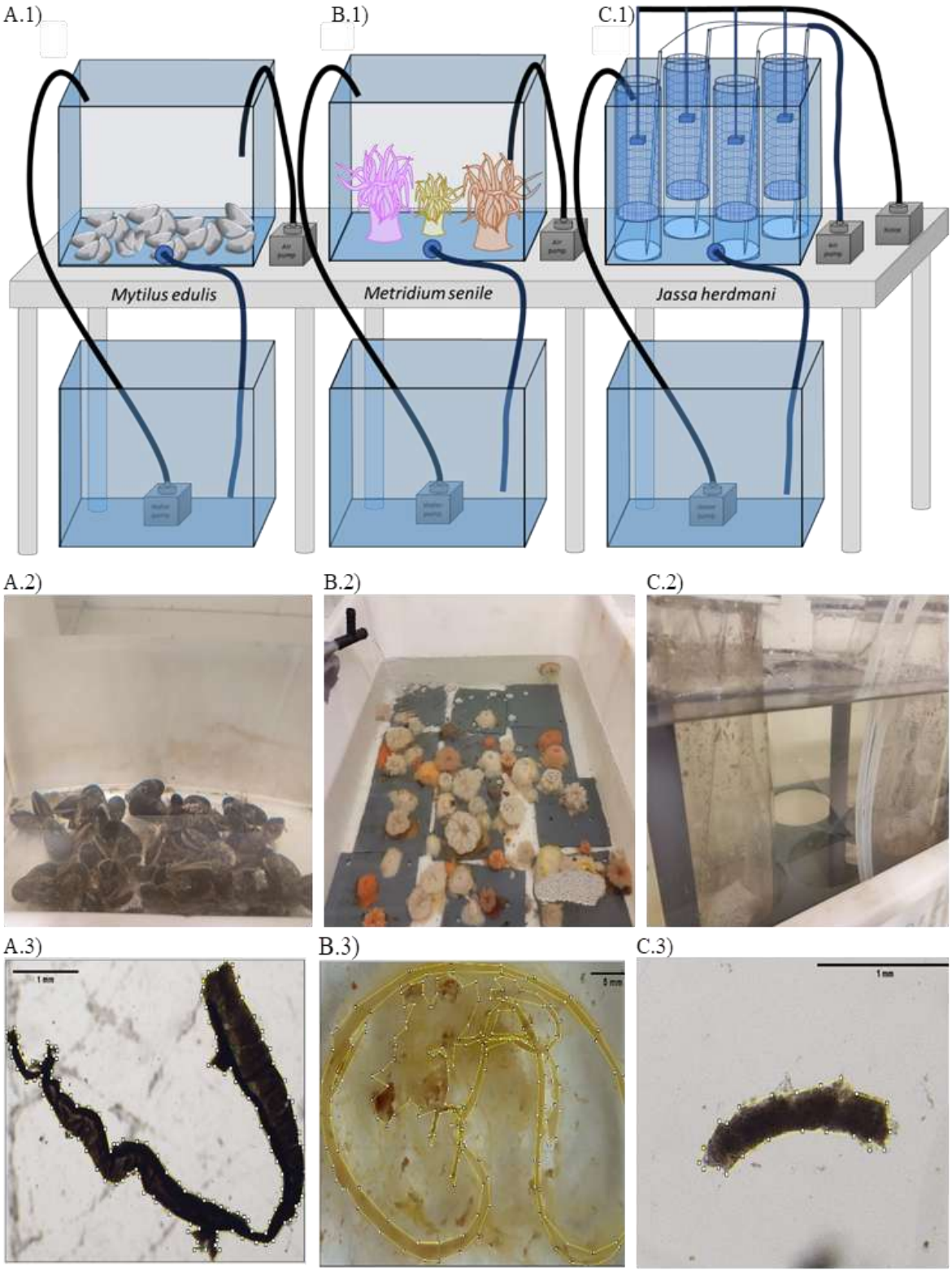

*Figure 5. Panel A) Incubation setup to collect the FP from the key species. Water was circulated from the lower to upper tank via a pump and returned by gravity through a plastic tube. All upper tanks were oxygenated. Panel B) Incubated organisms and, Pa nel C) Example of the faecal pellet physical analysis for the 3 different species: 1) Blue Mussel (*Mytilus edulis*), 2) plumose anemone (*Metridium senile*) and 3) tube-building amphipods (*Jassa herdmani*).*

b. Marker selection and strategy for analysis

Freeze-dried samples from individual endmembers and SPM traps were processed following a three-step AA extraction protocol adapted from Popp et al. (2007) and Hannides et al. (2009, 2013, 2020), and identical to the protocol described for the artificial mixtures. Compound-specific $\delta^{15}N$ values were determined by gas chromatography–combustion–isotope ratio mass spectrometry (GC–C–IRMS).

To select the most suitable AA tracers for unmixing natural samples from the sediment traps, we applied the previously proposed CI/CR/CTS methodology, which had been tested using artificial mixtures prior to model application. However, one important distinction must be considered when applying this methodology to natural samples. Due to their natural origin, the $\delta^{15}N$-AA ratios of the endmembers differ from those of the mixture samples. To account for these differences, we applied the Phe-correction used by Doherty et al. (2021) during their Ala and Thr identification. Phe was chosen because it preserves the $\delta^{15}N$ value of the nitrogen source at the base of the food web (McClelland and Montoya 2002; Chikaraishi et al. 2007). Therefore, the Phe value was subtracted from the other AA ratio values.

Seasonal total organic carbon (TOC) concentrations from environmental samples collected during SPM trap deployment are expressed in mg L^{-1}. For the SPM traps, total carbon (TC) is expressed as a percentage. Carbon measurements were obtained using an Elemental Analyzer–Isotope Ratio Mass Spectrometer (EA–IRMS). Based on the organic carbon (OC) results, a downward OC flux was calculated for each sediment trap. This calculation considered the TOC value (mg), the deployment duration (days), and the surface area of the SPM trap (m^2).

Following the ^{15}N-AA tracer evaluation using the model-independent CI/CR/CTS framework, unmixing analyses were performed. A validated fingerprinting model (FingerPro v2; Lizaga et al. 2018, 2020b) was used to estimate endmember contributions to the SPM trap samples. The model outputs contribution percentages ranging from 0 to 1 for each endmember per sediment trap. These percentages can be directly multiplied by the calculated downward OC flux values to determine endmember-specific OC fluxes for each SPM trap, as the unmixing results are already expressed in carbon units.

3.4 Spatial footprint

a. FP characteristics

As already indicated, the focus is on the faecal pellets of three important species in OWFs: the blue mussel *Mytilus edulis*, the tube-building amphipod *Jassa herdmani* and the plumose anemone *Metridium senile*. *Mytilus* occurs in high densities at the upper subtidal parts of the turbines, up to almost 30000 ind. m^{-2} on a Belgian jacket-based turbine (Mavraki et al. 2023) and occupies the belt between 0.5 m and 8 m below the water surface (Voet 2023). On average 1368 individuals are found per m^2 in the size class 1 to 3 cm (Mavraki et al. 2020b). *Jassa* is generally found below the mussel belt, at 5 to 15 m below the water surface (Voet, 2023). Mavraki et al. (2022) estimate that 31731 active individuals are found per m^2, that are producing faecal pellets. *Metridium* lives at the lower parts of the turbines, and can be found from 15 m below the water surface up to 25 m below the water surface (Voet 2023), where it has become an important contributor to the fouling communities (Kerckhof et al. 2019). Density data (80 ind. m^{-2}) are derived from the BISAR data base (Dannheim et al. 2025).

All these species are important suspension feeders affecting the local primary producer stock (Mavraki et al. 2020a, Mavraki et al. 2023), and returning organic matter to the water column as FP. In the model, a wind turbine is modelled with *Mytilus* living at 14 to 21 meter above the sea bottom (mab), *Jassa* between 7 and 13.5 mab and *Metridium* between 0.5 and 6.5 mab.

The fall velocity of the FP is an important parameter in the Langrangian dispersal model. The fall velocity has been measured in the laboratory using standard techniques (i.e. Belcher et al. 2017). In short, FPs was released in a graduated glass cylinder, filled with ambient sea water. The average sinking velocity has been calculated from the time taken by the FP to sink past 2 marked distances, 10 cm apart. The starting point for the measurements was more than 10 cm away from the water surface to measure the actual terminal sinking velocity. The sinking velocity was measured as a function of the volume of the FP (Fig. 6). For the *Metridium*, *Jassa* and *Mytilus* the sinking velocities were measured for 24, 50 and 60 samples of FP respectively.

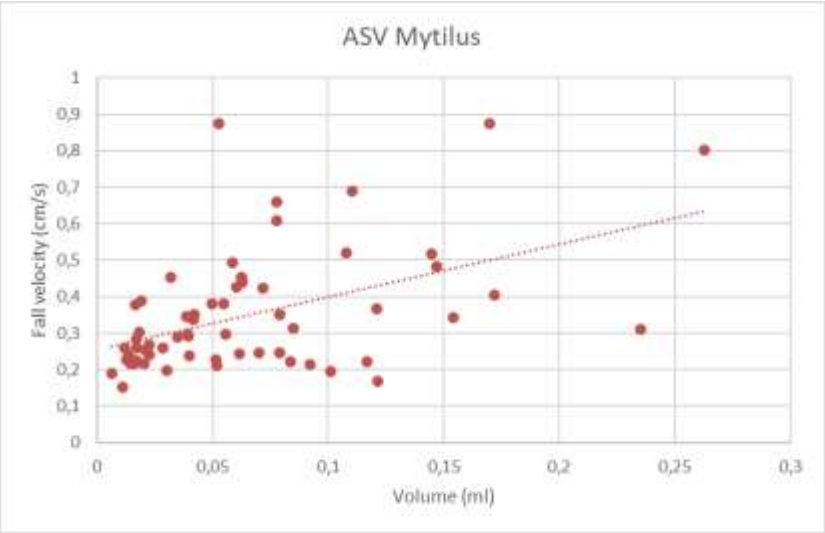

Figure 6. Fall velocity of Mytilus FP (n=60) as a function of FP volume.

Faecal pellets of *Metridium* are much larger than the ones of *Jassa* and *Mytilus*. Furthermore it is striking that the sinking velocity of *Metridium* is decreasing with increasing volume of the FP while the opposite is observed f *Jassa* and *Mytilus* FP. Mean fall velocity varies between 0.11 cm s^{-1} for *Jassa*, 0.25 cm s^{-1} for *Mytilus* and 0.46 cm s^{-1} for *Metridium*. Denis et al. (2025) used a higher fall velocity of 0.77 cm s^{-1} in winter for *Mytilus* in their simulations, based on similar experiments.

The production of the faecal pellets and the carbon that is related released by *Metridium* is estimated by Frontier et al. (2024) and Møller et al. (2003), based on *Isotealia antarctica* and *Utricinipsis antarctica* in summer and winter. A mean value of 3.73*10-4 gC(FP) ind^{-1} day^{-1} was derived. For a the entire monopile, with an estimated diameter of 10 m and taking into account the depth, a total production equalled 226.2 mgC h^{-1}. The production of carbon FP by *Jassa* is estimated at 1.02*10-4 mgC(FP) ind^{-1} h^{-1} (Mavraki et al. 2022). The total FP carbon production by *Jassa* is 661.6 mgC(FP) h^{-1}. For *Mytilus*, values are based on Mavraki et al. (2020b) and estimated at 6.25*10-3 mgC(FP) ind^{-1} h^{-1} , leading to a total of 1877.8 mgC h^{-1}. *Mytilus* therefore produces 6 times as high carbon in the faecal pellets than *Metridium* and 3 times as much as *Jassa*.

b. Modelling strategy

Hydrodynamical model

The model that is set up is based on the COHERENS V2 model (Luyten, 2021), a modelling system for shallow waters. COHERENS follows a modular structure based on a numerical hydrodynamic model. The version of the model included domain decomposition and parallel computing, making it possible to run high-resolution applications. More information on the COHERENS software can be found on the COHERENS V3 website https://ecomod.be/tools/COHERENS/ (Luyten, 2025).

In the framework of the operational forecasting of tides and currents on the Belgian Continental Shelf, a series of models has been set up (Dulière, 2018), starting from a model for the entire North West European Continental Shelf (CoS) to a model of the Belgian Continental Shelf (BeC). While the largest model is a two-dimensional hydrodynamic model, the North Sea (NoS), Southern Bight (SoB) and Belgian Continental Shelf (BeC) models are three-dimensional models. The resolution varies from about 4 km for the CoS model, to 1,5 km for NoS, and 750 m for the SoB model. The resolution of the BeC model is around 270 m x 270 m. A validation of these models is ongoing, but the first results are satisfactory.

To model the dispersal around the wind turbines, a higher resolution model is needed. New higher resolution models and grids were prepared up to a resolution of 10 m x 10 m. Since it is advised to get a refinement of a factor 3 between the nested grids, three additional model grids were set up: a model with a resolution of about 90 m x 90 m, a second one with a resolution of about 30 m x 30 m and the final model grid with the final resolution of 10 m x 10 m. Different high resolution bathymetries were developed based on the data portal of the Afdeling Waterwegen Kust, Flemish Hydrography (AWK) at https://afdelingkust.be/nl/bathymetrische-databank. The final high resolution model has 217 x 271 grids points. In the finest model, the wind turbines are represented by one dry well of 10 m x 10 m, which is in the order of magnitude of the actual monopiles (Fig. 7).

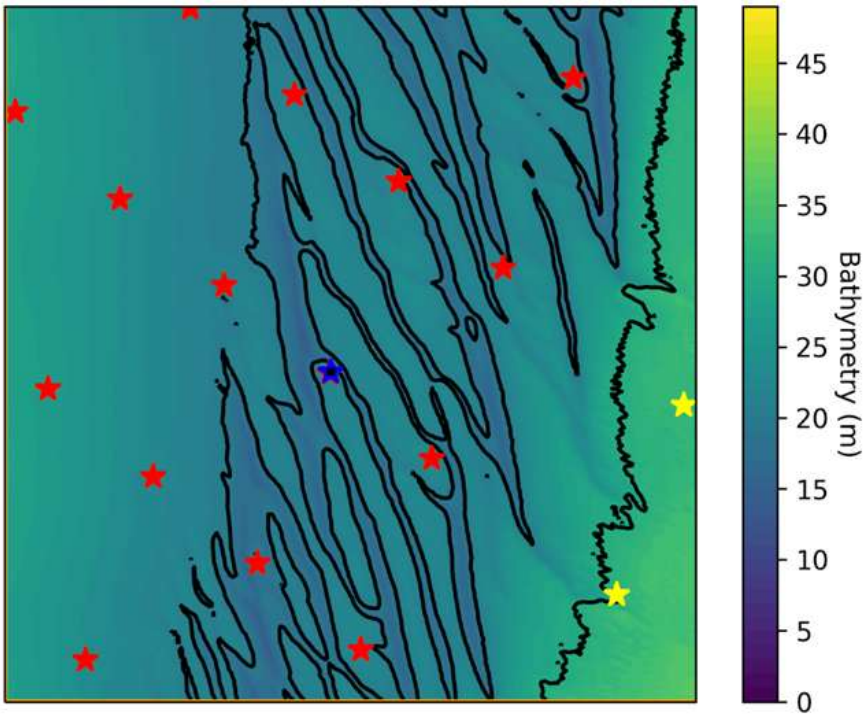

Figure 7. Bathymetry of the 10 m x 10 m. Blue star is the D8 wind turbine of the Belwind wind farm.

Some tests were done on the SpacePole cluster of the Royal Meteorological Institute to find the optimal number of processors to execute the simulations. For the 90 m x 90 m and 30 m x 30 m, 24 processors are used, while for the 10 m x 10 m 48 processors are used. A total calculation time of 1.5 hour for 1 day of simulation is needed for the full chain of models.

Since no hydrodynamic measurements are available in the area, no specific validation has been executed for these model runs. However in the framework of the EDEN2000 studies similar high resolution models have been developed for the Princess Elisabeth zone and a validation has been executed (Van den Eynde et al., 2023). The results have been satisfactory and show that the coupling of the models to this high resolution is working well and that the results in the Belgian Continental Shelf are satisfactory.

Dispersal model

In the framework of the project a simple particle dispersal model has been developed. In the model the particles are followed through the model grid. A fourth-order Runge-Kutta method is used to follow the particle through the model grid with high accuracy . No diffusion is modelled, as the FP are considered to be the centre of a certain mass of particles. At the moment no resuspension is modelled. Resuspension is possible to include in a Lagrangian tracking model (e.g. Lepers et al. 2024), but the height above the bottom where the particle is re-released is subject to a large uncertainty, which adds to the uncertainty of the critical bottom shear stress for erosion.

The simulations have been executed for the results with 2D depth averaged currents, and taking into account the three-dimensional results, with higher velocities near the surface, and lower velocities near the bottom (Van den Eynde, 2025).

During the simulations, it has been found that with low fall velocity, the particles quite rapidly reach the boundaries of the high resolution model. Therefore, in these cases, no information is recovered on the position of the particles. Furthermore, due to the ebb-and-flood movement, it is possible that the particles, after being transported away from the turbine, are being transported back and are deposited in the neighbourhood of the turbine anyhow. Therefore the dispersal models were coupled to follow the particle the different grids and with the highest resolution possible. If a particle enters a high resolution grid, the particles path is again calculated in the high resolution grid (Fig. 8).

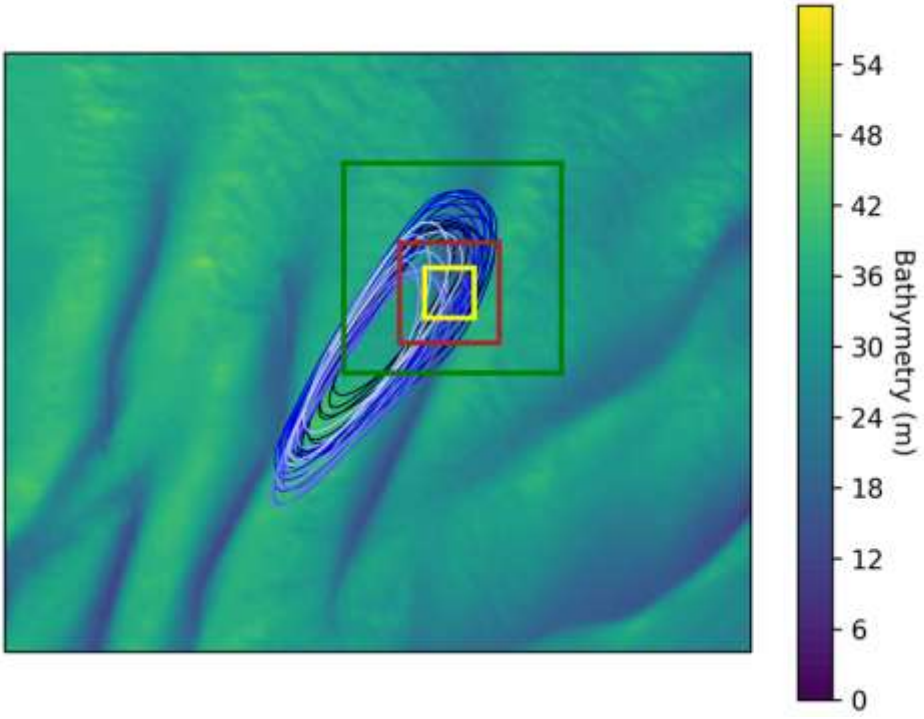

Figure 8. Particle position through different model grids, from dark blue (beginning position) to light blue (final position).

c. Carbon accumulation potential in OWF sediments

The TOC content of the upper 10 cm of the sediment (in weight %, meaning g TOC per 100 g dry sediment), was integrated for this 10 cm sediment column as follows:

TOC content of the upper 10 cm (g m-2)= $\sum i \frac{TOC\%}{100} * grain\ density * (1 - porosity) * 10000$

With *i* representing each one centimetre sediment layer, grain density assumed 2.6 g cm^{-3} and a measured average porosity of 0.3.

The total macrobenthic biomass observed in these sediments in October 2022 was added to the total TOC content of the upper 10 cm. Macrobenthic wet weights have been converted to ash free dry weights using established conversion factors from literature (Ricchiardi et al. 1998, Sistermans et al. 2004 and Gogina et al. 2022), and further converted to C biomass assuming carbon content as 50% of

the ash free dry weight (Wijsman et al. 1999). Since there were no seasonal measurements of macrofauna C biomass, we assumed that the macrobenthic C biomass was constant throughout the year.

The integrated TOC content in the upper 10 cm sediment (see Results 6.1 Table X), measured along the SW gradient of the foundation of turbine D5, was scaled up to the area around this foundation. Due to the tide action, the area has an ellipse shape along the SW-NE axis. The area of the tidal ellipse corresponds to the dimensions of the footprint of the faecal pellets, as derived from hydrodynamic modelling (see Results 4.1). The area of four ellipses was calculated (Table 2). The long radius of the ellipse had a length of 32.5, 40.5, 50.5 or 100.5m, corresponding to the length of the sampled gradient in the field (Methodology 6.1). The short radius of the ellipse was calculated based on the ratio of the short:long radius length as derived from hydrodynamic modelling (Results 4.1), for the widest reach (mussel faecal pellets with a sinking speed of 7.7 m s^{-1}). The average long and short radius of the 95% ellipse for mask 0 and 1 was taken for this calculation. From this area, the surface of the SPL was subtracted (radius 25.5m) and the area of the corresponding inner ellipse (e.g. the area of the ellipse with long radius 100.5m (yellow area in Figure 9) needs to be corrected for the area of the SPL and the area of the ellipse with long radius 50.5m).

Table 2. Dimensions of the ellipse-shaped footprint of the faecal pellets.

Distance to SPL (m)	**Distance to turbine (long radius) (m)**	**Short radius b (m)**	**Area (m^2)**	**Area without SPL (m^2)**	**Area inner ellipse (m^2)**	**Area ellipse ring (m^2)**
7	32.5	11.38	1162	145	0	145
15	40.5	14.19	1805	500	145	355
25	50.5	17.69	2806	1192	500	692
75	100.5	35.20	11115	9072	1192	7880

The final faecal pellet footprint is shown in Figure 9.

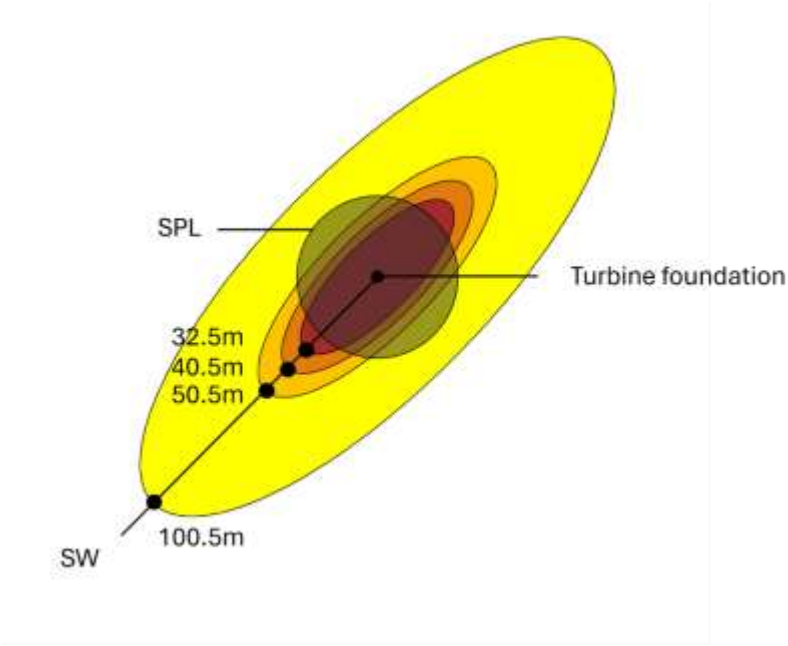

Figure 9 Schematic diagram of the footprint of the faecal pellets, with indication of the turbine foundation in the centre, the SPL with radius 25.5m and the four ellipses with long radius corresponding to the distance from the turbine at which the sediment was sampled.

The total TOC content (g m^{-2}) observed at each of the four distances from the SPL was then extrapolated to the ellipse shape with the corresponding long axis length.

The carbon content upscaled to the four ellipses was then summed and expressed per season.

The total carbon content observed in the sampled sediments within the footprint of the faecal pellets was then compared to the modelled carbon deposited by the fouling fauna within the same area.

3.5 Fate of faecal pellets in the benthic food web

a. Labelling of faecal pellets

Before starting the experiment, natural FP fluxes were estimated for the OWF site to guide the amount of material to be added into the experiment. Individuals of blue mussel, *Mytilus edulis*, were collected from or near turbine D5 (51°32.87952' N, 2°55.77318' E) within the C-Power OWF by divers. The organisms were transported in oxygenated seawater at ambient temperature to minimize stress. Natural seawater collected during sampling was used in laboratory incubations to replicate in situ food availability conditions. After a 24-hour acclimation period in the laboratory, 151.5 mg of 99% of ^{13}C-labelled algal lyophilized cells (*Synechococcus* sp.) was resuspended in 1 L of filtered sea water and added to the experimental container. The amount added was based on previous experimental data, where approximately 0.1 g of ^{13}C-labelled *Synechococcus* cells (equivalent to 43 mg C, 99 % ^{13}C; Sigma-Aldrich, VR 487945) (Mavraki et al. 2020) was used, and extrapolated for a container capacity of 30 L. Labelled FP were collected over 5 days, taking into account that mussel filtration rates decreased with declining cell availability. (Riisgård, 1991). The collected pellets were centrifuged and rinsed three times with 0.01 M synthetic seawater, then stored at –80 °C. The water tank was clean daily to ensure collection of fresh FP each day. At the end of the experiment, all FP were lyophilized and homogenized using a mortar and pestle. A subsample was analysed for carbon content using an Elemental Analyzer–

Isotope Ratio Mass Spectrometer (EA–IRMS; Sercon, UK) to verify that the desired ^{13}C enrichment was achieved.

A sufficient quantity of mussel faecal pellets enriched to 5 % ^{13}C was produced for all sediment incubation experiments. For each experimental core, approximately 190 mg of labelled FP was carefully distributed across the sediment surface. The pellets had a total organic carbon (TOC) content of 26.3%, corresponding to 49.34 mg of organic carbon per core (Table 3).

Table 3. Amount of FP (mg) with 13C-labelled carbon added to each experimental core, and corresponding TOC content of the added material at the beginning of the experiment

Location	Core	FP added to core (mg)	OC content FP (mg)
REF	1	189.9	49.374
REF	2	189.4	49.244
REF	3	189.7	49.322
REF	4	189.3	49.218
OWF	1	190.4	49.504
OWF	2	190.5	49.53
OWF	3	189.3	49.218
OWF	4	189.7	49.322

b. Study area and sampling

Sampling was conducted during the RV Belgica campaign (21–31 October 2023) in the Belgian part of the North Sea (BPNS). Two sites were targeted: the C-Power OWF. approximately 100 m southwest of turbine D5 (51°32.87952’ N, 2°55.77318’ E), and a reference site (REF) on the Groote Bank (51°27.63753’ N, 2°52.02166’ E).

At each site, four box-cores were collected. From each, the upper 10 cm of sediment was subsampled into one large Plexiglas incubation core (19 cm diameter) and five smaller cores (3.6 cm inner diameter; ≈10 cm^2) used to determine porewater dissolved inorganic carbon (DIC), background ^{13}C signatures of total organic carbon (TOC), bacteria, meiofauna, and to measure sediment permeability. The remaining water outside of the subsampling cores was carefully siphoned into a vial and then filter through Ø25 mm GF/F glass fibre filters (0.7 µm pore size) that had been pre-combusted and weighed for particulate organic carbon analysis. For the collected sediment cores, porewater was extracted at 1 cm intervals using 3 cm rhizons (0.15 µm pore size) inserted into pre-drilled holes sealed prior to sampling and transferred to pre-weighed 12 mL Exetainers (Labco, UK) containing 85 µL of 37% HCl and flushed with N_2. Sediment samples for TOC analysis were sectioned into 1 cm layers down to 10 cm. Cores designated for bacterial analysis were sliced into 0–2, 2–5, and >5 cm layers (total depth 9–14 cm). Meiofauna cores were sectioned into 0–1, 1–5, and >5 cm layers (total depth 9–15

cm). All sediment layers were stored at –20 °C. Remaining sediment was sieved through a 1 mm mesh to isolate macrofauna, identified to higher taxonomic levels, and frozen at –20 °C.

c. Experimental setup and flux measurements

The large incubation sediment cores were bottom sealed and transported to the laboratory, where they were randomly allocated in a temperature-controlled seawater bath (14 °C, TECO temperature control unit). The cores were aerated and allowed to acclimate for 24 hours before the addition of the labelled FP. For each experimental core, approximately 190 mg of labelled FP was carefully distributed across the sediment surface. The pellets had a TOC content of 26.3%, corresponding to 49.34 mg of organic carbon per core (Table 4). After adding the ^{13}C-labelled material, a stirred chamber with rotating Plexiglas disc (Plexiglass Ø: 19 cm; *H*: 30 cm) positioned 5.4 cm above the sediment surface was used to simulate near-natural advective porewater flow at 12 rpm (Huettel and Rush 2000). The cores were then left to equilibrate for another 24 hours prior to the start of the first incubation with oxygenation. Oxygen concentration and temperature were continuously monitored using a pre-calibrated Firesting oxygen miniprobe (PyroScience; 3 mm diameter, 10 cm length) (Figure 10).

Table 4 Amount of fecal pellet (mg) with labelled carbon added to each core, and organic carbon content of the added faecal pellet at the beginning of the experiment.

Location	Core	FP added to core (mg)	OC content FP (mg)
REF	1	189.9	49.374
REF	2	189.4	49.244
REF	3	189.7	49.322
REF	4	189.3	49.218
OWF	1	190.4	49.504
OWF	2	190.5	49.53
OWF	3	189.3	49.218
OWF	4	189.7	49.322

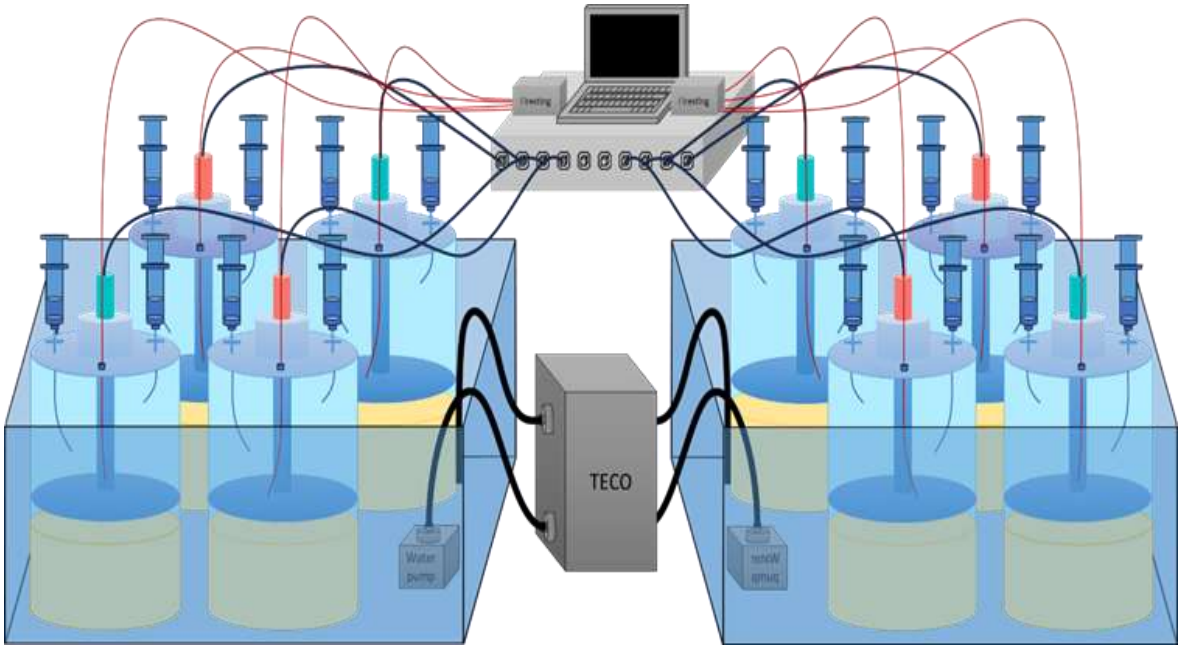

Figure 10 Experimental setup for sediment core incubations. Each water bath contained sediment cores (19 cm diameter) maintained at 14 °C. Oxygen concentrations were recorded in each core using FireSting O_2 sensors connected to a multichannel interface and computer for data logging. Temperature stability was maintained by a TECO temperature control unit and circulating water pumps. Cores collected from within the offshore wind farm (OWF) are shown in turquoise, while cores from the reference site (REF) are shown in coral red; both types were evenly distributed and randomly allocated between the two water baths

Closed-core incubations were conducted three times over the 7-day experimental period. During each incubation, both the top and bottom of the cores were sealed to minimize gas exchange, and the oxygen supply line was removed. Incubations proceeded until oxygen saturation declined to approximately 70% of the initial level, ensuring that values remained above 60% to prevent the onset of anaerobic mineralization within the sediment. Discrete samples for DIC and TOC analysis were collected at regular intervals using 20 mL plastic syringes through gas-tight sampling ports in the upper lids of the cores. At each sampling, 5 mL of overlying water was withdrawn and immediately replaced with 5 mL of filtered seawater to maintain constant volume. The samples were filtered directly through 0.45 µm PTFE syringe filters fitted with 26-gauge needles into 12 mL Exetainers (Labco, UK) that had been pre-flushed with N_2, contained 85 µL of 37% HCl, and were pre-weighed. In a subset of reference cores, an automated DIC-trap system driven by an air pump was tested. However, minor air leakage caused small fluctuations in water level, rendering the system ineffective; this issue was documented and considered during data interpretation.

At the end of the experiment, before sediment subsampling, the overlying water was carefully siphoned off for POC analysis, leaving 1 cm on top of sediment. Then, subsamples were collected using small Plexiglas cores (3.6 cm diameter) for the analysis of porewater DIC, ^{13}C in TOC, bacterial biomass and meiofauna. The core designated for TOC analysis was also used for granulometry and pigment quantification. The remaining sediment was sieved through a 1 mm mesh to collect macrofauna, which were processed and stored as described for the pre-experimental sampling.

d. Laboratory analysis

Water samples collected during the experiment were analyzed for ^{13}C-DIC, TOC, total alkalinity, and nutrients. The concentration and isotopic composition of ^{13}C-DIC in overlying water and porewater

were determined by measuring CO_2 in the headspace of sealed Exetainer vials using a gas chromatograph equipped with a thermal conductivity detector (Trace GC, Interscience), correcting for injected sample volume and pressure changes. TOC samples from the sediment were pooled into depth layers (0–1, 1–2, 2–4, 4–6, and 6–10 cm), homogenized, dried, and ground. Approximately 80 mg of material was weighed into pre-combusted silver cups and acidified following the procedure used for faunal samples, then sealed in tin capsules and stored in a desiccator until EA-IRMS analysis. During the first and third incubation cycles at both REF and IMP sites, additional water samples were collected for total alkalinity and nutrient analyses (phosphate, nitrate, nitrite, and ammonium). At the end of the experiment, the remaining overlying water was filtered through Ø25 mm pre-combusted GF/F filters (0.7 µm pore size) for POC determination.

Sediment samples collected after the incubations were used for several analyses. Subsamples for TOC were also used for granulometry, which was measured by laser diffraction using a Malvern Mastersizer Hydro 2000G. Pigments were extracted from freeze-dried sediment using 90% acetone and quantified with a Turner fluorimeter. TOC and TN were measured using an elemental analyser after acidification of ~15 mg of sediment to remove inorganic carbon, and additional subsamples were processed for stable carbon and nitrogen isotope composition. Sediment permeability was measured on intact cores using a permeameter following Buchanan (1984).

Bacterial uptake of the added phytodetritus was assessed via isotope enrichment of bacterial-specific phospholipid fatty acids (PLFAs), following Boschker and Middelburg (2002). Two diagnostic PLFA biomarkers (i15:0 and ai15:0) were selected because of their specificity for bacteria and consistent presence across samples. After lipid extraction, fatty acids were converted to fatty acid methyl esters (FAMEs), and their $\delta^{13}C$ values were analysed by GC-IRMS (Thermo Scientific Delta Plus with Trace GC Ultra, via GC Isolink and ConFlo IV).

Meiofauna were extracted by sieving samples through a 38 µm mesh and repeatedly decanting the suspended fraction into a sieve to recover organisms. The retained material was examined under a stereomicroscope, and meiofauna were sorted into higher taxonomic groups. Because nematodes and copepods were the most abundant taxa, only these were collected for stable isotope analysis, with at least 150 nematodes and 60 copepods required per sample. Depth layers contained insufficient individuals to be processed separately, so samples were pooled per core. Organisms were transferred to aluminium cups, dried at 80°C overnight, and stored in a desiccator until EA-IRMS analysis. Stable isotope measurements were performed at KU Leuven using an elemental analyser (Thermo Flash HT/EA or EA 1110) coupled to a Thermo Delta V Advantage IRMS via a Conflo IV interface. Calibration was performed with IAEA-600, an in-house leucine standard, and an in-house tuna standard, with results expressed relative to VPDB.

Macrofauna isolated from the remaining sediment were thawed, cleaned, and dried overnight at 80°C in pre-combusted porcelain cups. Larger organisms were homogenized using a mortar and pestle, while small organisms were analysed whole. Samples containing $CaCO_3$ were placed in silver cups and acidified by gradually increasing HCl concentration (1%, 5%, and 10%) until the reaction was complete, using a hot plate to assist evaporation. Non-calcareous samples were placed directly into aluminium cups without acidification. All macrofauna samples were analysed at the UGent Isotope Bioscience Laboratory (ISOFYS) using EA-IRMS (EA IsoLink interfaced through a ConFlo IV to a Thermo Delta Q).

Calibration standards included USGS 63, USGS 61, enriched in-house maize, and quality assurance standards USGS 62 and Low Organic Content Soil. Final $\delta^{13}C$ values are expressed relative to VPDB.

e. Strategy for analysis

Rates of sediment community oxygen consumption (SCOC) and ^{13}C-DIC accumulation were calculated from the linear decrease or increase in concentration over time during the closed-core incubations. Oxygen fluxes were calculated from the regression slopes of the oxygen concentration over time (Eq.1).

$$SCOC = \frac{dC}{dt}\frac{V}{A} \qquad (1)$$

The total amount of respired ^{13}C was estimated by averaging the slopes obtained from the incubation experiments and multiplying this mean rate by the duration of the experiment. Because the DIC-trap system malfunctioned during the first incubation, the resulting ^{13}C-DIC measurements were considered unreliable and were excluded from further calculations.

The relative contribution of faecal-pellet-derived carbon to the different carbon pools (macrofauna, meiofauna, bacteria, TOC, POC and porewater DIC) was determined as follows (Eq. 2):

$$FP\ derived\ C = \frac{a^{13}C_{Sample} - a^{13}C_{bg}}{a^{13}C_{FP} - a^{13}C_{bg}} \qquad (2)$$

Background ^{13}C abundance ($a^{13}C_{bg}$) were determined from non-enriched samples. For TOC, background values were calculated per site and sediment layer; for meiofauna and macrofauna, background values were determined per taxon. When a given taxon appeared in the enriched samples, but no natural-abundance individuals were available, a higher-level taxonomic group was used to establish background values. For example, no Cumacea were present in the non-enriched samples, so the average ^{13}C signature of Amphipoda and Mysida was used as a proxy.

To assess whether FP derived C accumulation in the different pools differed between samples collected inside the offshore wind farm and those from the reference area (REF), statistical comparisons were conducted. When assumptions were satisfied, a two-sample t-test was applied. Normality was evaluated using the Shapiro–Wilk test, and homogeneity of variances with Levene's test. When these assumptions were not met, a Wilcoxon signed-rank test was used instead. Statistical significance was set at $\alpha = 0.05$ for all tests.

3.6 Mineralisation of organic matter in OWF sediments

Additional deposition of organic matter (OM) on the seafloor surrounding wind turbines, as hypothesized in the project, is expected to change mineralization (recycling) processes in the seafloor (biogeochemical processes), which in turn has repercussions on the return flux of nutrients to the water column (benthic-pelagic coupling). In OUTFLOW, we studied this process in data-driven model representations of biogeochemical processes in the seafloor. The sediment in the study area is generally permeable (coarse-grained), as opposed to cohesive(fine-grained). This means that transport of solutes in the interstitial water in the seafloor is dominated by advective transport, as

opposed to diffusive transport in cohesive sediment. So, the modelling required the application of a novel model description which includes advective porewater transport, as model descriptions of early diagenetic processes tend to focus on cohesive sediments.

a. Sampling

We studied the sediments in the immediate vicinity of an offshore wind turbine within the C-Power wind farm concession in the BPNS (turbine "D5"). This 5MW turbine with gravity based foundation was constructed in 2008, and has been the focus of several environmental studies (e.g. De Mesel et al. 2015; Kerckhof et al. 2010; Mavraki et al. 2020). We sampled the sediment along a transect extending southwest from the turbine, at distances of 7, 15, 25, and 75 m away from the edge of the scour protection layer (SPL), aligned with the direction of the main tidal current.

At 7, 15, and 25 m, a scientific dive team collected nine perspex cores of 3.6 cm inner diameter: six for the extraction of porewater nutrients, and three to six for the determination of granulometry, pigments, and TOC. The cores were pressed into the seafloor by hand, aiming for 15 cm of sediment in the cores, and sealed with a rubber stopper. From the research vessel (*RV* Belgica, *RV* Simon Stevin), a NIOZ boxcore was lowered to the seafloor at 75 m away from the edge of the SPL, and retrieved after closing. From the initial 30 cm diameter sample, nine 3.6 cm diameter subcores were collected: 5 for the extraction of porewater nutrients, and 4 for the same environmental parameters as described above. This sampling scheme was replicated seasonally if possible, in summer no vessel was available to take samples at 75 m distance. In winter, no samples were collected due to unfavourable weather conditions, see Table 5 for an overview of sampling dates and conditions.

Table 5. Details of sample collection

Season	Distance SPL (m)	Sampling date	Sample type	Bottom water temperature	Salinity	Campaign code
Spring	7	27/04/2022	diver	9.9	32.6	SiSt_22-220
	15	29/03/2022	diver	8.25	33.4	BE2022_08
	25	28/03/2022	diver	8.25	33.4	BE2022_08
	100	28/03/2022	boxcore	8.25	33.4	BE2022_08
Summer	7	05/07/2022	diver	18.5	33.5	SiSt22-370
	15	05/07/2022	diver	18.5	33.5	SiSt22-370
	25	05/07/2022	diver	18.5	33.5	SiSt22-370
Fall	7	06/09/2022	diver	20	33.3	SiSt22-520
	15	07/09/2022	diver	20	33.3	SiSt22-520
	25	08/09/2022	diver	20	33.3	SiSt22-520

	100	10/17/2022	boxcore	20	33.3	BE2022_25

b. Sample processing

Sedimentary characteristics

Sediment cores were sliced at 1 cm intervals using an extruder, with overlying water carefully removed to avoid surface disturbance. Each section was stored in aluminium vials at –80 °C. Samples were freeze-dried to determine water content (weight %) and calculate porosity from water content and solid-phase density, correcting for porewater salinity. On each slice, grain size distribution (median grain size, D_{50} µm), total organic carbon (TOC) content (% dry weight) and photosynthetic pigments (chlorophyll a, pheophorbide) were analysed.). Sediment permeability was estimated from D_{50} following Wilson et al. (2018).

Porewater nutrients

Porewater was sampled through pre-drilled core holes at 1 cm intervals using rhizon samplers (0.15 µm; Rhizosphere Research Products). Approximately 3 mL of porewater was collected per interval under vacuum with N_2-flushed syringes to minimize oxygen exposure, following Dickens et al. (2007) and Seeberg-Elverfeldt et al. (2005). Overlying water samples (~5 mL) were retrieved similarly.

All porewater samples were frozen (–20 °C) until analysis. After thawing, nutrient concentrations were measured using a SEAL QuAAtro segmented flow analyser (Jodo et al., 1992).

c. Permeable diagenesis

To investigate sediment biogeochemistry near offshore wind turbine foundations, we applied the PermeableDia model (Soetaert & De Borger, unpubl.), a two-dimensional reactive transport model developed to simulate early diagenetic processes in permeable sediments. Unlike conventional 1D diagenetic models, PermeableDia explicitly incorporates advective porewater flows that arise from pressure gradients induced by seabed topography (e.g. ripples, small dunes) and local hydrodynamic forcing. This makes it particularly suited for representing the physical–biogeochemical coupling in sandy shelf environments.

Model structure and flow generation

The model describes a two-dimensional sediment domain of 1 m depth and one ripple wavelength in length. The advective flow field is generated in two steps. First, a spatially variable pressure head is imposed along the sediment–water interface, represented as a sinusoidal boundary condition reflecting the ripple geometry. This pressure distribution generates porewater flow through the sediment matrix, which is computed by solving a steady-state boundary value problem for the hydraulic head. Flow magnitude depends on sediment porosity, permeability, storativity, and water viscosity. From the pressure field, the model derives porewater velocities, which are subsequently used as an additional advective transport term in the reactive transport equations for solutes.

The flow model was parameterized for each season–distance combination using site-specific measurements of median grain size, temperature, salinity, and permeability, which were used to estimate ripple height and wavelength following empirical relations for current-generated bedforms. For the modelled conditions, ripple heights ranged between approximately 2 and 3 cm, and

wavelengths between 17 and 25 cm. Permeability values were derived from grain size data, ranging from 2×10^{-12} to 1×10^{-11} m². A representative porosity of 0.3 was used for all simulations.

Biogeochemical processes

Advective flows were coupled to a model of early diagenesis (OMEXDIA, Soetaert et al. (1996), extended to include phosphorus cycling (Ait Ballagh et al. 2020). The model simulates the degradation of organic matter through a "3G" scheme consisting of three fractions of differing degradability: fast, slow, and refractory organic matter. The two reactive fractions are remineralized through successive redox pathways depending on the local availability of oxidants: oxic mineralization, denitrification, and anoxic mineralization (including sulphate and metal reduction, represented as oxygen demand units – ODUs). The model includes ten state variables: four solids (fast and slow organic carbon, Fe-bound phosphorus, Ca-bound phosphorus) and six solutes (O_2, NO_3^-, NH_3, ODUs, PO_4^{3-}, and DIC). The equations are solved to steady state using the rootSolve package in R.

Model setup and parameterization

Model dimensions and flow parameters were defined using the permeable.flow function within the PermeableDia package, allowing specification of ripple geometry and grid resolution. The horizontal axis was discretized into 10 cells, and the vertical axis into 50 cells with a non-uniform grid (finer near the sediment surface). The upper boundary was defined as a fixed pressure head varying sinusoidally along the sediment surface. Zero-gradient conditions were applied at the lower and lateral boundaries to allow open exchange.

Biogeochemical parameters were initialized based on literature values for permeable coastal sediments, with adjustments to reflect higher reactivity and oxygen availability relative to cohesive environments. Initial carbon fluxes (*Cflux*) to the sediment were estimated from literature values for the Belgian Part of the North Sea and in situ sediment trap data, covering a range of 10–250 mmol C m^{-2} d^{-1} of potential values for deposition during the sampling period.

Model fitting and optimization

Model fitting combined manual calibration, numerical optimization, and Monte Carlo uncertainty analysis. First, manual calibration was used to identify plausible values for fast and slow organic matter degradation rates (*rFast*, *rSlow*), bioturbation intensity (*Db*), and depth (*L*), by visually matching modelled and observed TOC and ammonium profiles.

Next, parameters were optimized using the BOBYQA algorithm (R package nloptr), minimizing the sum of squared residuals between measured and modelled 1D profiles of TOC, NH_3, and NO_3^-. Because PermeableDia outputs 2D results, these were horizontally averaged before fitting. Optimized parameters included carbon flux (*Cflux*), nitrification rate (*rNit*), and half-saturation constants for nitrate and oxygen limitation. Parameter bounds were constrained to ±10–50% of initial estimates based on sensitivity and identifiability. Temperature modifications (Q_{10} = 2, reference 15 °C) were applied to *rFast* and *Db*, and parameter uncertainty was quantified via MCMC analysis (2000 iterations, FME package). Sensitivity tests using sensRange assessed the influence of permeability, porosity, and ripple geometry on mineralization pathways.

This combined data-driven modelling and fitting approach enabled quantitative comparison of modelled porewater profiles with field observations, and provided constrained estimates of key

process rates such as total mineralization, nitrification–denitrification, and solute exchange fluxes across the sediment–water interface.

3.7 Spatial upscaling: field based measurements

a. 3- Vessel campaign set up

We collected data on suspended particulate matter (SPM) in and around offshore wind farms located along the Belgium–Netherlands marine border in the Southern Bight of the North Sea (SBNS) (Figure 11). The combined concession areas contain 571 turbines over roughly 620 km², mainly on monopile foundations (n = 517), with a few gravity-based (n = 6) and jacket (n = 48) structures. The SBNS is a shallow, dynamic region (depths <40 m) with tidal currents up to 1 m s^{-1}, keeping the water column well-mixed year-round and promoting high primary productivity (317–522 g C m^{-2} y^{-1}). Coarse sandy sediments dominate, while finer materials occur mainly nearshore.

We combined transect-based sampling and fixed mooring deployments to capture both spatial and temporal variability of SPM across the wind farm area (Figure 11). Three research vessels operated along upstream (RV Belgica), within-farm (RV Simon Stevin), and downstream transects (RV Pelagia), completing repeated 13-hour surveys with CTD and Niskin sampling. Vessels stopped each half hour for a CTD cast, and every hour for a CTD cast + Niskin sampling. Transect and mooring positions were optimized using 2D hydrodynamic particle-transport modelling (Van den Eynde, 2022) to ensure that water masses sampled upstream could be tracked downstream as they passed through the wind farm**.**

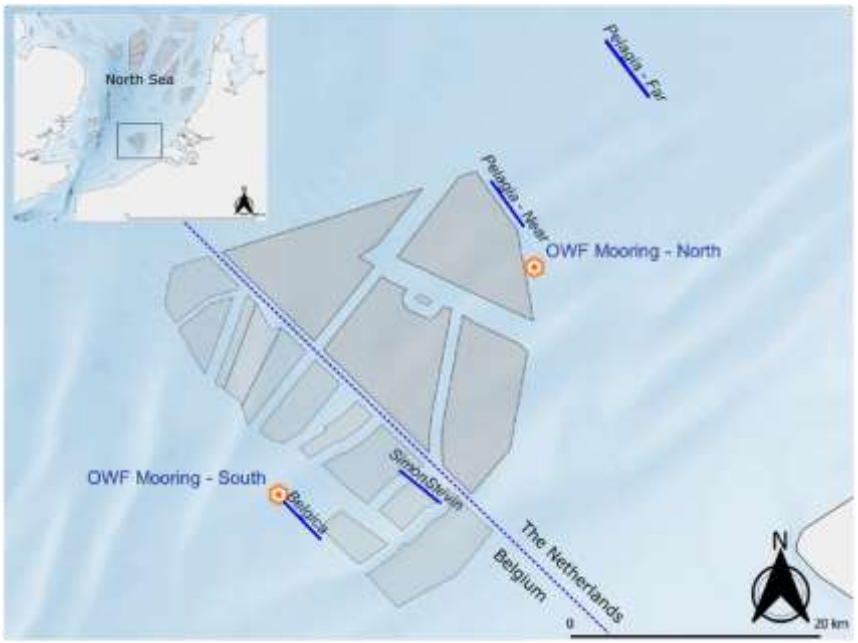

Figure 11 The offshore wind farm aggregation along the marine border between Belgium and the Netherlands (dotted blue line) in the Southern North Sea. Individual wind farm concessions are outlined as grey polygons. Sampling transects of the different ships are shown as full blue lines. Locations of the moorings are indicated as orange-white dots.

During each CTD cast, three bottles on a rosette sampler were closed at surface (1 m below surface), mid-water, and bottom (≈3 m above the seafloor), giving nine samples per cast. Upon retrieval, water was subsampled for SPM, chlorophyll a, and nutrient analyses.

For SPM, 750–2000 mL of seawater was filtered under vacuum through pre-weighed GF/F filters (0.7 µm), rinsed three times with Milli-Q water to remove salts, stored in petri dishes, and frozen. Chlorophyll *a* was determined from 750–2000 mL filtered over GF/F filters, rinsed with synthetic seawater, and stored at −80 °C (either directly or after flash-freezing in liquid nitrogen). Surface samples were also filtered (0.45 µm syringe filter) for dissolved nutrients, which were frozen at −20 °C until analysis.

b. Lab work

All samples were analysed at the Royal Netherlands Institute for Sea Research (NIOZ). SPM concentrations were determined gravimetrically from filter weight differences, and organic carbon and nitrogen contents were measured with an Interscience Flash 2000 elemental analyser after acidification with 0.1 N HCl. Chlorophyll *a* was quantified fluorometrically using 90% acetone extraction, and dissolved nutrients (nitrate, nitrite, ammonium, phosphate, silicate) were analysed with a SEAL QuAAtro segmented flow analyser.

c. Statistical analysis

Linear mixed-effects models were used to compare SPM, chlorophyll *a*, and related ratios (organic C:N, chl a:SPM, chl a:organic C, organic C:total C) among sampling locations, following Zuur et al., (2009) using the lme package in R (Pinheiro et al., 2023). ADCP current headings (°) were decomposed into sine and cosine components to account for tidal current direction (east–west, north–south). Data were explored for outliers, collinearity, and interactions prior to modelling. For comparisons among the three vessels, we fitted:

Response ~ location + depthclass + mean velocity + sin-heading + cos-heading + mean upward velocity + mean upward velocity × (location + sin-heading + cos-heading) + 1|(day/station),

with station nested within day as a random effect. For the Pelagia-only dataset (including a control transect sailed on a separate day, Figure 2), location was replaced by sampling day:

Response ~ day + depthclass + mean velocity + sin-heading + cos-heading + mean upward velocity + mean upward velocity × (day + sin-heading + cos-heading) + 1|(station).

Residuals were visually inspected for normality and homoscedasticity; where needed, variance structures were added to model heterogeneity in residualsnon-constant spread. Model simplification followed a stepwise backward selection based on $p < 0.05$ and log-likelihood ratio tests, comparing models by AIC. Fixed effects were selected under maximum likelihood (ML) and final models refitted with restricted ML (REML).

For environmental parameters (temperature, salinity, nutrients), Wilcoxon rank-sum tests were used to compare locations due to heteroscedasticity in these data.

3.8 Spatial upscaling: modelling

This task addressed the question of spatial upscaling of the local processes explored in other work packages, from a biogeochemical perspective. For complementarity with the achievements made in other WPs, we focused on detailing the influence of the fouling fauna inhabiting the lateral surface of wind farm monopiles on the surrounding ecosystem processes, at spatial scales of a single offshore wind farm (OWF) on the order of 1-50km.

a. Model description

We set up a spatially explicit model framework resolving the tidal circulation and the typical biogeochemical cycle of the southern North Sea, and by developing a module to express the filtration activity of biofouling fauna inhabiting the submerged surfaces of offshore infrastructure, and the transport and deposition of their faecal pellets (FP).

COHERENS (Luyten et al., 2025: https://doi.org/10.5281/zenodo.11261106, last access: 30 June 2025) is a three-dimensional hydrodynamic model designed for a wide range of applications in coastal and continental seas, estuaries, lakes and reservoirs ((https://ecomod.be/tools/COHERENS/, last access: 21 November 2025). Its Biogeochemical (BGC) module has been developed with the the Framework for Aquatic Biogeochemical Models (FABM, https://github.com/fabm-model/fabm) to maintain modularity and facilitate its integration with different hydrodynamical models. The model includes, in the pelagic layer, two phytoplankton groups (silicate-consumers, a.k.a diatoms, and non-silicate-consumers), one zooplankton group, two particulate detrital pools (slow-decaying and fast-decaying particulate organic matter, with remineralisation rates of respectively 0.09 and 3.65 yr^{-1}). In the benthic layer, it includes two pools for particulate detrital organic matter (slow and fast) and one pool for silicious detritus. We do not explicitly resolve the benthic layer and all benthic pools are vertically integrated. The model is expressed in terms of carbon, nitrogen, phosphorus and silicon content and includes a detailed carbonated chemistry module. The ecosystem dynamics involves a dynamic chlorophyll to carbon formulation (Geider, et al. 1997), while a fixed stoichiometric composition is applied for plankton and particulate components.

We developed a modular solution to incorporate sessile suspension feeders within aquatic BGC models formulated in FABM (Bruggeman, et al. 2014). The module is generic and can easily be adapted to different BGC model designs. Here, we assume one single filter-feeder species (blue mussel) with a static biomass and imposed process rates: clearance rate, FP production and FP sinking rates. Those rates include seasonal variation and were acquired through dedicated lab experiments (in the context of SPF-Economy ETF projects EcoMPV and SWIM) and are considered to be representative of the dominant biofouling community. Planktons and particulate matter of the NPZD model are consumed by filtration, which is set by the local density of biofouling biomass and its clearance rate. Part of the ingested material is egested as faecal pellets. The remnant part is processed and returned to the water column in dissolved phase (i.e. dissolved inorganic carbon, ammonium, phosphate and silicate). Faecal pellets are subjected to transport and assigned with sinking velocity. Upon reaching the benthic layer, their stoichiometric content is redistributed amongst the benthic variables of the NPZD model.

b. Process rates

The data on blue mussel characteristics were provided by ongoing projects ECoMPV and SWIM and included information on seasonal process rates of clearance rates, FP production rates, and FP sinking

velocity (Figure 12). To represent the entire fouling community, mean monthly values were calculated for the three mussel size classes. A von Mises functional form was adopted for all three parameters.

Figure 12. Seasonal laboratory experiment results and the associated fitting functions to produce seasonal forcings. (a) Mussel clearance rate. (b) Faecal pellet production rate. (c) Faecal pellet sinking velocity.

c. Model setup and scenario

We consider a synthetic domain extending over 40km, with a flat bathymetry at 20m depth. The domain is forced with typical marine conditions of the BPNS, in terms of atmospheric conditions (C3S, 2018), tidal flows (Marine Forecasting Centre, 2023) and biogeochemical initial conditions (Lancelot et al., 2005). The residual circulation in this setup is oriented northwest. The calibration of the NPZD parameters derives from a 1D simulation (EcoMPV Project deliverable, D1.5) set along the monitoring station "W08" and relied on monitoring data (POC, CHL, NO2, PO4, SiO) obtained in the context of the BELSPO BG-PART project. We assume that there is no significant lateral input of nutrients and that nutrient dynamics are driven by local biogeochemical processes. Initial conditions of nutrients (PO_4, NO_3, NH_4, Si), phytoplankton biomass and Particulate Organic Matter (POM) are adapted to local conditions.

A scenario simulation is compared to the reference run. The scenario includes 54 turbines of 8 m diameter located 1000 m from each other in the centre of the domain, in a regular 9 x 6 grid thus extending on 9 by 6 kms. The 3D spatial distribution of submerged surfaces is derived from this configuration, and used to set the initial condition of the biofouling community. A spatial resolution of 500m is adopted which enables the location of one single turbine each two cells in the centre (Fig. 13). We consider the fouling community to be concentrated on the upper 8m below the average sea surface, each foundation accounting for 200m² of submerged hard substrates. The distribution of the biofouling biomass in each model grid cell then derives from the vertical discretization and the local sea surface elevation.

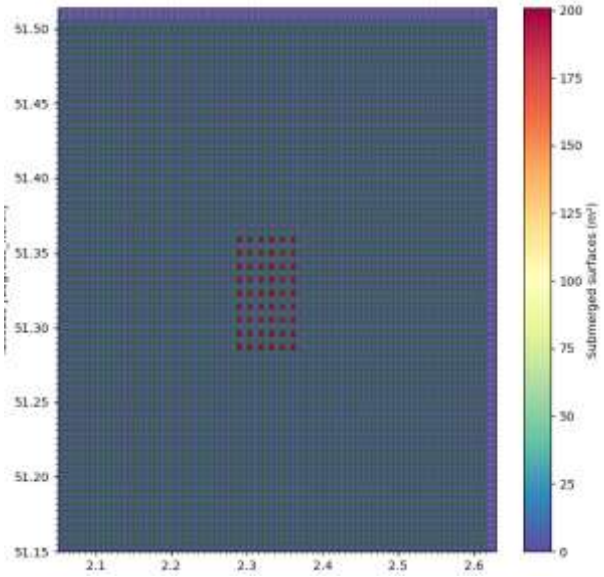

Figure 13 Model grid (zoomed on the central part).

4. SCIENTIFIC RESULTS AND RECOMMENDATIONS

4.1 The offshore wind food web

The food webs and associated work delivered information on (1) food web characteristics, difference in biomass and network topology between different food webs, (2) variations in organic carbon uptake pathways driven by differing functional role of fauna in the food webs, (3) and secondary production of fish within the OWF.

a. Descriptive food web properties

The OWF food web had the highest species richness (120 species) compared with the Coarse (57) and Fine (92) habitats. However, despite the higher species count, total faunal (benthos + fish) biomass was lowest in the OWF (~662 mmol C m^{-2}) versus ~2047 for the Coarse and ~12894 for the Fine sediment site. The difference in macrofaunal biomass between OWF and Coarse food web was mostly due to the absence of adult heart urchins (*E. cordatum*) within the OWF community.

As a result of this high species richness, the OWF food web had many more links (853 total, 726 internal, Table 6) than Coarse (536 total, 447 internal) and Fine, but it had lower connectance (0.17 vs ~ 0.22-0.23) and lower cycling (via Finn's index) — indicating less internal recycling and possibly lower stability/maturity. Overall, though, the carbon throughflow (*TST*), the total amount of carbon moving through the food web, in the OWF was 513.9 ± 0.2 mmol C m^{-2} d^{-1}, nearly identical to the Coarse site (512.6 ± 2.0 mmol C m^{-2} d^{-1}), but lower than the Fine site (698.7 ± 11.5 mmol C m^{-2} d^{-1}).

Table 6. Food web indices. Calculated food web indices based on 1000 randomly sampled solutions of each food web (mean values ± SD). Last three columns show results of bootstrapping test: the percentage of solutions where the value of a given index was higher in food web A than higher B, with the contrasts A and B indicated by the column title. Table adopted from De Borger et al., 2025

Index	Full name	units	Coarse	Fine	OWF	% Coarse > Fine	% Coarse > OWF	% Fine > OWF
TST	Total system throughflow	mmol C m^{-2} d^{-1}	512.57 ± 1.97	698.70 ± 11.47	513.9 ± 0.2	0.00	24.20	100.00
Ltot	Total number of links		453 ± 0	536 ± 0	853 ± 0	0.00	0.00	0.00
Lint	Number of internal links		374 ± 0	447 ± 0	726 ± 0	0.00	0.00	0.00
LD	Link density		11.05 ± 0	11.65 ± 0	13.1 ± 0	0.00	0.00	0.00
Tij	Average link weight	mmol C m^{-2} d^{-1}	1.69 ± 0	1.73 ± 0.02	0.9 ± 0	0.00	100.00	100.00
CI	Connectance		0.23 ± 0	0.22 ± 0	0.2 ± 0	100.00	100.00	100.00
FCI	Revised Finn's cycling index		0.02 ± 0	0.03 ± 0	0.01 ± 0	2.20	100.00	100.00

In summary, the OWF food web displays a high species richness, though many species occur only at low biomass when observed at the relevant spatial scale. This leads to many, but weak connections in

the trophic network. In addition, indices such as connectance, and Finn's cycling index, which were generally lower in the OWF food web, indicate that the network is less stable or less mature than the other food webs (likely a combination of the two).

b. Variation in organic carbon uptake pathways

The uptake patterns of different food sources (organic carbon) by macrofauna differed between the food webs both in absolute quantities (driven by biomass differences), and relative quantities (driven by different functional roles expressed in fauna communities).

In the Coarse site, the large biomass of the deposit-feeding sea-urchin *Echinocardium cordatum* dominated uptake of sediment organic matter (sedOM), which was the main input of organic matter into the benthic food web (Figure 14). This species was also an important input of sedOM in the Fine food web, but here, the abundance of suspension feeders, suspension-deposit feeders, filter feeders, and scavengers results in a more even uptake of different food sources. In the OWF, the *E. cordatum* dominated sedOM uptake is supplemented by the activities of suspension feeders on the hard substrates. The soft-sediment species, present in a much larger area in this food web, still dominated uptake (≈68 %). However, the hard-substrate community on turbine foundations and scour-protection layers accounted for ~26% of uptake of water-column food sources in the OWF, despite these species occurring on only ~0.5 % of the available surface in this food web.

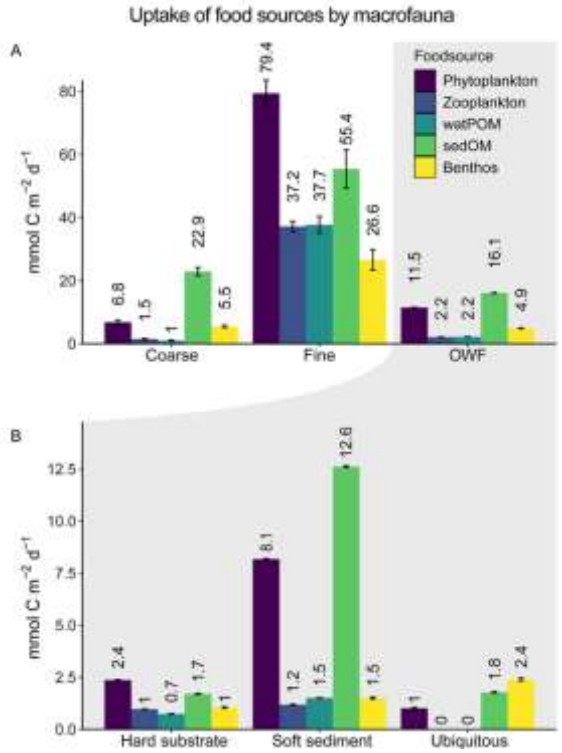

Figure 14. Food source uptake per food web: Breakdown of uptake flows (mmol C m−2 d−1, y-axis) of different food sources (colours) for (A) Coarse, Fine and OWF food webs, and (B) the subcommunities within the OWF food web: the hard substrate community (turbine + SPL), soft sediment community, and ubiquitous species. Error bars represent SD on 10,000 solutions of the Monte Carlo procedure.

The presence of these hard-substrate species also resulted in an increased flow of organic carbon to the sedimentary organic matter pool of about 10 %, when compared to the baseline. This flow was derived from the contribution of hard substrate species to the water column detritus pool, with the assumption that this contribution is in the form of heavier particles, (pseudo-)faeces depositing in the immediate vicinity of the turbine-SPL.

So, the installation of hard substrates in a soft sediment environment creates a new trophic pathway: large biomass of suspension feeders on the hard substrate draws resources from the water column (phyto- & zooplankton), deposits organic matter to the seabed (via faeces/pseudofaeces) and thereby increases benthic carbon input. This supports previous findings of local enrichment, and quantifies the pathway that causes this.

c. Fish production and feeding preferences

The biomass of fish was similar in the OWF food web (4.9 mmol C m^{-2}) and the Coarse food web (4.3 mmol C m^{-2}), despite that absolute prey biomass (macrofaunal biomass) was considerably lower in the OWF food web (see 4.1.a). In the Fine food web, fish biomass was much higher (12.4 mmol C m^{-}), reflecting higher prey availability.

Production of fish was not significantly higher in the OWF (0.12 ± 0.01 mmol C m^{-2} d^{-1}) compared to the Coarse site (0.11 ± 0.01 mmol C m^{-2} d^{-1}), but far lower than the Fine site (0.32 ± 0.02 mmol C m^{-2} d^{-1}). These trends also follow the differences in fish biomass between the different food webs above.

Prey preferences for several fish taxa shifted between the different food webs, indicating flexibility in the consumption behaviour of these fish in response to local availability of prey. In the OWF specifically, fish showed incorporation of hard-substrate prey, with many species deriving a portion of their diet from turbine-associated prey, predominantly in the form of crustaceans. This differed between fish groups, where *Callionymiformes*, *Gobiformes* and *Scombridae* derived between 7 and 10 % of their uptake from the turbine-SPL, *Cottoidei* prey consisted for 72 % of turbine-SPL species.

Summarized, the biomass of fish in the OWF was similar to the Coarse sandy environment, despite higher potential prey biomass in the latter. Prey from the hard-substrate communities also contribute significantly to the diets of several fish taxa. This implies that feeding in the OWF is energetically beneficial for fish as the lower prey biomass does sustain a relatively high fish biomass, however we could not prove elevated secondary production in the OWF as a result of this. This may be the result of the relatively sparse data available about fish biomass within the OWF, and definitely close to the turbine. The available data came from point observations by divers and trawls collected ~250 m away from the turbines, where experimental fishing was allowed. This may have resulted in an underestimation of the fish stocks by not sampling the dense aggregation of fish that are observed by divers in the immediate vicinity of offshore wind turbines.

d. Recommendations

Offshore wind farms (OWFs) are active ecological modifiers that alter the structure and functioning of coastal food webs. By introducing hard substrates that support dense communities of suspension feeders, OWFs establish new trophic pathways linking the water column to the seafloor and enhance carbon deposition in surrounding sediments. These processes influence biodiversity, productivity, and carbon cycling at the ecosystem scale, highlighting the need for integrated management approaches.

- OWFs should therefore be recognized as functional ecosystem components within marine spatial planning. **Environmental impact assessments should move beyond species inventories to include trophic and biogeochemical interactions**, ensuring that energy development is evaluated in terms of its effects on food-web dynamics and carbon flows.
- Because the studied OWF food web appeared less mature and likely still evolving**, long-term ecological monitoring is essential**. Programs should track changes in species composition, carbon fluxes, and trophic connectivity throughout the operational life of wind farms.
- As offshore wind development expands, the ecological effects of multiple farms may accumulate across regions. This **calls for cumulative-impact assessments and regional-scale models** that integrate trophic processes and carbon dynamics.
- This type of research requires standardized, interdisciplinary data collection. **Consistent monitoring across wind-farm sites** will enable comparison, improve model accuracy, and guide adaptive management strategies.

4.2 Marker development for OM endmembers

a. Endmember characterisation

Distinct $\delta^{15}N$ signatures and AA nitrogen contents were identified for each endmember (FP *Mytilus edulis*, FP *Metridium senile*, phytoplankton, and zooplankton). These values established clear isotopic baselines for use in the unmixing analyses. Tyr was only detectable in sufficient quantities for FP *Metridium* and zooplankton (Figure 15).

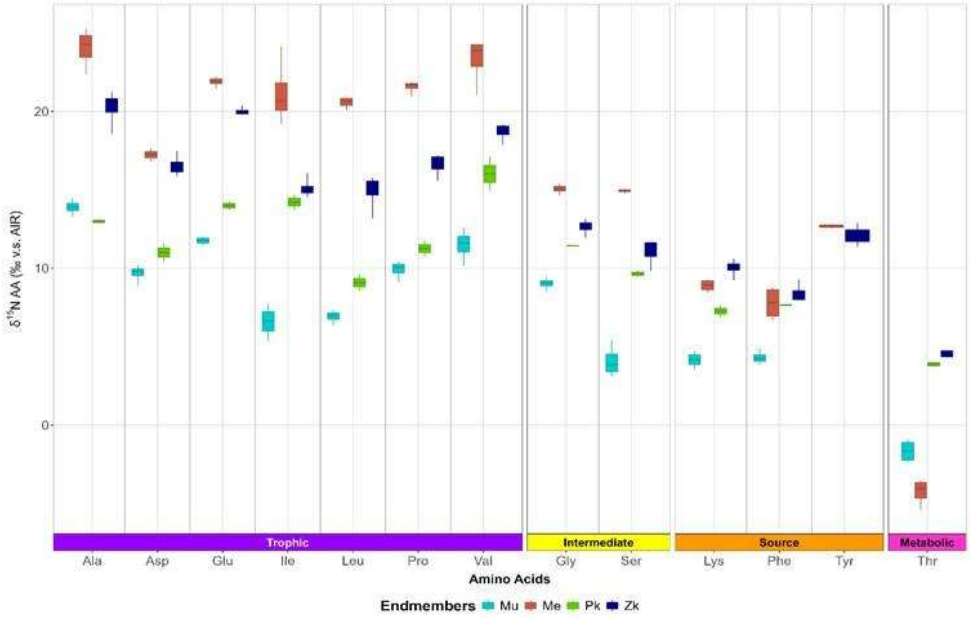

Figure 15. Box plots of $\delta^{15}N$ values (‰ vs. AIR) for AA from each endmember: FP Mussel (Mu, light blue), FP Metridium (Me, coral red), phytoplankton (Pk, green), and zooplankton (Zk, dark blue). AA are grouped by isotopic behaviour: Trophic (purple), Intermediate (yellow), Source (orange), and Metabolic (pink)

b. Tracer selection

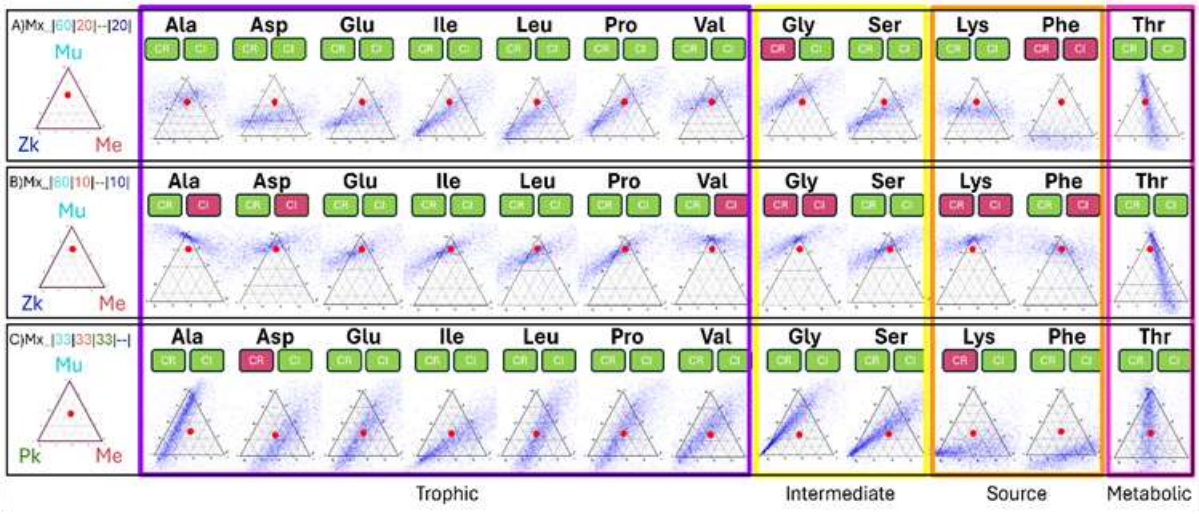

Figure 16. Ternary diagrams showing $\delta^{15}N$-AA tracer predictions for three artificial mixtures: 1) 60% FP Mussel, 20% FP Metridium, 20% Zooplankton; 2) 80% FP Mussel, 10% FP Metridium, 10% Zooplankton; 3)33% FP Mussel, 33% FP Metridium, 33% Phytoplankton. Sources ar Sources are color-coded: FP Mussel (light blue), FP Metridium (coral red), Phytoplankton (green), and Zooplankton (dark blue). AA are grouped by function: Trophic (purple), Intermediate (yellow), Source (orange), Metabolic (pink). CR (Consensus Ranking >63%) and CI (Conservativeness

Index: good/fair) are highlighted with green squares; red squares indicate failure. Red dots mark the theoretical mixture values.

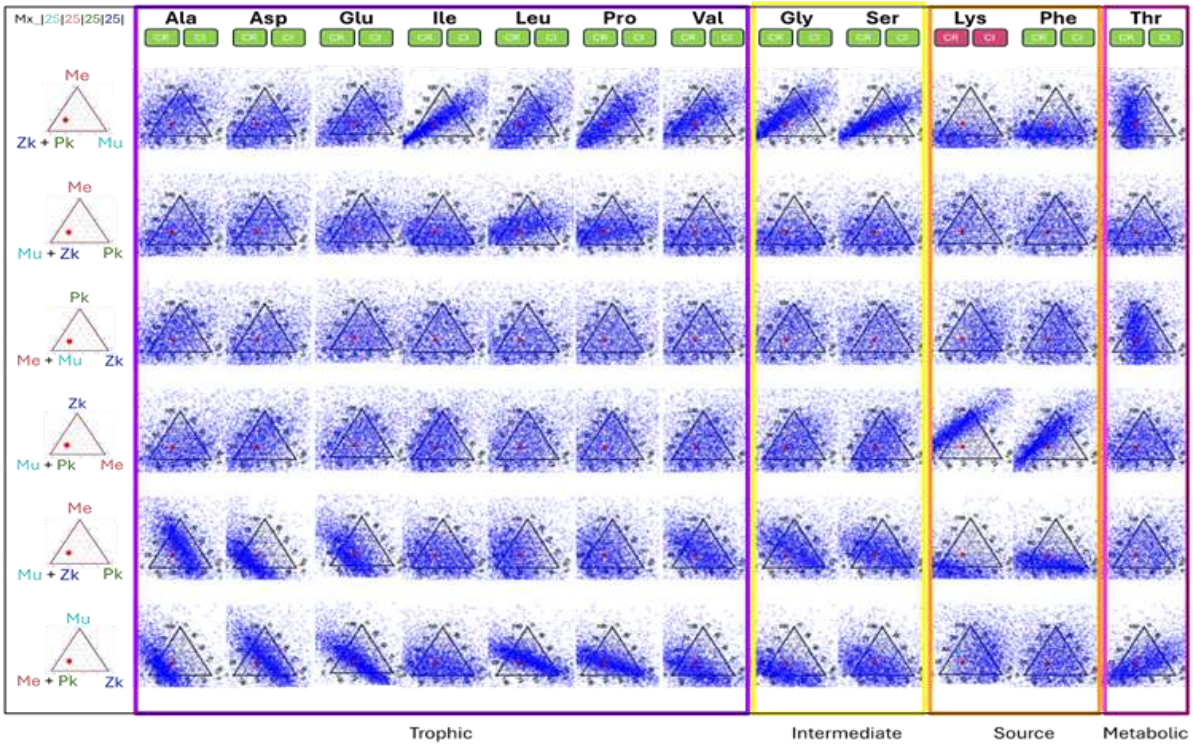

Figure 17 Ternary diagrams showing δ^{15}N-AA tracer predictions for a 4-source mixture (25% each: FP Mussel (light blue), FP Metridium (coral red), Phytoplankton (green) and Zooplankton (dark blue)). AA are grouped by function: Trophic (purple), Intermediate (yellow), Source (orange), Metabolic (pink). Green squares indicate CR >63% and acceptable CI (good/fair); red squares indicate test failure. Red dots show the theoretical solution.

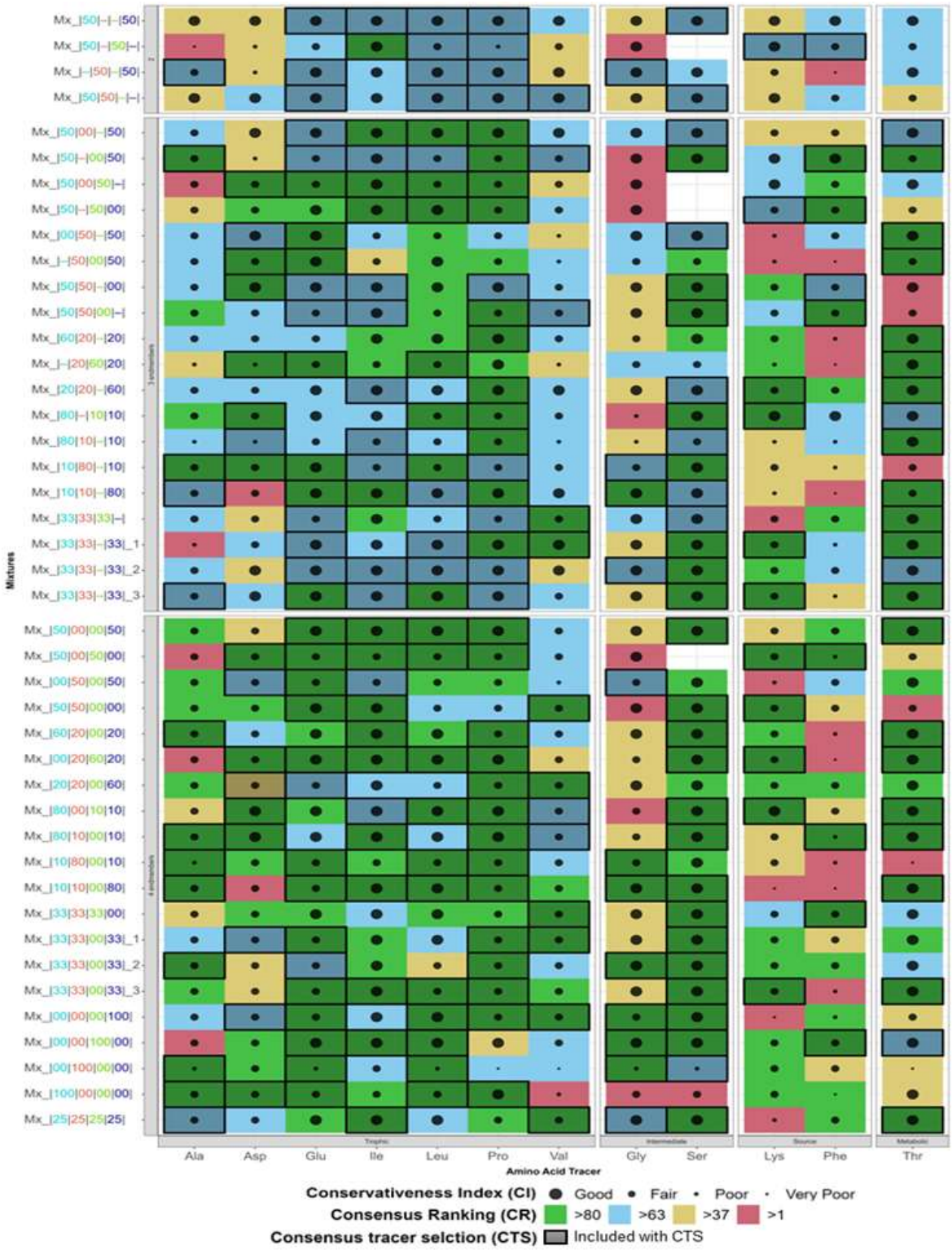

Figure 18. Heatmap showing CI (Conservativeness Index), CR (Consensus Ranking), and CTS (Consistency-Based Tracer Selection) results for each δ^{15}N-AA tracer across artificial mixtures of increasing endmember complexity (top to bottom). Mixtures combining FP Mussel (light blue), FP Metridium (coral red), phytoplankton (green) and zooplankton (dark blue). CI is represented by dot size (larger = higher CI).CR values (%) are color-coded: green (>80%), light blue (>63%), yellow (>37%), red (>1%). CTS is indicated by black boxes, identifying consistent and stable performing tracers (error < 0.05).

c. Unmixing performance

Three tracer selection approaches were tested: (i) the Ala–Thr pair, (ii) all available AA, and (iii) the model-based CI/CR/CTS framework (Fig. 19 - 20). The CI/CR/CTS-selected tracers produced estimates closest to theoretical source contributions, with narrower uncertainty ranges and lower Root Mean Square Error (RMSE) values. The Ala–Thr method consistently showed the greatest deviation and variability as mixture complexity increased. The All-AA approach performed moderately well but was more sensitive to overdetermined scenarios (i.e., inclusion of zero-contribution endmembers). In contrast, the CI/CR/CTS method maintained stable performance even in complex or uncertain conditions, demonstrating its robustness and precision (Figure 21).

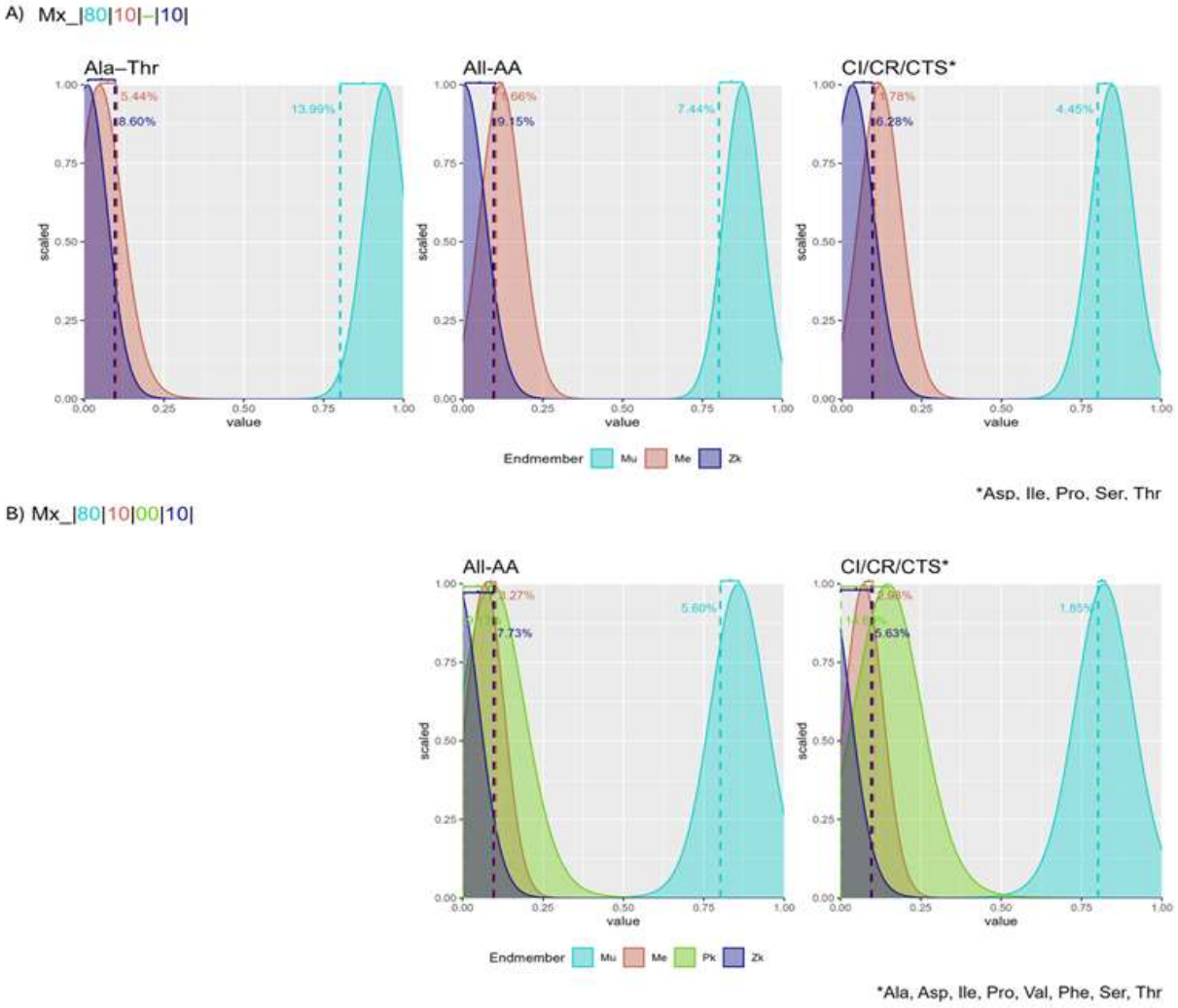

Figure 19. Unmixing results for the same artificial sample using FingerPro. A) Density plot with three endmembers: 80% FP Mussel (light blue), 10% FP Metridium (coral red), 10% Zooplankton (dark blue). B) Same as A, but with added complexity: 0% Phytoplankton (green) included as a fourth endmember. Vertical lines mark the theoretical contributions. Distributions (0–1) indicate proportional contributions. Each panel (left to right) shows unmixing using Ala and Thr only, all AA, and CI/CR/CTS-selected AA. Deviation errors (as %) between theoretical and mean estimates are shown per endmember in corresponding colours. AA used in the "CI/CR/CTS" approach are listed below each graph (*).

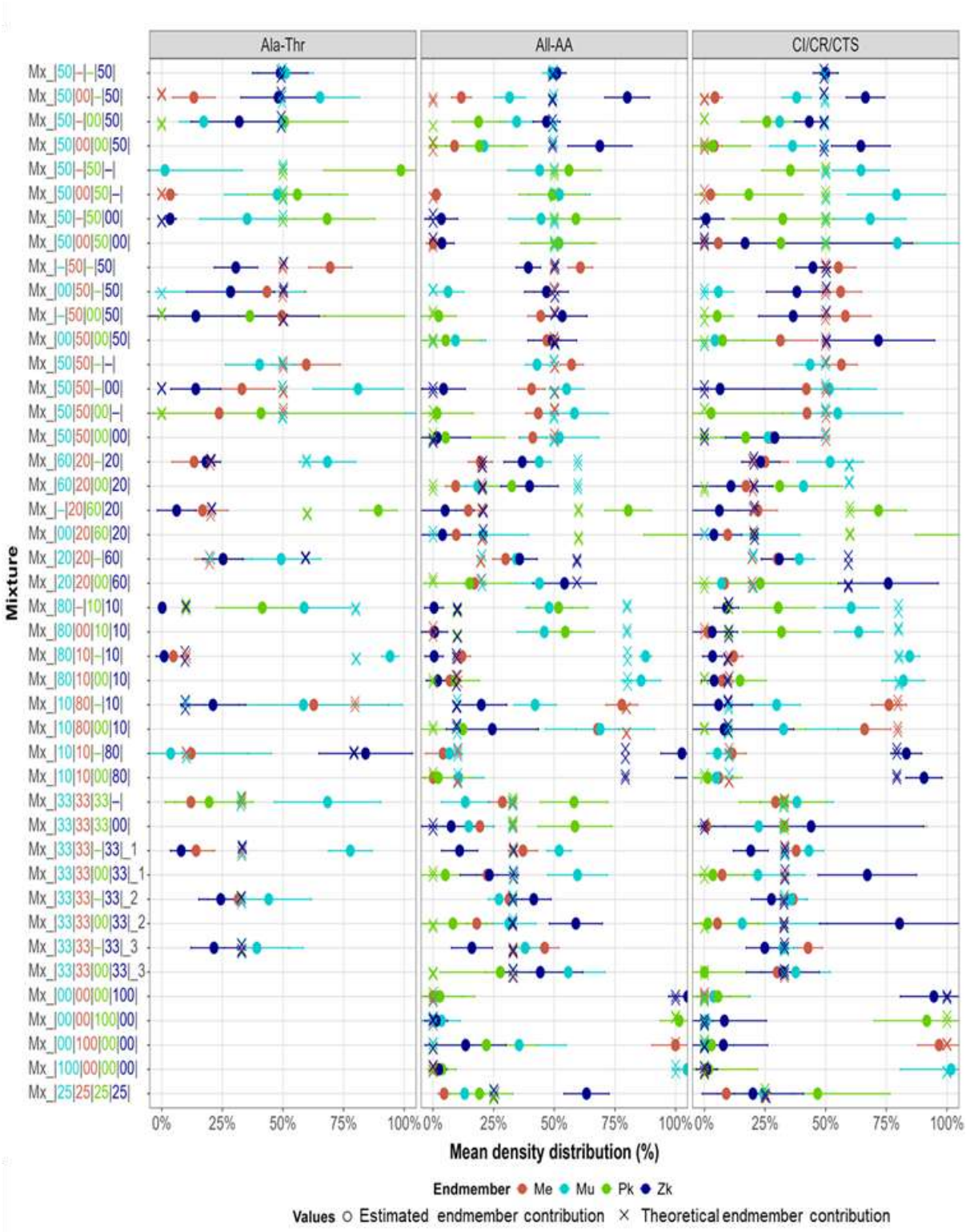

Figure 20. Summary of unmixing probability density results across mixtures. Unmixing approaches are grouped as: (1) "Ala–Thr", (2) "All AA", and (3) "Cl/CR/CTS". Each row represents a mixture with known theoretical contributions from FP Mussel (Mu = light blue), FP Metridium (Me = coral red), phytoplankton (Pk = green), and zooplankton (Zk = dark blue), indicated by "X" markers. Estimated contributions (% mean ± confidence interval) are shown as coloured points with horizontal error bars

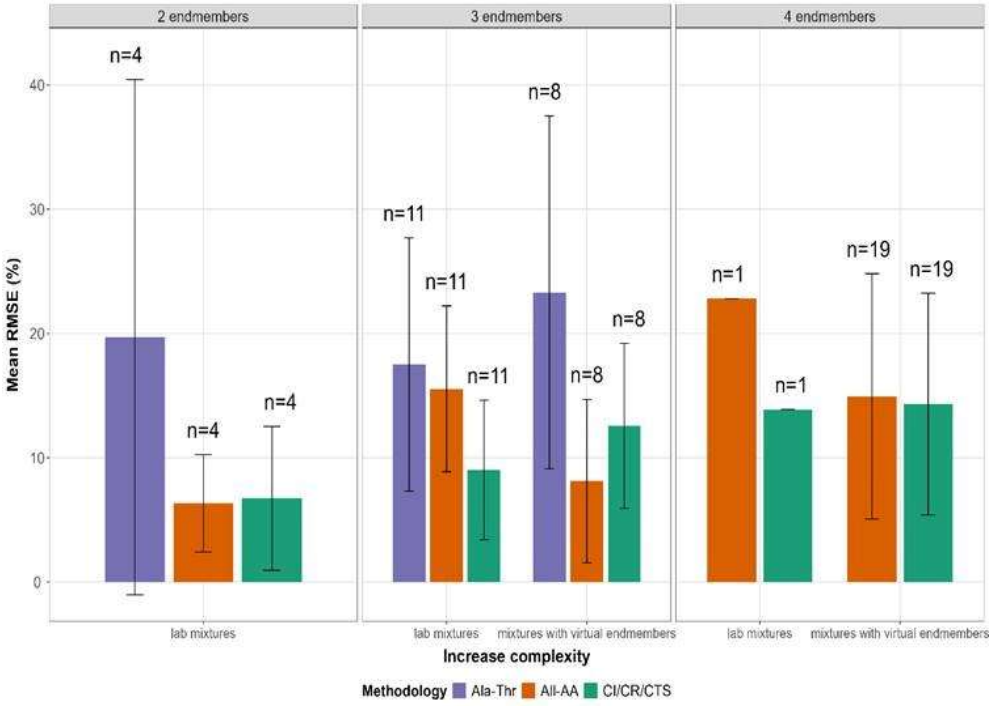

Figure 21. Root Mean Square Error (RMSE) of source contribution estimates, grouped by the number of endmembers (left to right) and by mixture type (lab-based vs. virtually added endmembers). Bars show mean RMSE (%) ± standard deviation for each method: "Ala-Thr" (purple), "All-AA" (orange), and "CI/CR/CTS" (green). Sample sizes (n) for each group are indicated above the bars. Lower RMSE values indicate higher estimation accuracy.

d. Recommendation on methodology

Accurately distinguishing multiple OM sources in marine environments, including faecal pellets, zooplankton, and phytoplankton, is essential for understanding OM pathways and their responses to human activities such as bivalve aquaculture and offshore renewable energy development. Based on the results of this study, t**rophic amino acids (Glu, Ile, Leu, Pro) and complementary Ser and Thr are recommended as the most reliable tracers for future ^{15}N-AA-based unmixing studies in similar marine systems. Systematic tracer selection using the CI/CR/CTS framework** is strongly advised when considering more than three endmembers as it improves accuracy, minimizes bias, and allows the inclusion of multiple tracers, enabling robust unmixing of complex samples with more than three contributing endmembers. Applying the CI/CR/CTS framework to artificial mixtures enhances the precision of source attribution, supporting more informed management of nutrient cycling, sediment dynamics, and overall ecosystem health. **On natural samples, CI/CR/CTS opens the possibility of wider tracer selection and greater understanding of tracer behaviour before applying any unmixing.** However, for natural samples, Phe-normalization must be considered as the endmembers, and the mixture signals are not 100% equal.

4.3 Quantification of fouling-fauna derived OM in water and sediment

a. Organic carbon measurements – water column

Seasonal total particulate organic carbon (TOC) values show higher concentrations in April than June and October. Highest levels of TOC are found at 10 m depth in April with a value of 1115.21 mg L^{-1}. Remarkably, TOC concentration values at 5 m depth are similar in April (708.153 mg L^{-1}) and October (674.200 mg L^{-1}) (Fig. 22)

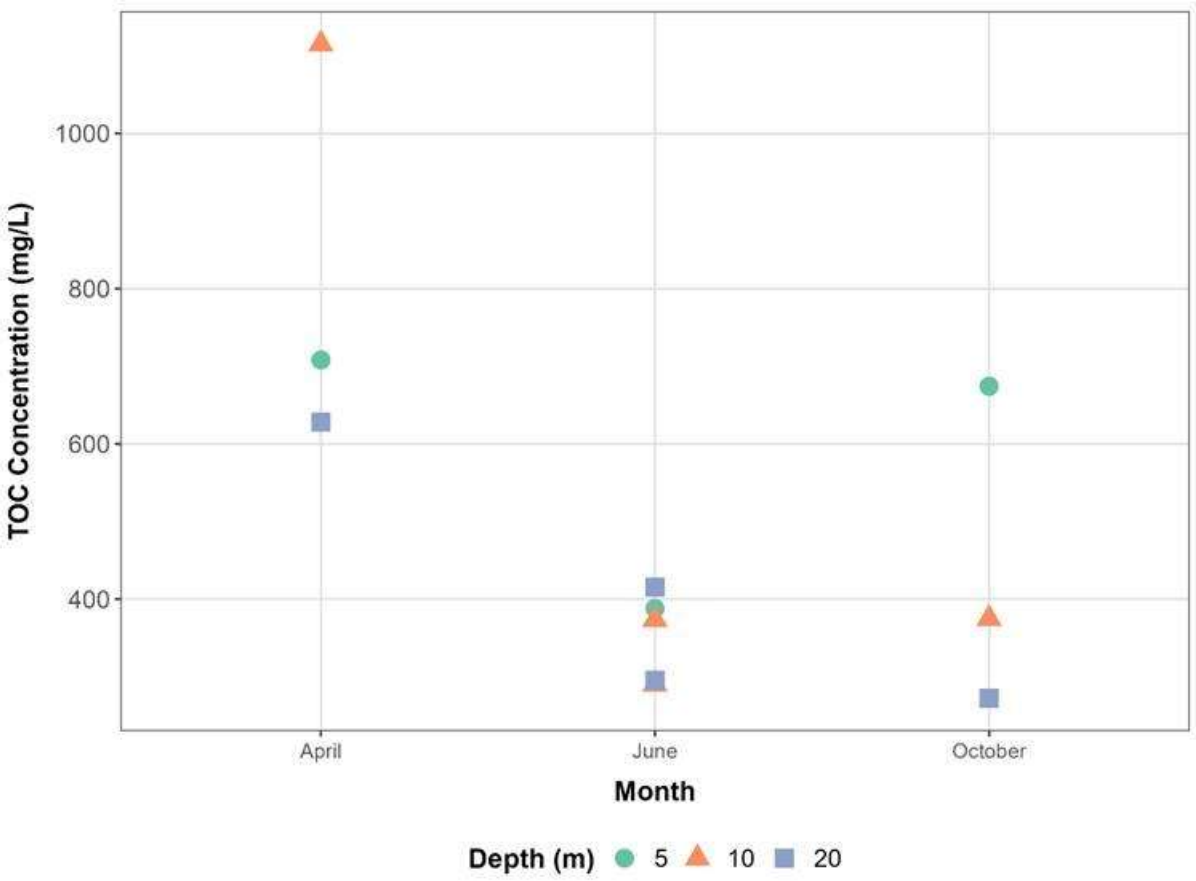

Figure 22. Total Organic Carbon (TOC) concentrations in bulk POM filters collected during the same seasonal periods as the SPM trap deployments (April, June, and October). Sampling depths are indicated by symbol and colour: green circles for −5 m, orange triangles for −10 m, and purple squares for −20 m.

b. Organic carbon measurements – sediment trap

When analysing the carbon content of the SPM trap samples the Total carbon (TC) values only reach up to 5%, with the highest mean value observed in June at 5.71%, followed by April (5.15 %), and is lowest in October (1.6%). This indicates that the remaining mass, nearly 94 % - 98 % of the sample, is composed primarily of mineral material, such as silica (sand), rather than carbon-rich matter. These results highlight that mineral inputs dominate the SPM trap flux throughout the sampling period. Values per sediment trap are indicated in Table 7.

Table 7. Total Carbon (TC), Organic Carbon (OC), Inorganic Carbon (IC), and downward Organic Carbon flux (g OC m^{-2} d^{-1}) measured in SPM traps during April, June, and October 2022. Values correspond to paired sediment trap deployments (A and B) for each month

Sediment trap		Date deployment	Date collection	Total carbon content (%)	Organic carbon content (%)	Inorganic carbon content (%)	Downward OC flux (g OC/m²/d)
April_2022	A	27/04/2022	29/04/2022	5.47%	3.70%	1.77%	7.159
April_2022	B	27/04/2022	29/04/2022	4.82%	3.52%	1.30%	8.307
June_2022	A	27/06/2022	29/06/2022	6.38%	3.77%	2.61%	19.258
June_2022	B	27/06/2022	29/06/2022	5.04%	4.18%	0.86%	10.974
Oct_2022	A	17/10/2022	21/10/2022	1.19%	1.09%	0.10%	10.132
Oct_2022	B	17/10/2022	21/10/2022	2.00%	1.26%	0.74%	4.167

For the TC fraction, OC constitutes the larger portion of the carbon pool, with values of 3.61% (April), 3.98% (June), and 1.18% (October) in all months. IC makes up the remaining fraction, contributing 1.54% in April, 1.74% in June, and 0.42% in October, but with higher variability, particularly in June, where IC shows a larger standard deviation (±1.24%) (Figure 23).

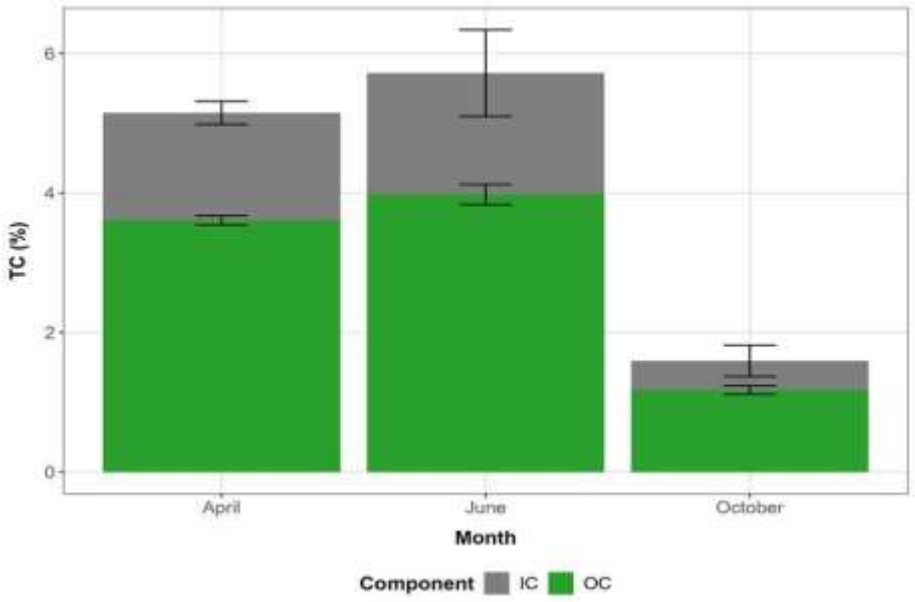

Figure 23. Seasonal variation in carbon fractions of SPM trap material. Bars show mean Organic Carbon (OC) and Inorganic Carbon (IC) contributions to Total Carbon (TC) for April, June, and October, with standard deviations indicated. TC remains low across all seasons, peaking in June at 5.71% (April: 5.15%; October: 1.6%). OC consistently represents most of the carbon content, while IC contributes a smaller and more variable fraction. The low TC values indicate that the collected SPM is dominated by inorganic material, with roughly 94–98% of the total mass composed of mineral particles such as silica.

Downward OC fluxes derived from the SPM trap samples show clear seasonal variability as well as differences between traps A and B per month. In April, OC fluxes are moderate and similar between the two traps, with 7.16 g OC m^{-2} d^{-1} in trap A and 8.31 g OC m^{-2} d^{-1} in trap B. Fluxes increase sharply in June, when trap A reaches the highest value observed across the sampling period (19.26 g OC m^{-2} d^{-1}), while trap B also shows an elevated flux of 10.97 g OC m^{-2} d^{-1}. By October, downward OC fluxes decline again, with trap A recording 10.13 g OC m^{-2} d^{-1} and trap B decreasing to 4.17 g OC m^{-2} d^{-1}. Overall, the pronounced June peak suggests enhanced mid-year export of particulate organic matter, while April and October exhibit more moderate fluxes and stronger differences between the two traps (Fig. 24).

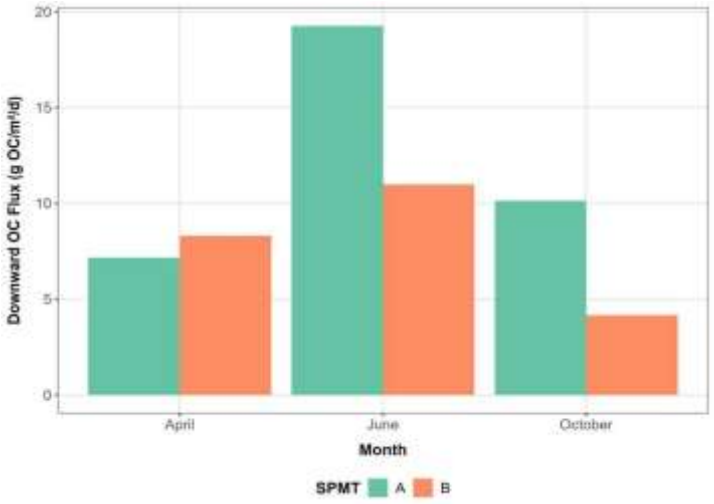

Figure 24. Downward Organic Carbon (OC) fluxes for SPM traps A and B during April, June, and October. Bars represent mean downward OC flux (g OC m^{-2} d^{-1}) for each trap and month. OC fluxes are highest in June, particularly in trap A (19.26 g OC m^{-2} d^{-1}), with lower and more comparable values in April and a marked decline in October. These patterns reflect strong seasonal variation in the downward transport of organic matter.

c. Endmember contribution – sediment trap

We analysed the δ^{15}N-AA values from the individual endmembers considered and the SPM trap samples obtained from the CSIA-AA extraction. The AA-N content (expressed on a carbon basis) was derived from the measured peak area. In this case, natural samples, we considered the baselines correction with Phenylalanine (Phe). Phe was chosen because it preserves the δ^{15}N value of the nitrogen source at the base of the food web (McClelland and Montoya 2002; Chikaraishi et al. 2007) (Table 8). Therefore, the value of δ^{15}N-Phe was subtracted to all the other δ^{15}N-AA values.

To determined which ^{15}N-AA tracers, have the best discriminative potential for source apportionment on each case, the CI/CR/CTS approach was followed (Table 9). Across all sampling periods, Asp and Glu consistently appeared within the trophic category Intermediate AA such as Gly and Ser were selected for most samples, whereas source AA, particularly Lys, were included whenever they showed stable δ^{15}N patterns indicative of baseline nitrogen signatures. Metabolic AA, Thr, was selected only in specific cases where their variability contributed meaningful diagnostic information. The resulting combinations differ among months and between traps, indicating that the best-performing AA for unmixing vary with seasonal changes in organic matter composition and nitrogen cycling processes.

Table 8. Classification of AA according to the nitrogen isotope patterns between producer and consumers during trophic transfer. ($\Delta^{15}N = \delta^{15}N$consumer - $\delta^{15}N$producers)

Source AA	$\Delta^{15}N \approx 0$ ‰	Phenylalanine (Phe) Lysine (Lys) Tyrosine (Tyr)
Trophic AA	$\Delta^{15}N >> 0$ ‰	Alanine (Ala) Aspartic acid + asparagine (Asp) Glutamic acid + glutamine (Glu) Leucine (Leu) Isoleucine (Ile) Proline (Pro) Valine (Val)
Intermediate AA	$\Delta^{15}N > 0$ ‰	Glycine (Gly) Serine (Ser)
Metabolic AA	$\Delta^{15}N < 0$ ‰	Threonine (*Thr*)

Although multiple trophic, intermediate, and metabolic amino acids were selected, these tracers are mechanistically redundant because their discriminatory power arises from the same underlying processes, primarily trophic fractionation during nitrogen transfer. As a result, several AA may convey similar isotopic information which can be seen on the graphic representation with ternary diagram when comparing the CI results of each AA. However, this redundancy is advantageous: if one AA performs poorly or is not detected, others within the same functional group can still provide reliable information. This becomes particularly important when increasing the number of endmembers in the unmixing model, as having multiple robust tracers enhances model stability and improves the ability to distinguish among complex mixtures of organic matter sources.

After the ^{15}N-AA tracer selection with model independent CI/CR/CTS framework, the isotopic unmixing model was applied to the SPM trap samples (FingerPro v2; Lizaga et al. 2018, 2020b). The resulting endmember compositions for each trap are shown in Figure 25, with values ranging from 0 to 100 %. In April, the SPM mixtures were dominated by FP Mussel and zooplankton, with April_A composed of 47% Mu and 43% zooplankton, and April_B showing an even stronger zooplankton contribution (68%) alongside smaller fractions of FP Mussel (21%) and Phytoplankton (11%).

Table 9. Amino acids (AA) selected before unmixing for SPMT samples collected in April, June, and October. Listed AA represent those included in the isotopic unmixing model after applying δ^{15}N-Phe baseline correction. AA are classified according to the nitrogen isotope patterns during trophic transfer: Trophic, Intermediate, Source and Metabolic

Sedument trap sample	CI/CR/CTS selected AA used for each unmixing - Phe corrected			
	Trophic	Intermediate	Source	Metabolic
April_A	Asp, Glu, Ile	Gly, Ser	Lys	
April_B	Asp, Glu, Ile, Leu, Pro	Gly, Ser	Lys	Thr
June_A	Ala, Asp, Glu, Ile, Leu, Pro	Ser	Lys	
June_B	Ala, Asp, Glu, Pro	Gly, Ser		Thr
October_B	Asp, Glu, Ile,	Gly, Ser	Lys, Tyr	

In June, both traps showed a marked shift toward FP Jassa material, with FP Jassa contributing 57% in June_A and 45% in June_B. FP Mussel remained the secondary contributor in both traps (41% and 40%, respectively), whereas Phytoplankton accounted for only minor fractions (2–15%). No contributions from FP Metridium or zooplankton were detected in June. In October, only trap B could be analyzed due to extraction failure in October_A. October_B exhibited a mixed composition dominated by FP Mussel (62%), followed by Phytoplankton (20%), zooplankton (16%), and a small contribution from FP Metridium (2%). Overall, these results highlight pronounced seasonal dynamics in organic matter sources to the SPM traps, including strong FP Jassa dominance in early summer and more heterogeneous mixtures in autumn.

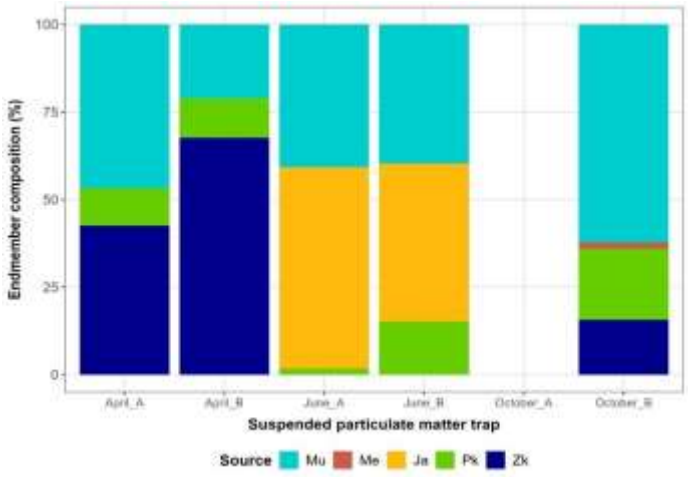

Figure 25. Endmember composition (%) of suspended particulate matter trapped in April, June, and October, derived from isotopic unmixing of ^{15}N-AA data using FingerPro v2. Bars represent proportional contributions (0–100%) to each SPM trap from the five endmembers considered: FP Mussel (Mu, light blue), FP Metridium (Me, coral red), FP Jassa (Ja, yellow), phytoplankton (Pk, green), and zooplankton (Zk, dark blue). October_A is absent because CSIA-AA extraction failed. April samples are dominated by FP Mussel and zooplankton, June samples show strong FP Jassa contributions, and October_B exhibits a mixed composition dominated by FP Mussel.

Because the isotopic unmixing model incorporates the carbon content of each endmember, the resulting source contributions are expressed directly in carbon units. This allows the proportions to be translated straightforwardly into endmember-apportioned downward organic carbon (OC) flux for each trap without additional conversion steps. The OC flux patterns show strong temporal variability (Figure 26). In April, modest OC fluxes (7.159 – 8.307 g OC m^{-2} d^{-1}) were dominated by FP Mussel and Zooplankton, with smaller inputs from Phytoplankton. June exhibits the highest fluxes of the time series, particularly in June_A (19.258 g OC m^{-2} d^{-1}), driven primarily by a large FP Jassa contribution and secondarily by FP Mussel. June_B shows a similar structure but with a lower total flux (10.974 g OC m^{-2} d^{-1}). In October, the absence of AA data for October_A results in the total OC flux being shown as NA, whereas October_B presents a low flux (4.167 g OC m^{-2} d^{-1}) composed mostly of FP Mussel with minor contributions from Phytoplankton and Zooplankton. Overall, these flux-weighted results emphasize strong seasonal shifts, including pronounced FP Jassa driven OC export in early summer and reduced flux with more heterogeneous sources in autumn.

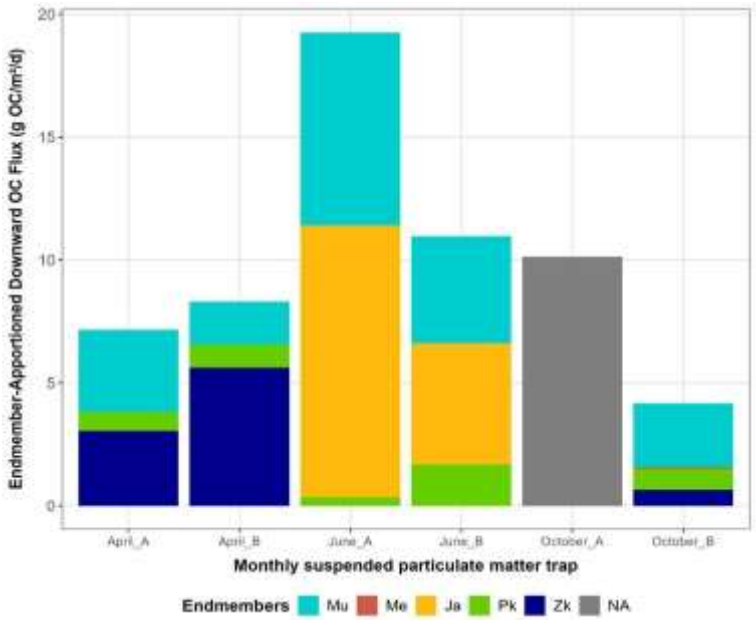

Figure 26. Endmember specific downward organic carbon flux (g OC m^{-2} d^{-1}) for monthly suspended particulate matter traps based on δ^{15}N-AA isotopic unmixing. The unmixing model accounts for the carbon content of each endmember, allowing direct conversion of source contributions into carbon flux. Endmembers include FP Mussel (Mu, light blue), FP Metridium (Me, coral red), FP Jassa (Ja, yellow), phytoplankton (Pk, green), and zooplankton (Zk, dark blue). Grey bars indicate months with no amino-acid data (October_A). Seasonal patterns show high OC export in June dominated by FP Jassa, moderate mixed-source fluxes in April, dominated by FP Mussel and Zooplankton and lower fluxes in October dominated by FP Mussel.

d. Recommendations

Improve future analyses and strengthen the reliability of endmember apportionment. First, **extraction procedures should be refined** to ensure consistent recovery of AA, as illustrated by the failed October A sample; incorporating duplicate extractions and additional quality-control steps would reduce the risk of data loss. Increasing the temporal resolution of SPM trap deployments, particularly between June and October, would help capture short-term ecological and hydrodynamic variability that strongly influences organic carbon sources. **To better interpret these temporal changes, SPM trap deployments should be accompanied by environmental monitoring** (e.g.,

temperature, currents, chlorophyll-a, benthic activity). The **endmember** library would also benefit from expansion, including a broader range of phytoplankton, zooplankton, and other fouling fauna organisms. Although multiple trophic, intermediate, and metabolic AA may appear mechanistically redundant, retaining this redundancy is recommended because it increases model robustness: if one tracer is noisy or analytically compromised, others can compensate, especially when dealing with a larger number of potential endmembers.

In addition, the **downward organic carbon flux** should continue to be **integrated** directly into **source apportionmen**t, as this provides a more ecologically meaningful interpretation of carbon transfer to depth. Given the overall low carbon content of trap material, improving mass collection, whether through deployment frequency or optimized trap design, would help reduce uncertainty in carbon measurements and isotope analyses. Together, these actions will improve the accuracy, interpretability, and ecological relevance of future SPMT-based AA isotope studies

4.4 Spatial Carbon footprint of a turbine

a. Hydrodynamical results

The simulations were executed for a full spring neap tidal cycle from 01/10/2013 0h tot 15/10/2013 0h. The highest tidal elevation is 1.99 m, while the highest depth-averaged current is 1.14 m/s. The influence of the different turbines is quite clear on the depth mean currents, with a clear decrease in current velocity in the wake of the turbines (Figure 27). The length of the "plume" seems to be in the order of 1 km when the plumes are going the north-eastern direction. It is clear that the plumes enhance each other and that the plumes can reach the turbines that are in the current direction. Near the turbine, the currents are much more disturbed. Remark that due to the nature of the model, with only a grid size of 10 m x 10 m, and the representation of the turbine by one land grid cell, the creation of local turbulence with the horseshoe vortexes is not modelled. For this much higher CFD models are needed. This will probably lead to plumes that have a smaller extension than in reality.

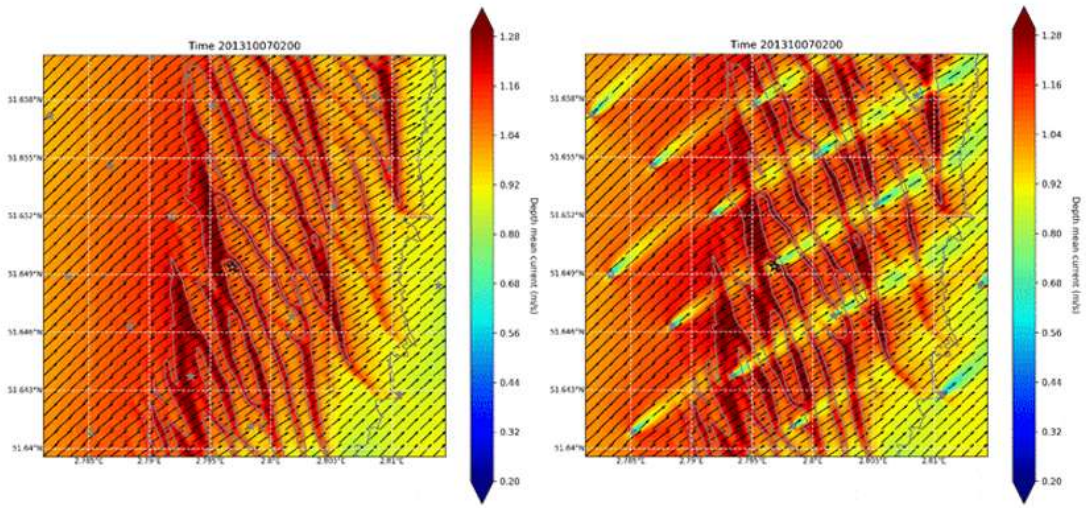

Figure 27. Depth averaged currents (07/10/2013, 02:00) without (left) and with (right) turbines

For the dispersal of particles and the generation of sediment plumes, also the eddy diffusivity is important. The eddy diffusivity is a measure for the general distribution of the particles over the water column, when there is an non-equilibrium. This is the main way that particles can move up to the water column counteracting the fall velocity. Due to the wind turbines, the turbulent diffusivity can be decreased in the wake of the turbines, but can increase also in other moments, mainly during moments where the currents are changing directions (Fig. 28).

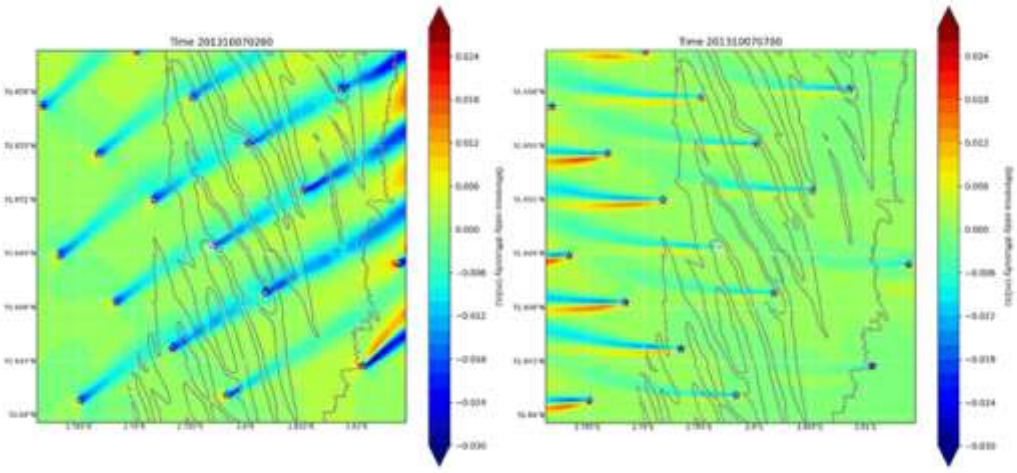

Figure 28. Difference between eddy diffusivity slightly below mid water for simulations without and with turbines at different times during the tide. Left: 07/10/2013, 02:00, right: 07/10/2013, 07:00.

b. Particle tracking of the faecal pellets – single turbine

Although different turbines are present in the wind farm, first simulation have been executed for one turbine for one tidal cycle. During a period of 12.5 h, every 5 minutes a particle was released at 24 points around a turbine for the maximum depth and the minimum depth for the different species. It has been shown that no big differences were found for the results using the 3D currents are the 2D depth averaged currents. The effect of the height of the release of the particles and the fall velocity however is of course important (Fig. 29).

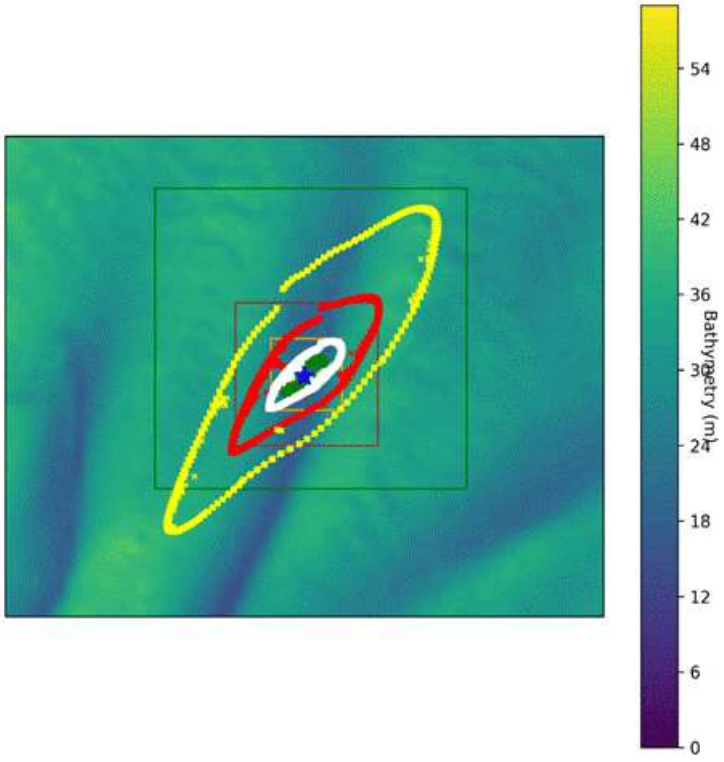

Figure 29. Deposition of FP from 1) Red: Mytilus, fall velocity of 3.5 mm s^{-1}, released at 21 mab; 2) Yellow: Jassa, fall velocity 1.1 mm s^{-1}, 13.5 mab; 3) Green: Metridium, fall velocity 4.5 mm s^{-1}, 6.5 mab; 4) White: Mytilus, fall velocity of 7.7 mm s^{-1}, 21 mab.

It seems that the deposition of the FP are on average some km away from the turbine, at least for the *Mytilus* and *Jassa* FP, due to the height of the release above the bottom and the relatively low fall velocity. The *Mytilus* FP deposition varies between 2213 m to 3311 m for release at 14 mab to 21 mab. The *Jassa* FP, due to the low fall velocity, is deposited the most far away, at a distance of more then 6500 m from the turbine, when released at 14 mab. For the *Metridium*, the deposition of FP varies between 786 m to only 45 m, when released at 6.5 mab or 0.5 mab. All these results are for deposition at neap tide. At spring tide, the distance is larger, for *Mytilus* a factor of 1.65 further away. The time of deposition varies between 120 seconds for *Metridium*, released at 0.5 mab to 12300 seconds, i.e 3.4 hours, for *Jassa*, released at 13.5 mab. This means that the FP are carried away due to the currents but are not coming back, during the turning of the tides.

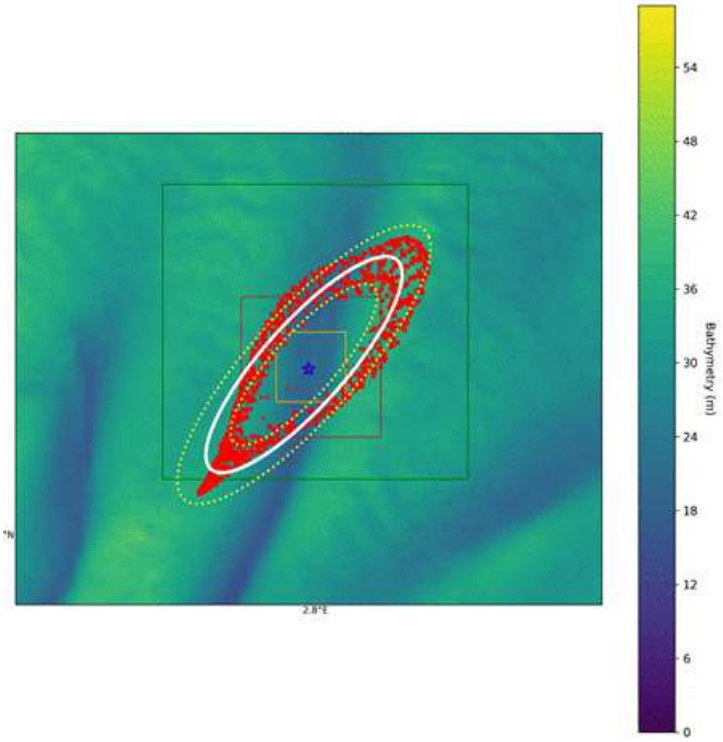

Figure 30. Ellipse around particles, released during a spring-neap tidal cycle. The yellow ellipses include 10% and 90% of the deposition points. The white ellipse includes 50% of the deposition points. Simulation of Mytilus, fall velocity of 3.5 mm s^{-1}, released at 21 mab.

During a full spring-neap tidal cycle, there is some variation of the deposition. To parametrise the results, two ellipses can be calculated, namely an ellipse that includes at least 10 % and 90 % of the deposition points. This means that 80 % of the deposition points are in between the two ellipses (Figure 30; Table 10).

Table 10. Dimension of the ellipses for the FP deposition during a spring-neap tidal cycle. Ws: fall velocity, depth: depth of release of the FP; NE_m, NE_x, NW_m, NW_x: minimum (10 %) and maximum (90 %) of the minimum and maximum axes of the ellipses in northeastern and northwestern direction

Species	Ws (m s^{-1})	Depth (mab)	NE_m (m)	NE_x (m)	NW_m (m)	NW_x (m)
Mytilus	3.5	21.0	3415	5894	1329	2152
	3.5	14.0	2280	3640	922	1499
	7.7	21.0	1565	2665	632	1018
Jassa	1.1	13.5	7038	11200	2382	3612
	1.1	7.0	3617	6241	1395	2257
Metridium	4.5	6.5	820	1433	322	531
	4.5	0.5	32	96	15	36

c. Particle tracking of the faecal pellets – multiple turbines

As multiple turbines are placed in the wind farm and the influence of the turbines on the hydrodynamics could influence the hydrodynamics in neighbouring turbines. Therefore, it is of interest to see whether the fact that different turbines are co-existing in the wind farm influence the dispersal and deposition of the FP. However, the influence of the ellipses of deposition between the results with only one turbine and different turbines are negligible (Figure 31).

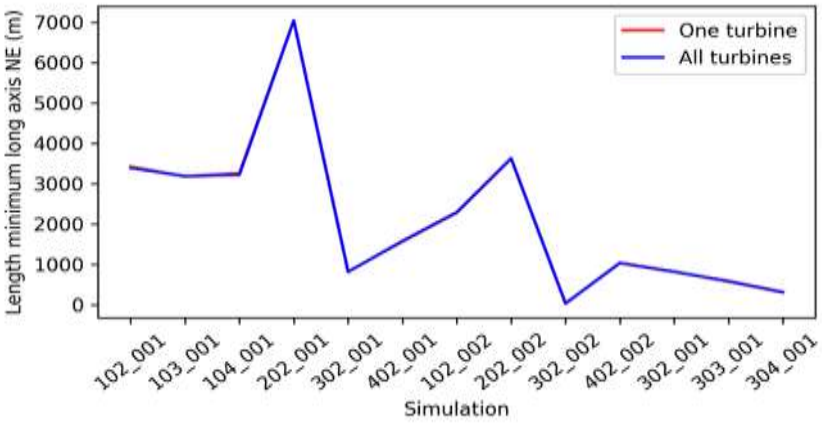

Figure 31. Calculated minimum length of the long axis of the ellipse for different simulation with only one turbine and with different turbines

d. Carbon deposition around a single turbine

To calculate the deposition of carbon, a full spring-neap tidal cycle is simulated. Particles are released at 8 places around the turbines at 2.5 m from the pole , and each 0.5 m between the highest and the lowest point where the species are found. Each hour respectively 240, 224 or 208 particles are release with FP of *Mytilus*, *Jassa* or *Metridium*, representing 1877.9 mgC, 661.6 mgC or 226.2 mgC. During the 14 days of the simulation, a total of 930 kgC is deposited in the neighbourhood of one turbine, of which 67% is coming from the *Mytilus*, 24 % from the *Jassa* and 8 % from the *Metridium*. The deposition shows again an elliptic form with a higher concentration of carbon deposition in the southwestern part of the ellipse (Figure 32).

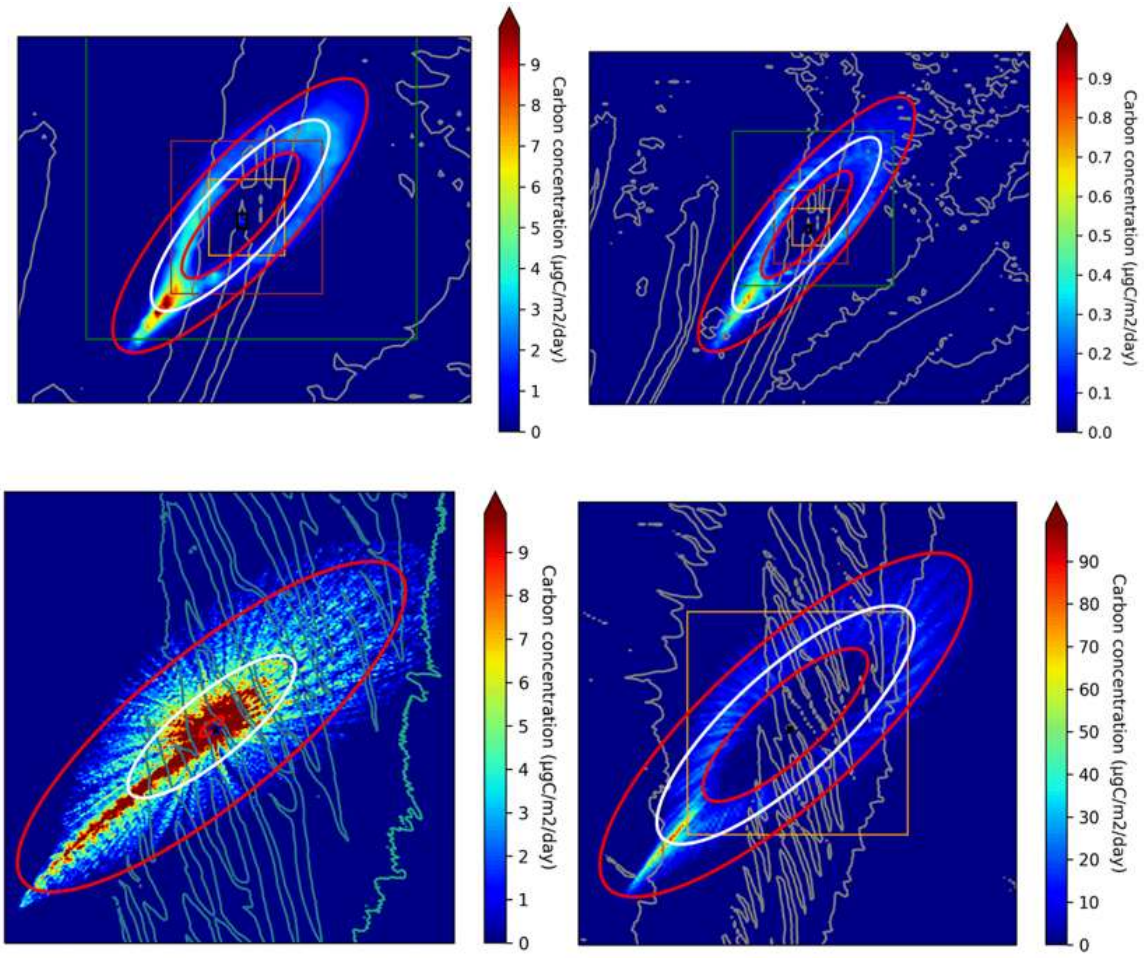

Figure 32. Carbon deposition (µgC m^{-2} day^{-1}) from the Mytilus, with fall velocity 3.5 mm s^{-1} (upper left), Jassa with fall velocity 1.1 mm s^{-1} (upper right), Metridium with fall velocity 4.5 mm s^{-1} (lower left) and Mytilus, with fall velocity 7.7 mm s^{-1} (lower right). The black box is the position of D8 wind turbine and the extent of one grid cell.

The carbon deposition from the FP of the three species combined is showing two clear ellipses from the *Metridium* near the turbine and the *Mytilus* further from the turbine, while the deposition from the *Jassa* further away from the turbine is less clear (Fig. 33).

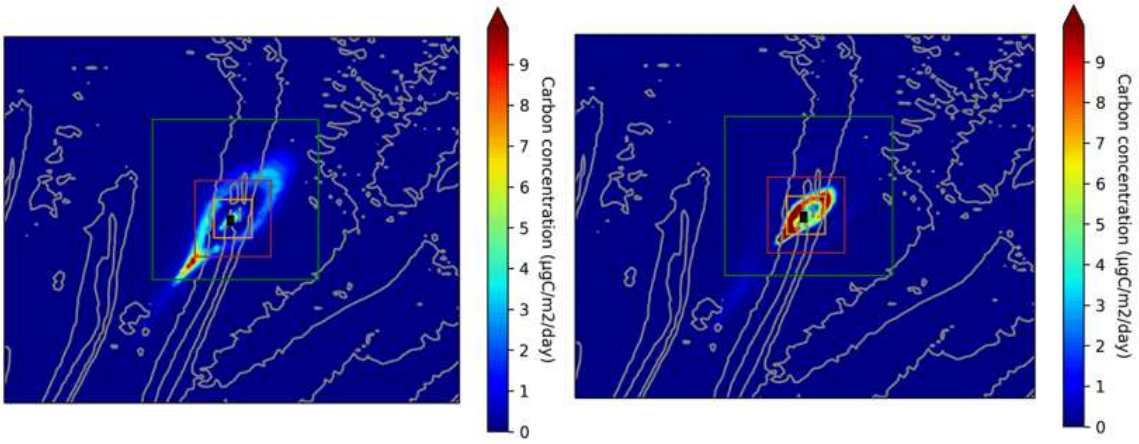

Figure 33. : Carbon deposition (µgC m^{-2} day^{-1}) from Mytilus, with fall velocity mm s^{-1}, Jassa and Metridium (left) and from Mytilus, with fall velocity 7.7 mm s^{-1}, Jassa and Metridium (right). The black box is the position of D8 wind turbine and the extent of one grid cell

The amount of carbon deposition in the ellipse, defined in Figure X (p19) is 5.5 kgC over the period of 14 days (Fig. 34). The carbon is mainly from FP from the *Metridium*.

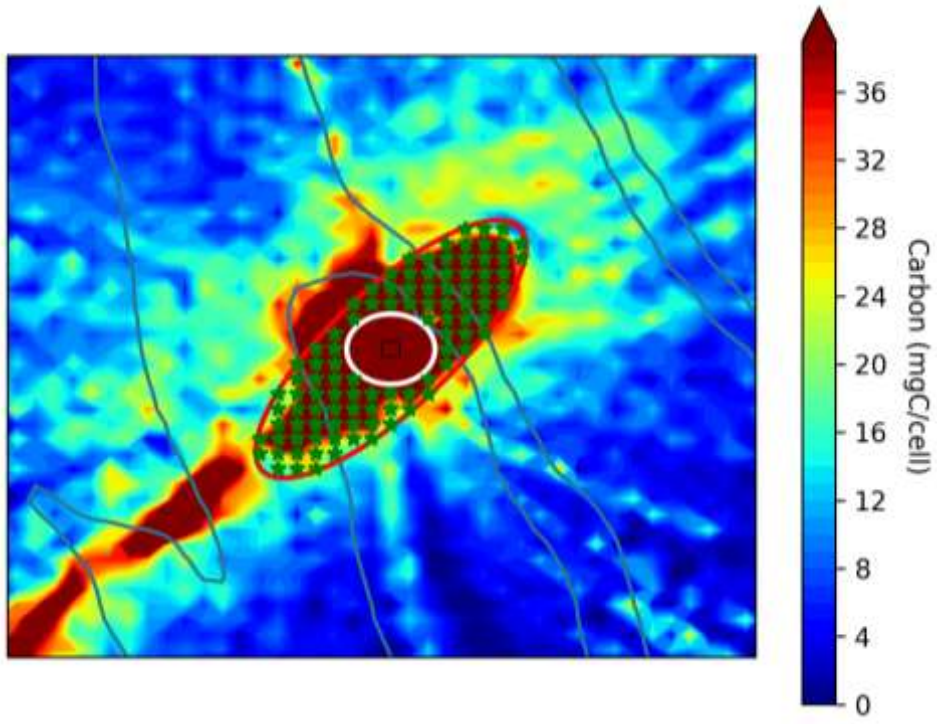

Figure 34. Amount of carbon in the ellipse of the measurements

e. Carbon Deposition from all wind farms

It is clear that the dispersal of the FP of the different species both influence the carbon cycle and the distribution of the carbon at the bottom both in the large scale and in the local scale around the turbine. To look at the large scale, the same distribution of the carbon around the different turbines at the BPNS are copied. This is of course a rough estimation, since the distribution of the FP around the turbines will depend on the local situation, the local water depth, the currents around the turbines

and much more. However to have a first estimation, the carbon concentration is copied and added for all wind turbines on the BPNS.

The effect of the higher fall velocity is clear with higher carbon depositions near the turbines themselves (Figure 35). The extend of the carbon deposition is some km around the wind farms. The maximum carbon deposition is 264 µgC m^{-2} day^{-1}.

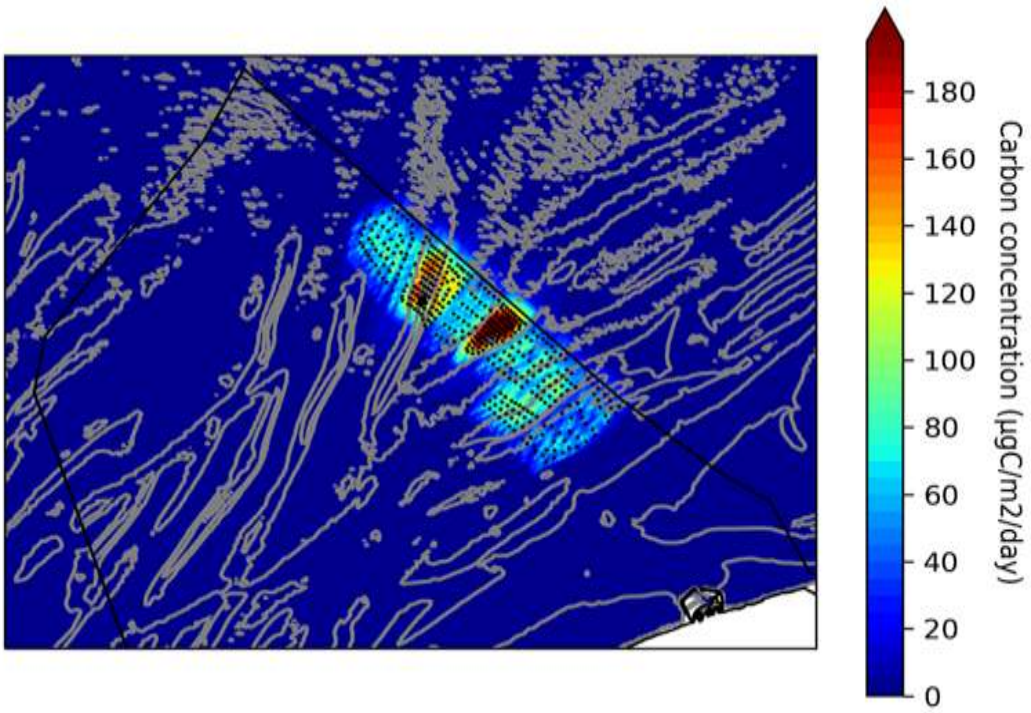

Figure 35. Carbon concentration (mgC m^{-2}) from Mytilus, with fall velocity 7.7 mm s^{-1}, Jassa and Metridium for all wind turbines in the eastern wind farms.

4.5 Carbon accumulation

a. Field measurements

In general, the TOC content of the sediments SW of turbine D5 in C-Power was very low (0.03-0.15 %; Figure 36). A clear seasonal signal was visible in the sediment TOC profiles. In spring, TOC content exhibited higher values in the sediments adjacent to the SPL of the turbine (≤ 25 m) compared to values at 75m from the turbine. In summer, the sediment TOC content had drastically decreased, being similar to the values observed at 15 and 25m from the SPL. However, TOC content still showed enriched sediments at 7 and 25m from the SPL. In autumn, TOC content had decreased further at all locations.

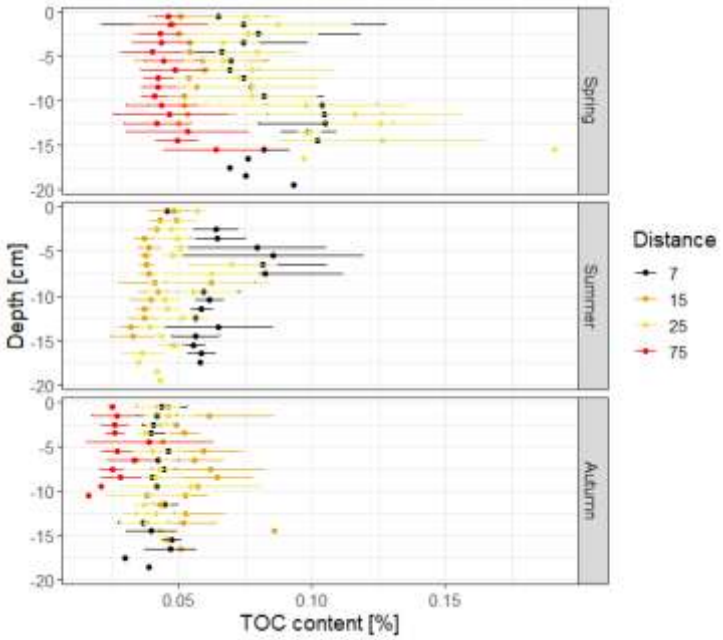

Figure 36. Total Organic Carbon content (%) of the sediment at different distances (in m) from the SPL, in spring, summer and autumn. Note the absence of TOC data at 75m from the SPL in summer.

Macrofauna was sampled in October 2022. Biomass ranged between 0.07 and 3.1 g Corg m^{-2} and was highest at 7 and 15m from the SPL (Fig. 37), largely driven by the presence of the heart urchin *Echinocardium cordatum*.

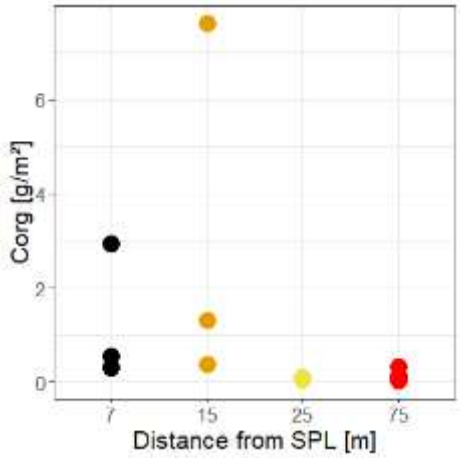

Figure 37. Macrofauna organic carbon biomass in g m^{-2}

b. Spatial upscaling to local turbine effect

Within the footprint of the faecal pellets of the fouling fauna on the foundation of turbine D5 (ellipse shape with long radius 100.5m and short radius 35m, excluding the deposition in the SPL area), 782 kg TOC was observed in spring and 489 kg in autumn (Table 11). Due to the absence of summer TOC data for 75m from the SPL (100.5m from the turbine foundation), no spatial extrapolation for the summer situation was made

Table 11. TOC content in the footprint, expressed per m² and extrapolated over the corresponding ellipse area

Distance to SPL (m)	Distance to turbine (long radius) (m)	Short radius b (m)	Corrected area (m²)	Season	TOC Upper 10 cm (g m^{-2})	TOC content macrofauna (g m^{-2})	TOC content (kg)
7	32.5	11	145	Spring	131	1.25	19
15	40.5	14	355	Spring	98	3.10	36
25	50.5	18	692	Spring	138	0.07	96
75	100.5	35	7880	Spring	80	0.16	632
7	32.5	11	145	Autumn	76	1.25	11
15	40.5	14	355	Autumn	100	3.10	37
25	50.5	18	692	Autumn	77	0.07	53
75	100.5	35	7880	Autumn	49	0.16	387

c. TOC enrichment effect in the sediment

A TOC enrichment of the sediment within 25 m of the SPL was calculated as the product of the ellipse area with long radius 50.5m and short radius 18 m (excluding the SPL area) and the TOC content of the area between 25 and 75m from the SPL (80 and 49 g TOC m-2 in Spring and Autumn, respectively). This calculation is based on the assumption that the TOC content between 25 and 75m is representative of the sediment TOC content beyond the footprint of the faecal pellets. In this scenario, the TOC content in Spring amounts to 727 kg in the total ellipse area with long radius 100.5m, while in Autumn, it is 446 kg.

The TOC enrichment of the sediment within the footprint of the faecal pellets was therefore 53 kg (+7%) in Spring and 33kg (+8.7%) in Autumn.

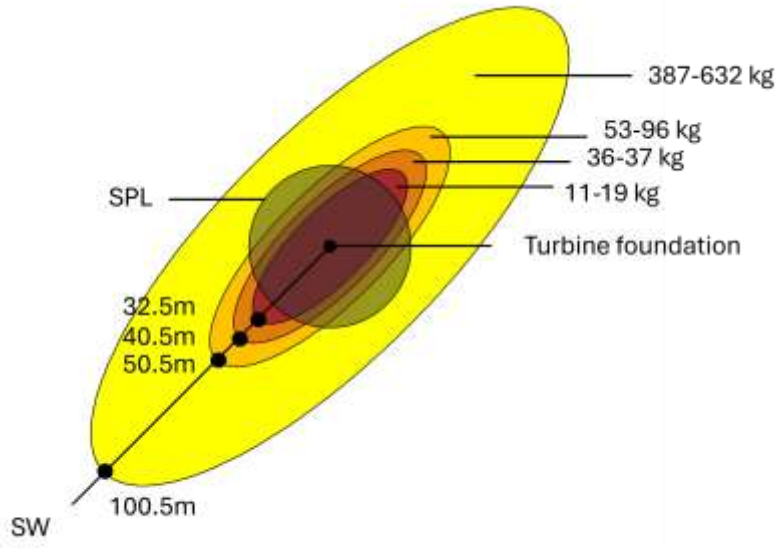

Figure 38. TOC content in the sediment in the footprint of the faecal pellet deposition area, an ellipse with long radii 32.5, 40.5, 50.5 and 100.5m, corresponding to the locations where sediments were sampled.

d. Potential sources of sediment organic enrichment within the footprint of the turbine foundation

Some back-of-the-envelope calculations might provide clues:

Faecal pellet input

From the results of the hydrodynamical model (4.1), we can conclude that only faecal pellets of *Metridium* would reach the seafloor in the considered ellipsoid area with long radius 100.5m (i.e. the sampled gradient). Faecal pellets of *Jassa* and *Mytilus* released by fouling fauna on a turbine foundation float far beyond this area (> 2 km) before they reach the sediment.

Based on the faecal pellet production rate of *Metridium* (1.56 * 10^{-2}mgC FP ind^{-1} h^{-1}), the density of Metridium (80 ind m^{-2}; whose FP have the highest chance of falling in the ellipse with 100.5m long radius; *Mytilus* and *Jassa* FP float much further) and a surface of the turbine over which the *Metridium* occur (radius 5m, lowest 6m of the turbine foundation), about 2 kg C per year should be released from the turbine in the form of FP. The hydrodynamical model shows that only 10% of these faecal pellets of *Metridium* reach the sediment in the considered ellipse around the turbine foundation from which they were released. This is 0.019 g Cm^{-2} per year over the ellipse with long radius 100.5m, assuming equal distribution on the sediment (11051 m² incl. SPL), or **0.05 mg C m^{-2} d^{-1}** within the considered ellipse.

Drop-off from fouling fauna on the turbine foundation

Dannheim et al. (2025) show that on average, 221 ± 825 gC m^{-2} turbine per year of dead fouling fauna biomass is released from the turbine. This corresponds to 0.6 g C m^{-2} turbine per day. Assuming a turbine foundation with radius 5m and height 30m (942 m²), 565 gC drops from the turbine foundation every day, or 208 kg C per year. Most of the dead biomass of *Mytilus* and probably *Metridium* will not

drift far, as mussel patches have been found at 37.5m from the turbine (~12m from the SPL) (Lefaible et al. 2023). *Jassa* biomass might drift further.

Even if we assume that all the dead fouling fauna biomass reaches the sediment within the considered ellipse, 208 kg C would come down from the turbine and arrive at the sediment over the course of one year. Spread over the ellipse (long radius 100.5m incl. SPL ~11051 m²), this corresponds to 18.8 g TOC m^{-2} year, or **0.05 gC m^2 d^{-1}.**

C deposition from phytodetritus

The C deposition from phytodetritus, strongest in spring, also contributes to the TOC stock in the sediment. Averaged over an entire year, this C deposition has been estimated in the BPNS outside of the OWF area, to range between **0.14 and 0.88 g C m^{-2} d^{-1}** (Joiris et al. 1982; Lancelot et al. 2005; Provoost et al. 2013).

Toward closing the carbon budget

In the sediment, we find about a **TOC stock of 49-138 g C m^{-2}** (in the ellipse with long radius 100.5m: 726 kg TOC in spring and 445 kg TOC in autumn, Table 11), of which **0.86-2.11 g C m^{-2} d^{-1} is mineralised** (De Borger et al. in prep.; Fig 39). An additional 12.6 mmol C/m²d or **0.15 g C m^{-2} d^{-1} is grazed** upon **by macrofauna** (De Borger et al. 2025). This means that after ~2 months, all the TOC in the sediment would be grazed away or mineralised. Therefore, there must be a steady input of organic carbon.

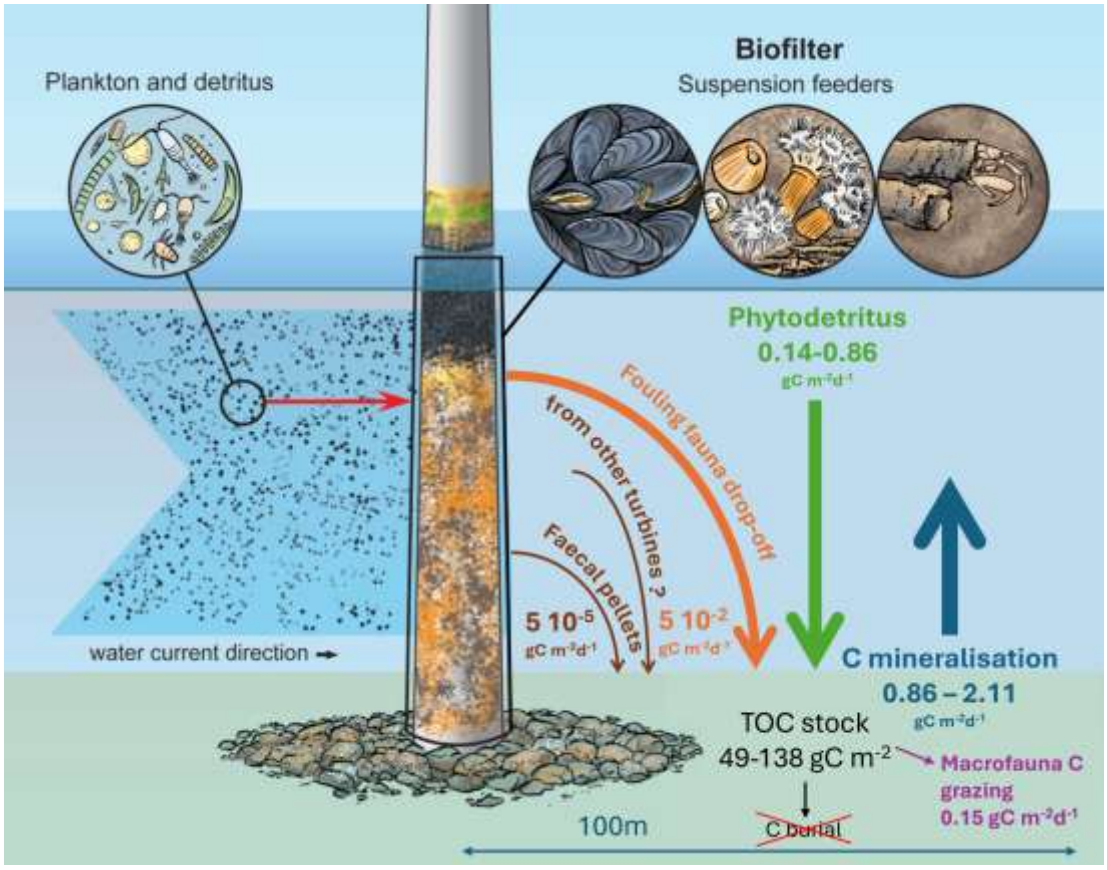

Figure 39. Preliminary Carbon budget for the sediment around an offshore wind turbine foundation

The TOC deposition from sinking phytodetritus cannot fully compensate for the C loss through mineralisation. The deficit ranges from - 0.02 to + 1.97 g C m^{-2} d^{-1} (subtracting the ranges on phytodetritus C input from those of the mineralisation rate). However, the TOC in the sediment encompasses the fresh and labile fraction that is quickly mineralised, and also an older, more refractory fraction, that is only slowly mineralised and can remain longer in the sediment.

The TOC biomass from phytodetritus is the largest input to the sediment, 3-18 times higher than that of the fouling fauna biomass drop off. The TOC biomass from the fouling fauna that comes down in the considered ellipse is on its turn 1000x higher than the TOC biomass from the FP of the fouling fauna.

However, there is still a high variability on the estimates in the local carbon budget around a turbine foundation:

- The upscaling from the sediment TOC measurements can be overestimated along the NW-SE axis (parallel to the sampled axis). Indeed the strongest organic enrichment has been found along the SW axis (Coates et al. 2014), but this difference is at most a factor 2.
- The estimates of fouling fauna biomass drop-off have a standard deviation of 4x the mean, even ranging to biomass gain on the turbine foundation. Biomass gain or loss for the turbine studied should be considered.
- The hydrodynamic modelling does not account for local eddies around the turbine foundation that could increase deposition rates of the faecal pellets, but also resuspend the faecal pellets again.
- The phytodetritus deposition can locally be higher in the wake of the turbine.
- Faecal pellets from Jassa and Mytilus released at upstream turbines can be deposited on the sediments around the considered turbine.
- The current-induced energy at the seabed has been shown to decrease from 170 N/m² down to 50 N/m² in the wake of each pile. The wake reaches 1000m along the main tidal axis (SW-NE). Advective flows in sediments around the turbine foundation are therefore potentially locally reduced because of this current reduction (Legrand et al. 2024). This would then explain why the TOC can stay in the sediment. The currents along the orthogonal axis (SE-NW) are increased up to 350m from the turbine, where advective flows could be stronger. It is unclear how these contrasting forces on advective currents are balanced in the field.

e. Recommendations

In summary, between spring and autumn, there can be a max. 8.7% increase in TOC stock (particulate organic carbon and macrobenthos) as opposed to background (> 75m from SPL) values. Note however, that this additional organic carbon is not permanently stored, so it is not to be considered long-term carbon sequestration. The sediments around the turbines remain permeable, and as such prone to resuspension of stored organic carbon and rapid organic carbon mineralization. In addition, the future decommissioning of the OWF sites will also mean significant removal of the organic carbon that was temporarily stored.

Recommendations on field work:

Sample more sediments adjacent to turbine foundations for TOC stock and mineralisation rate measurements, in longer gradients, different axes and around different foundation types, with and without SPL, to improve estimates of the representability of the above results for the entire OWF area.

Recommendations on data analysis:

Biomass gain or loss for the turbine studied should be considered, using the models from Dannheim et al. (2025).

Recommendations on modelling: the following elements should be represented in the hydrodynamical model:

- local eddies that enhance deposition of faecal pellets and resuspension of deposited organic matter
- local deposition patterns of phytodetritus in the wake of the turbine
- local deposition patterns of faecal pellets released at upstream turbine foundations

One enigma to solve is the contrast between the organic inputs from phytodetritus and fouling fauna biomass drop-off on the one hand, and the estimated organic carbon flux from the sediment trap. The sediment trap results indicate that 4-19 g C m^{-2} d^{-1} rain down on the sediment at ~100m from the turbine foundation (Table 11). This is 4-20 times higher than what we can find from potential sources (0.14 and 0.88 g C m^{-2} d^{-1} from phytodetritus + 0.05 gC m^{-2} d^{-1} from fouling fauna biomass drop off + 0.05 *10-3 g C m^{-2} d^{-1} from faecal pellets). We hypothesise that the sediment trap contains carbon originated from resuspended organic matter that had been accumulating on the seabed.

4.6 Organic matter processing in the sediment: food web research

a. Sediment characterisation

Sediments from all reference (REF) and offshore wind farm (OWF) replicates were similar across all measured characteristics (Table 12). They consisted of sandy, permeable sediments (permeability: REF 27.7 ± 3.36 × 10^{-12} m², OWF 28.2 ± 4.90 × 10^{-12} m²) with medium-coarse grain sizes ranging from 350 to 500 µm and relatively low organic carbon content (REF 0.045 ± 0.018 %, OWF 0.045 ± 0.014 %). The smallest grain size observed was 125 µm, indicating that no mud fraction (<63 µm) was present in either REF or OWF samples.

Table 12. Sediment characteristics of the sampled areas of the reference zone and offshore wind farm area, expressed as mean ± standard deviation. Calculations were made from 4 replicate box cores in each area. Porosity, TOC and median grain size were calculated using results from the upper 10cm of sediment collected at the specified locations. The fine sediment fraction includes all sediment < 250 µm.

		REF	OWF
Permeability	10^{-12} m^{-2}	27.7 ± 3.36	28.20 ± 4.90
Median grain size	µm	362 ± 14	379 ± 21
Fine sediment fraction (< 250 µm)	%	11 ± 2	11 ± 3
Porosity	$ml_{porewater}$/ $ml_{wet\ sediment}$	0.329 ± 0.067	0.391 ± 0.054
TOC	%	0.045 ± 0.018	0.045 ± 0.014
Chl a	µg/g	0.054 ± 0.021	0.062 ± 0.042
Chl a/CPE	-	0.705 ± 0.069	0.690 ± 0.088

b. Sediment community oxygen consumption (SCOC)

The two sediment types showed distinctly different responses to the addition of faecal pellets. The OWF sediment exhibited an immediate and steadily increasing reaction following pellet addition, whereas the reference sediment responded more slowly. On day 1, SCOC in the reference sediment was less than half that of the OWF sediment. However, it rose substantially over time—matching OWF levels by day 3 and surpassing them by day 5 (Fig. 40).

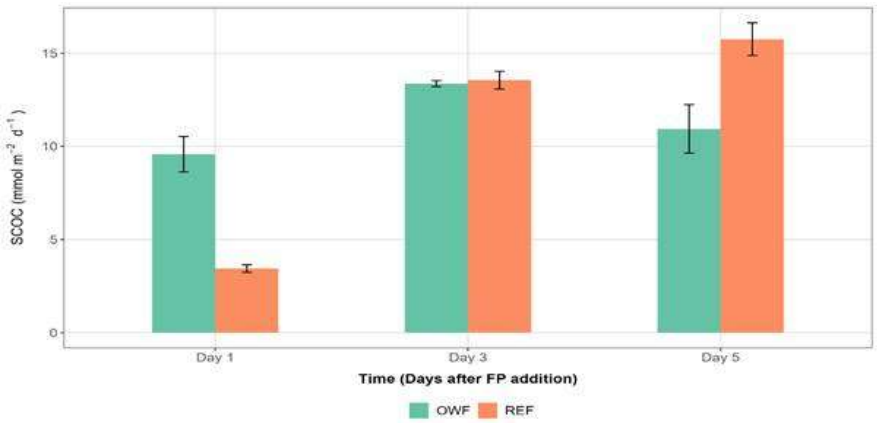

Figure 40. Sediment community oxygen consumption (SCOC; mmol m^{-2} d^{-1}) for the 3 times of closed-core incubation experiment after faecal pellets addition in the microcosms containing sediment from C-Power (OWF, green) and a reference zone (REF, orange).

c. Water column DIC

DIC dynamics in the overlying water reflect carbon release from sediments through respiration and organic matter mineralization, with minor contributions from other water column processes. Sediment-water exchange of FP-derived DIC was measured during three incubation experiments conducted one, three, and five days after M. edulis FP addition. Day-one REF results were excluded due to DIC trap malfunction.

From day one to three, mean FP-derived DIC in OWF cores showed slight changes, with two cores decreasing and two increasing (Figure 9, left). On day three, REF cores had higher mean DIC fluxes than OWF cores (REF: 3.79 ± 1.03 mmol m^{-2} d^{-1}; OWF: 2.70 ± 0.81 mmol m^{-2} d^{-1}). Between day three and five, FP DIC increased similarly in all OWF cores; in REF cores, three increased while one declined. By day five, mean FP-derived DIC fluxes were comparable between REF and OWF (≈3.70 mmol m^{-2} d^{-1}, Figure 42, right).

Estimated over seven days, total FP mineralization to DIC was 26.51 ± 18.32 mmol m^{-2} in REF and 21.91 ± 15.11 mmol m^{-2} in OWF cores, with no significant difference between areas (Wilcoxon signed-rank test, $p > 0.05$). (Fig. 41)

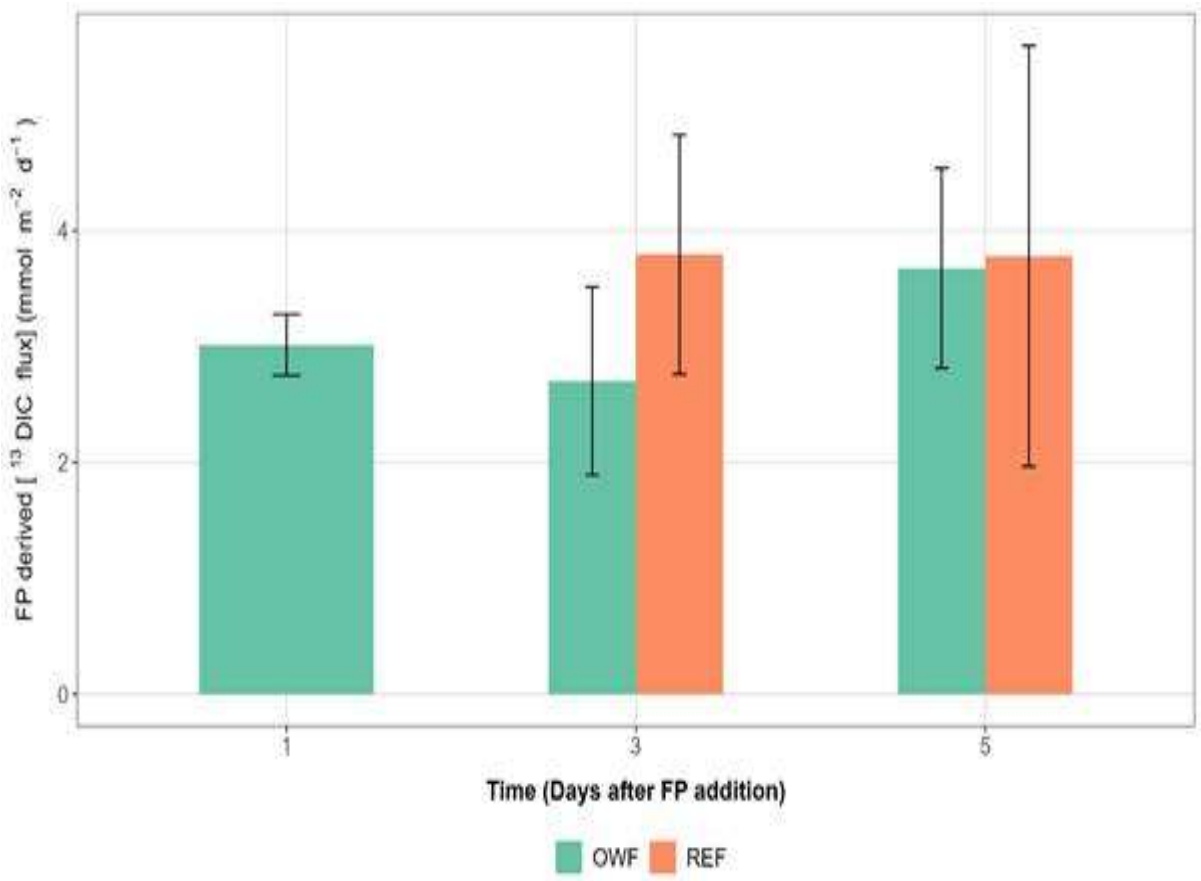

Figure 41. Flux of FP-derived ^{13}C-DIC (mmol m^{-2} d^{-1}) in overlying water of offshore wind farm (OWF, green) and reference (REF, orange) sediment cores over five days following FP addition. Error bars represent standard deviation across replicates.

d. Porewater DIC

Pore water DIC concentrations were measured at 1-cm intervals for each sediment core. FP-derived DIC concentrations differed significantly between OWF and REF cores (Wilcoxon signed-rank test, $p < 0.05$). In the upper sediment layers, OWF cores exhibited higher concentrations than REF cores, with averages of 352.76 µmol m^{-2} and 176.79 µmol m^{-2} in the first centimetre, respectively (Figure 42, left). At greater depths, concentrations in both core types converged, reaching 227.75 µmol m^{-2} in REF and 188.81 µmol m^{-2} in OWF cores at 6–7 cm depth. Three of the four REF cores showed very similar DIC concentration profiles with depth, while the fourth core had slightly elevated values. In contrast, OWF cores displayed greater variability among replicates.

Summing the contributions across all sediment layers revealed that the total amount of FP-derived carbon transferred to pore water was higher in OWF cores (2151.98 µmol m^{-2}) than in REF cores (1442.26 µmol m^{-2}). (Fig. 42)

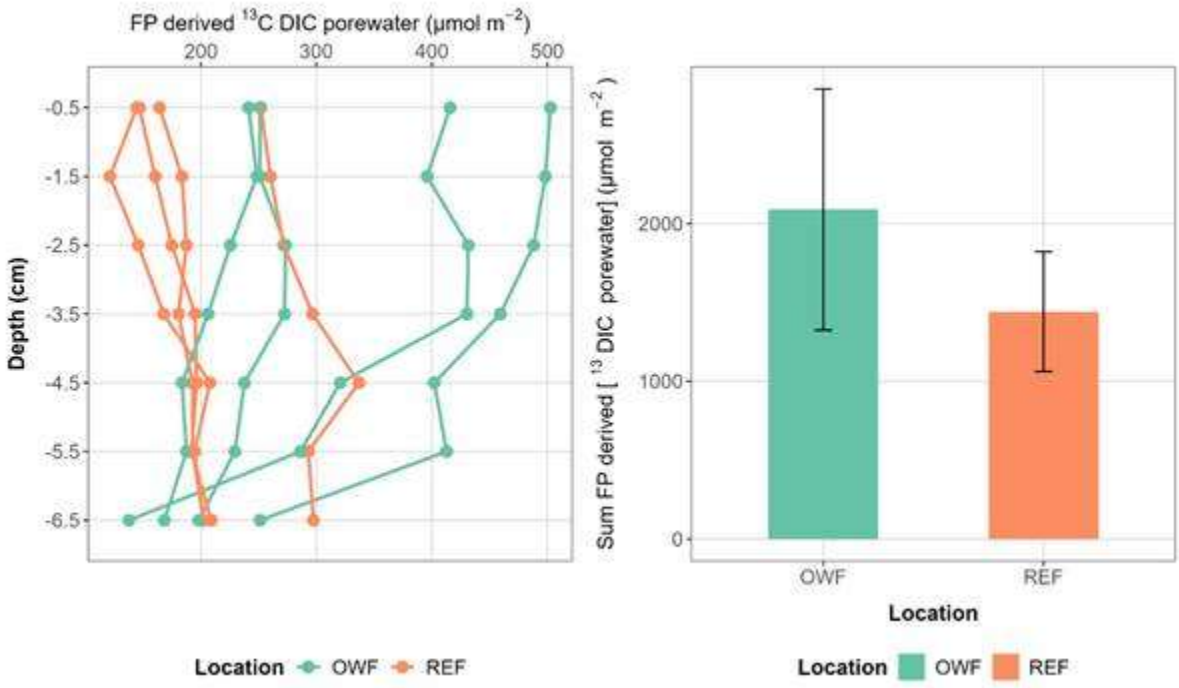

Figure 42. Dissolved inorganic carbon (DIC) concentrations in pore water from M. edulis FPs in reference (REF) and offshore wind farm (OWF) sediments. Left: values per individual core; right: mean values per location with error bars representing standard deviation

e. TOC

Analysis of total organic carbon (TOC) showed that the sediment contained a high proportion of FP-derived carbon, particularly within the upper centimetre of the cores (REF: 41.35 ± 15.68 mmol FP C m^{-2}; OWF: 65.36 ± 41.87 mmol FP C m^{-2}). Below this layer, FP carbon levels dropped sharply, reaching much lower concentrations between 1 and 2 cm depth (REF: 7.38 ± 2.94 mmol FP C m^{-2}; OWF: 5.83 ± 2.67 mmol FP C m^{-2}). This pattern of surface enrichment followed by rapid decline was evident in both REF and OWF cores (Figure 43, left). However, the average FP carbon content in the upper centimetre of OWF cores was approximately 1.5 times higher than in REF cores (Figure 43 right). Below 1 cm, FP-derived TOC values were similarly low across both core types, and in the deepest layers (6–10 cm) they approached zero (REF: 0.12 ± 0.97 mmol FP C m^{-2}; OWF: –0.93 ± 1.93 mmol FP C m^{-2}).

Inspection of individual cores (Figure 43) revealed that two OWF cores closely resembled the REF cores, whereas the remaining two OWF cores (OWF 1 and OWF 4) showed substantially elevated FP-derived TOC in the upper centimetre. This variability resulted in the large standard deviation and corresponding error bars observed for the OWF surface layer. In contrast, REF cores showed much less variation. At depths greater than 1 cm, TOC values across all cores were consistent, leading to narrow error margins.

The difference in FP-derived TOC between REF and OWF cores was not statistically significant across the full depth profile (Wilcoxon signed-rank test, $p > 0.05$) nor within the upper centimetre (Wilcoxon signed-rank test, p 0> 0.05).

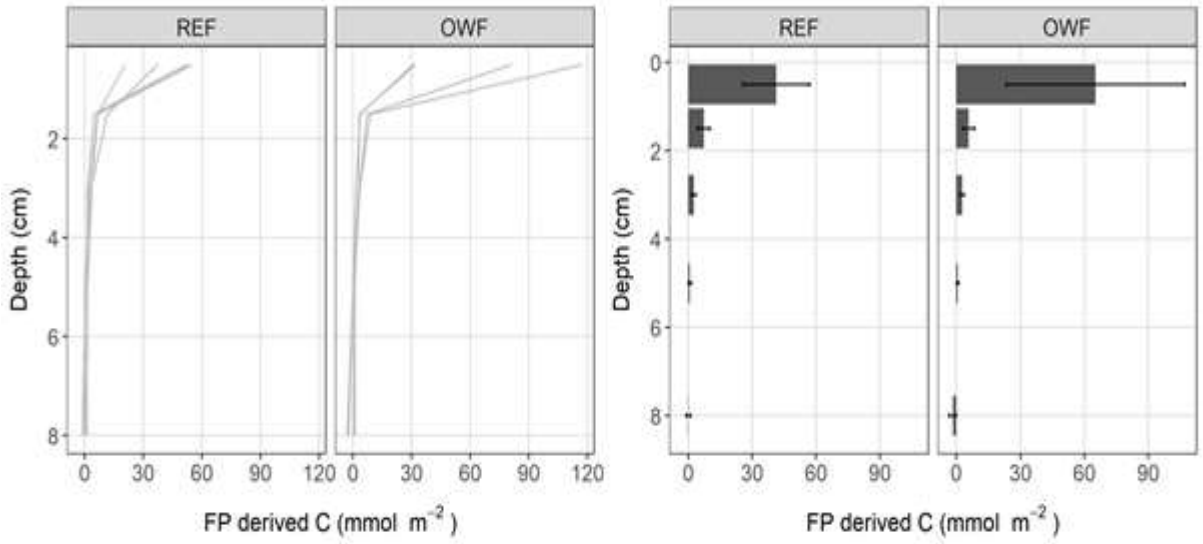

Figure 43. Faecal pellet derived total organic carbon (TOC) values across depth layers of sediment from the reference area and the offshore wind farm area per sediment core (left) and as mean with error bars representing standard deviation (right). This carbon pool represents the amount of faecal pellet that was left unprocessed throughout the experiment. Depth is indicated as the mean depth of the pooled layers (e.g. 6-10cm sample can be found at 8cm on the graph).

f. Fauna assimilation

The average assimilation of FP-derived carbon by meiofauna in reference (REF) samples ranged from 0.0016 to 0.0185 mmol m^{-2}, while in offshore wind farm (OWF) samples it ranged from 0.0039 to 0.1286 mmol m^{-2} (Fig. 44). For copepods, no significant difference in assimilation was observed between the two sites (two-sample t-test, $p > 0.05$). In contrast, nematodes showed a significant increase in FP carbon assimilation in OWF sediments (Wilcoxon signed-rank test, $p < 0.05$), with mean values of 0.0146 ± 0.0028 mmol m^{-2} in REF and 0.0667 ± 0.0488 mmol m^{-2} in OWF cores seven days after FP addition. Assimilation among OWF replicates varied from 0.0222 to 0.1286 mmol m^{-2}.

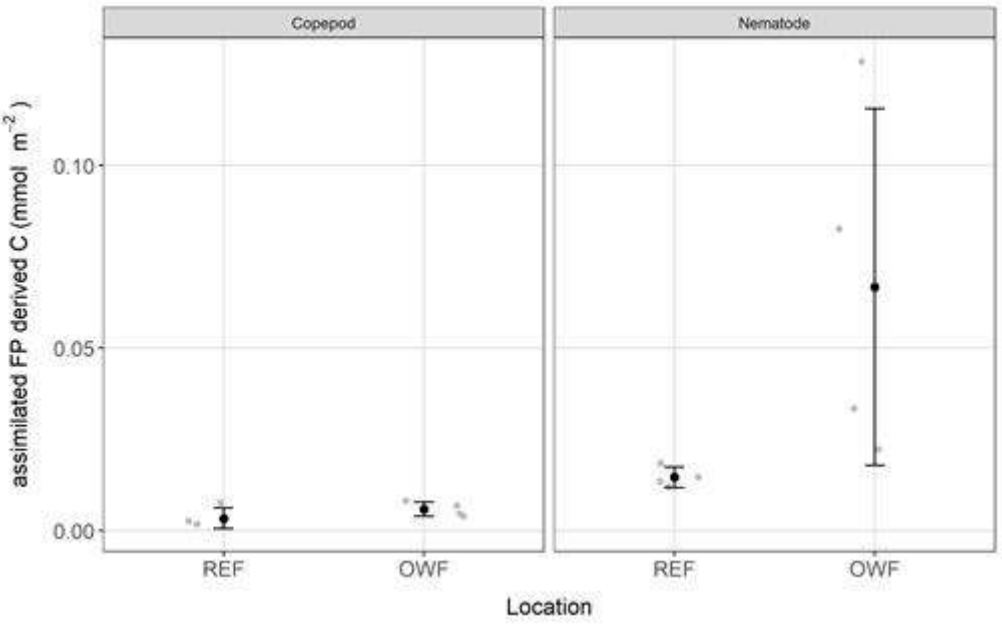

Figure 44. Assimilation of faecal pellet (FP) carbon by meiofauna (Copepoda and Nematoda) during the incubation experiment on RV Belgica. FP carbon assimilation did not differ significantly for Copepoda between

REF and OWF cores (two-sample t-test, $p > 0.05$). Nematodes, however, showed significantly higher assimilation in OWF cores compared to REF cores (Wilcoxon signed-rank test, $p < 0.05$), with means of 0.015 ± 0.003 mmol m^{-2} in REF and 0.067 ± 0.049 mmol m^{-2} in OWF.

For macrofauna, mean FP carbon assimilation did not differ significantly between REF and OWF cores (two-sample t-test, $p > 0.05$), with 4.87 ± 10.32 µmol m^{-2} in REF and 19.06 ± 39.04 µmol m^{-2} in OWF cores. Most macrofaunal taxa showed no significant differences between sites, except for Mysida, which assimilated significantly more FP carbon in OWF cores (3.62 ± 0.83 µmol m^{-2}) compared to REF (0.46 ± 0.78 µmol m^{-2}, two-sample t-test, $p < 0.05$) (Figure 45.). Cumacea results were limited to two OWF cores with no REF comparison, so Amphipoda data were used instead. Notably, Amphipoda exhibited the highest FP carbon assimilation among macrofauna in OWF replicate 1 (16.64 µmol m^{-2}), nearly four times higher than the other OWF replicate.

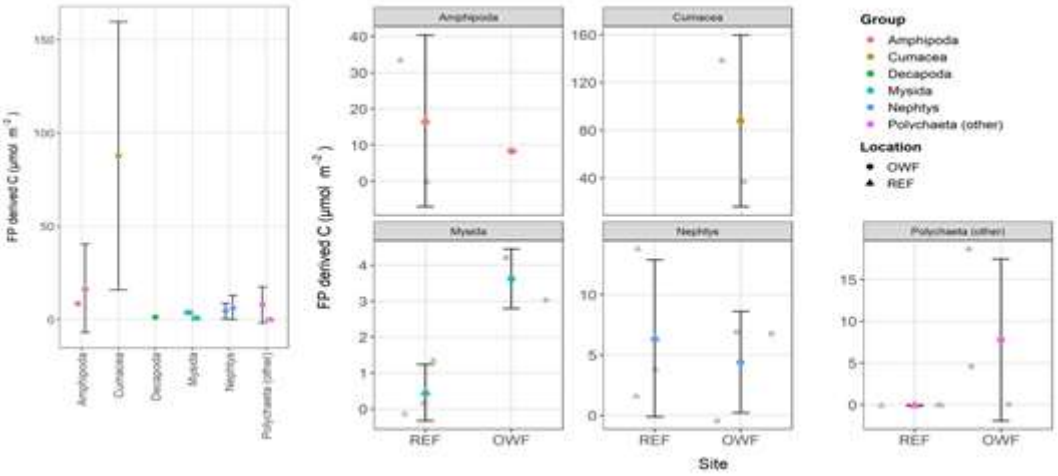

Figure 45. Assimilation of faecal pellet–derived carbon by macrofauna (mmol m^{-2}) in reference (REF) and offshore wind farm (OWF) sediments. Gray points show individual measurements, while colored points represent means ± standard deviation

g. POC and bacteria assimilation

Data on particulate organic carbon (POC) and bacterial assimilation are still being processed and have not yet been integrated into the carbon budget. Once included, these pools may provide a more complete understanding of faecal pellet–derived carbon flow and retention in REF and OWF sediments.

h. Preliminary carbon budget – food web

At the end of the seven-day experiment, 13C-labelled faecal pellets (FP) were added to four REF and four OWF sediment cores, and various carbon pools were analysed: sediment TOC (representing unprocessed FP), meiofauna, macrofauna, DIC in overlying water, and DIC in pore water. Overall, 56.6% (81.94 mmol m^{-2}) of FP carbon was traced in REF cores and 69.4% (100.47 mmol m^{-2}) in OWF cores. In REF cores, ~36.1% of FP carbon remained in the sediment, mainly in the top 1 cm, whereas in OWF cores this was ~50.7%. Most processed FP carbon was mineralized through respiration, accounting for 89.4% of processed FP in REF cores and 81.5% in OWF cores. Pore water DIC mineralization contributed 10.4% in REF and 18.0% in OWF, while faunal assimilation was minimal (<1%), with meiofauna and macrofauna assimilating similar small amounts per site. Overall, respiration dominated FP processing, while OWF cores showed higher retention of FP in sediment,

pore water, and faunal pools, reflecting slower degradation. FP-derived DIC in pore water was higher in OWF cores, especially in surface layers, but converged with REF cores at depth, suggesting less effective diffusion in OWF sediments. TOC measurements showed that FP carbon was concentrated in the top 1 cm, with a steep decline below, indicating limited vertical mixing. Bioturbation, a potential mixing mechanism, was not observed, likely due to small core size, laboratory conditions, and localized sampling. The higher amount of residual FP in OWF cores aligns with lower respiration rates, suggesting that OWF sediments retain more organic carbon. This may result from slower degradation by benthic communities or microbial activity, despite similar sediment characteristics between REF and OWF sites. These results support the hypothesis that OWF sediments act as localized carbon sinks, with a net higher retention of FP-derived organic carbon (Figure 46) .

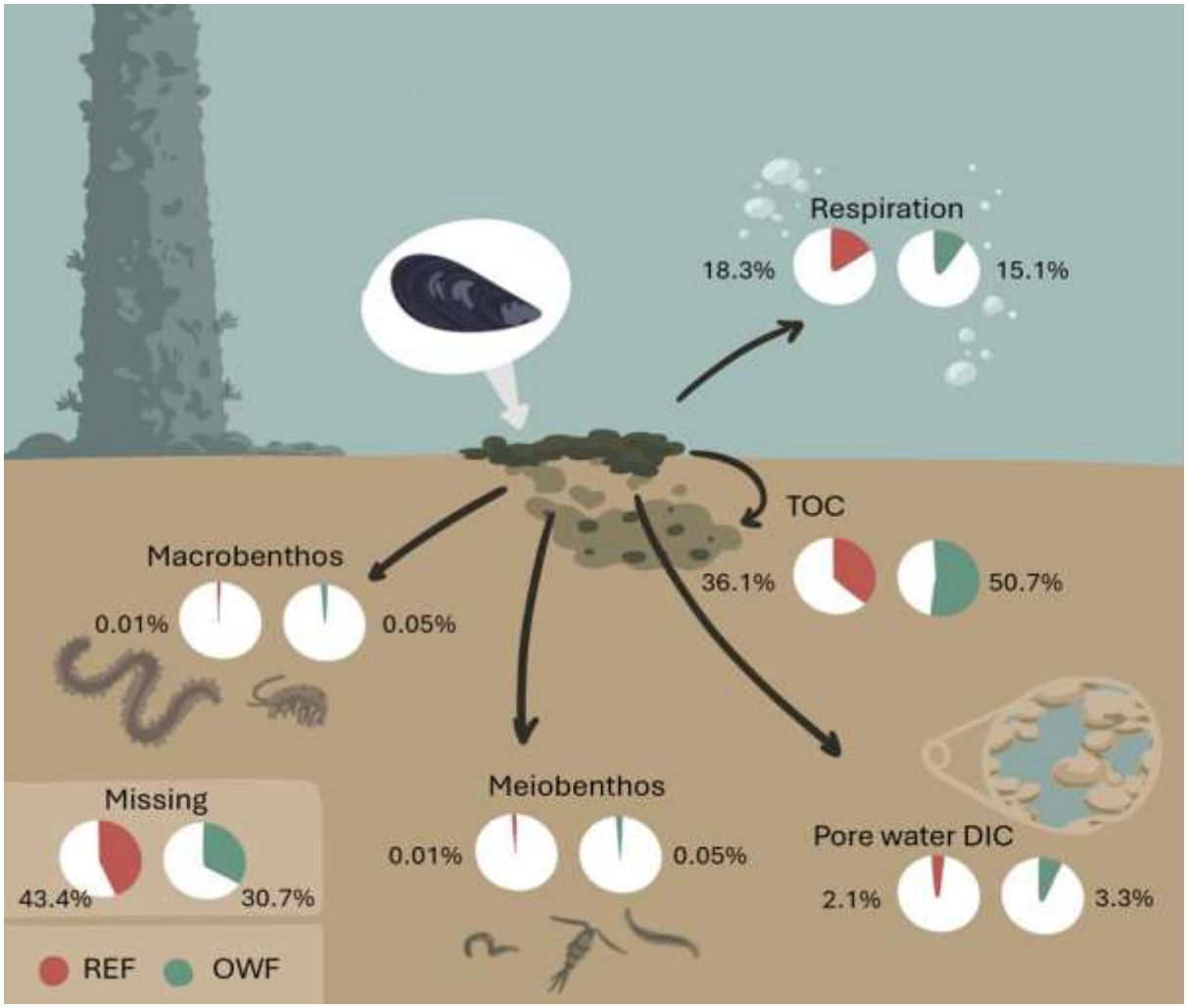

Figure 46. Summary of the carbon budget of blue mussel (M. edulis) faecal pellet (FP) carbon in REF (red) and OWF (green) sediments with similar properties. Using 13C-labelled FP over seven days, key differences were observed: higher respiration in REF (red), greater incorporation into sediment pools in OWF (green), and more unprocessed FP in surface sediment in OWF (green). The carbon budget was more fully accounted for in OWF sediments. © Iona Birnie

i. Recommendations

Based on the findings of this study, several recommendations can be made for future research and the management of offshore wind farm (OWF) environments. **Extending the duration of pulse-chase experiments** would provide a more comprehensive understanding of the long-term fate of mussel faecal pellet (FP) carbon in sediments. **Sampling over longer periods** and at multiple time points would

allow the tracking of degradation, assimilation, and burial processes beyond the seven-day timeframe used here, offering insight into the persistence of OWF sediments as localized carbon sinks.
Increasing the number of sediment cores and expanding spatial coverage within and around OWFs would help account for the high variability observed in FP processing, particularly due to the heterogeneity of sediment enrichment, biofouling drop-off, and faunal distribution. Sampling across different distances from turbines and considering various foundation types could clarify how structural and environmental factors influence sediment carbon cycling. Experimental design improvements are also recommended. Ensuring airtight DIC traps and more stable laboratory conditions would prevent potential artifacts in FP distribution and DIC measurements. Using larger sediment cores or implementing in situ experiments could better replicate natural bioturbation and sediment-water exchange processes, which were limited under laboratory conditions.
Future studies should also incorporate **additional carbon pools, including dissolved organic carbon in the pore water, and in the water column**. conducting depth-resolved analyses of microbial communities likely play a major role in FP processing, particularly in reference sediments where higher respiration rates were observed and including them would allow for a more complete closure of the carbon budget. Similarly, meiofauna and macrofauna would improve understanding of FP assimilation patterns, as the vertical distribution of organisms within the sediment appears to influence their access to and uptake of organic matter. Further research into the structure and feeding strategies of benthic communities is needed to explain variability in FP assimilation among taxa. Studying the responses of meiofauna and macrofauna to OWF-induced environmental changes could clarify whether trophic shifts toward detritivory or omnivory enhance sediment carbon retention. Monitoring sediment characteristics, such as grain size, permeability, and organic matter content over time, would also help link physical sediment properties with carbon processing and burial.
Finally, these findings suggest that OWF sediments may act as localized carbon sinks, especially in areas with abundant filter-feeding fouling fauna. Recognizing this role in carbon cycling could inform environmental impact assessments and carbon management strategies for offshore wind farms, highlighting the potential of OWFs not only as renewable energy sources but also as contributors to carbon sequestration in coastal ecosystems.

4.7 Organic matter processing in the sediment: mineralisation

a. Sediment properties

Across all sampling periods and distances from the turbine, sediments were characterized by medium to coarse sands, with median grain size (MGS) values ranging between 292 and 435 µm (Table 13). Although variability occurred between specific season–distance combinations, no consistent trend in MGS was observed with distance from the scour protection layer (SPL). Permeability values reflected these grain-size patterns, ranging from 2.09×10^{-12} to 1.31×10^{-11} m², consistent with the sediments' permeable nature.

Surface total organic carbon (TOC) contents were low overall, varying from 0.03% to 0.08% of sediment dry weight, but displayed clear seasonal differences. TOC was highest in spring and summer (up to 0.08 ± 0.02%), and declined markedly in autumn (minimum 0.03 ± 0.01%). No systematic pattern with distance was apparent in surface sediments, but in the subsurface layers (2–12 cm), TOC tended to decrease with increasing distance from the turbine, particularly in spring and summer.

Photosynthetic pigment concentrations (chlorophyll a and its degradation products) also showed distinct seasonal dynamics (Table 13). Surface chlorophyll *a* values were greatest in spring, ranging from 0.64 to 1.26 µg g^{-1}, indicating recent deposition of fresh organic material. Concentrations decreased toward autumn (0.17–0.34 µg g^{-1}). Similar patterns were observed for pheophorbide and pheophytin, which were elevated in spring and lower in autumn, though their spatial variability between distances was more pronounced. In general, pigment concentrations were highest close to the turbine (7–15 m) and lowest at 75 m, particularly during spring and summer, suggesting enhanced organic matter input or retention near the SPL.

Table 13. Measured surface (average top 2 cm ± SD) values for median grain size (MGS, µm), permeability (m^2), total organic carbon (TOC, %), chlorophyll a (Chl a, µg g^{-1}), pheophorbide (µg g^{-1}), and pheophytin (µg g^{-1}).

Season	Distance (*m*)	MGS (*µm*)	Permeability	TOC (%)	Chl a (*µg g^{-1}*)	Pheophorbide (*µg g^{-1}*)	Pheophytin (*µg g^{-1}*)
spring	7	364 ± 70	5.77 10^{-12}	0.07 ± 0.04	0.64 ± 0.35	0.05 ± 0.04	0.12 ± 0.14
spring	15	339 ± 32	4.16 10^{-12}	0.05 ± 0.01	0.99 ± 1.24	0.04 ± 0.04	0.14 ± 0.2
spring	25	292 ± 7	2.09 10^{-12}	0.08 ± 0.02	1.26 ± 0.75	0.08 ± 0.05	0.11 ± 0.08
spring	75	364 ± 13	5.77 10^{-12}	0.05 ± 0.01	0.2 ± 0.06	0.01 ± 0	0.01 ± 0
summer	7	364 ± 30	5.77 10^{-12}	0.05 ± 0.01	0.3 ± 0.11	0.03 ± 0.02	0.06 ± 0.02
summer	15	384 ± 23	7.39 10^{-12}	0.05 ± 0.01	0.16 ± 0.05	0.04 ± 0.02	0.04 ± 0.02
summer	25	372 ± 35	6.38 10^{-12}	0.05 ± 0.01	0.22 ± 0.17	0.05 ± 0.05	0.07 ± 0.07
autumn	7	354 ± 15	5.08 10^{-12}	0.04 ± 0.01	0.2 ± 0.08	0.02 ± 0.02	0.01 ± 0
autumn	15	392 ± 35	8.13 10^{-12}	0.05 ± 0.01	0.34 ± 0.09	0.02 ± 0.01	0.02 ± 0.01
autumn	25	435 ± 56	1.31 10^{-11}	0.04 ± 0.01	0.22 ± 0.15	0.01 ± 0.01	0.01 ± 0.01
autumn	75	355 ± 16	5.14 10^{-12}	0.03 ± 0.01	0.17 ± 0.1	0.01 ± 0	0.01 ± 0

b. Porewater nutrients

Porewater nutrient distributions (Figure 47) exhibited pronounced seasonal and spatial patterns. In spring, concentrations of ammonia (NH_3), nitrite (NO_2^-), and phosphate (PO_4^{3-}) were highest in sediments closest to the turbine (7 m), decreasing progressively with distance. Conversely, nitrate (NO_3^-) showed an opposite pattern — increasing with distance from the SPL, implying more oxidized conditions and/or decreasing organic matter loads further away from the turbine.

In summer, ammonia and phosphate remained elevated at 7 m but the gradients with distance were less distinct than in spring, indicating a more uniform distribution of organic matter loads and reactivity across sites. By autumn, nutrient profiles again differentiated with distance: nitrate concentrations increased away from the SPL, while phosphate declined. Ammonium concentrations

remained elevated across all distances, likely reflecting accumulated mineralization products from the preceding productive season.

These patterns collectively suggest that organic matter mineralization rates were greatest near the turbine, with strong coupling between carbon degradation and nutrient regeneration processes.

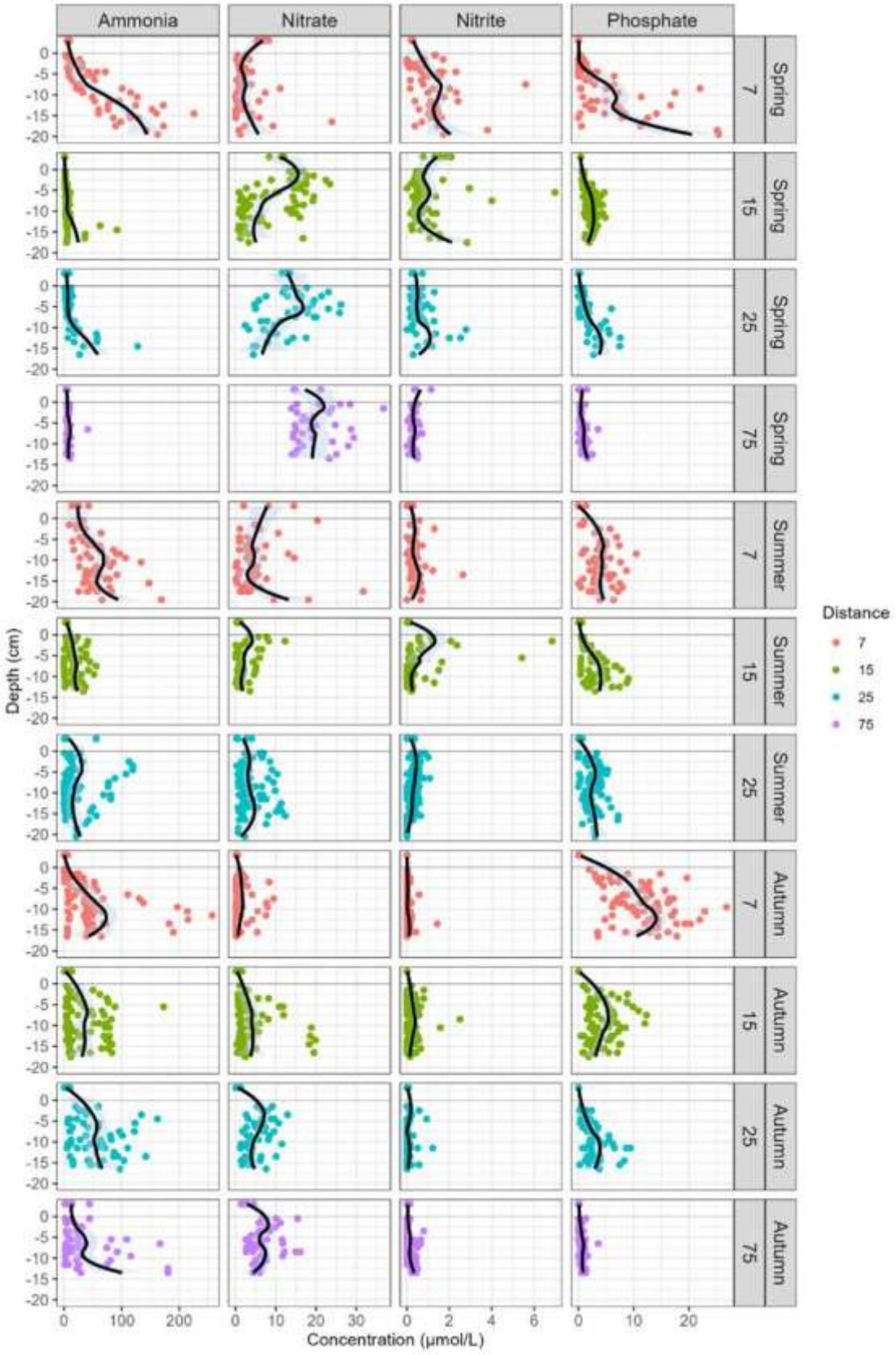

Figure 47. Smoothed (black lines) average porewater nutrient profiles for ammonia (NH_3), nitrate (NO_3^-), nitrite (NO_2^-), and phosphate (PO_4^{3-}) (columns) for the different season – distance combination (rows). Individual values shown by dots.

c. Modelled mineralization rates

Model simulations revealed marked seasonal and spatial variation in total carbon mineralization and the relative contribution of different mineralization pathways (Fig. 48). Across all seasons, total mineralization rates were highest closest to the turbine (7 m) and declined with distance, supporting field observations of enhanced organic enrichment near the SPL. In spring, total mineralization reached 176 ± 8 mmol C m^{-2} d^{-1} at 7 m, compared to 52–61 mmol C m^{-2} d^{-1} further away. Similar but slightly lower magnitudes were observed in summer (up to 146 ± 9 mmol C m^{-2} d^{-1} near the turbine) and autumn (approximately 138 ± 12 mmol C m^{-2} d^{-1}).

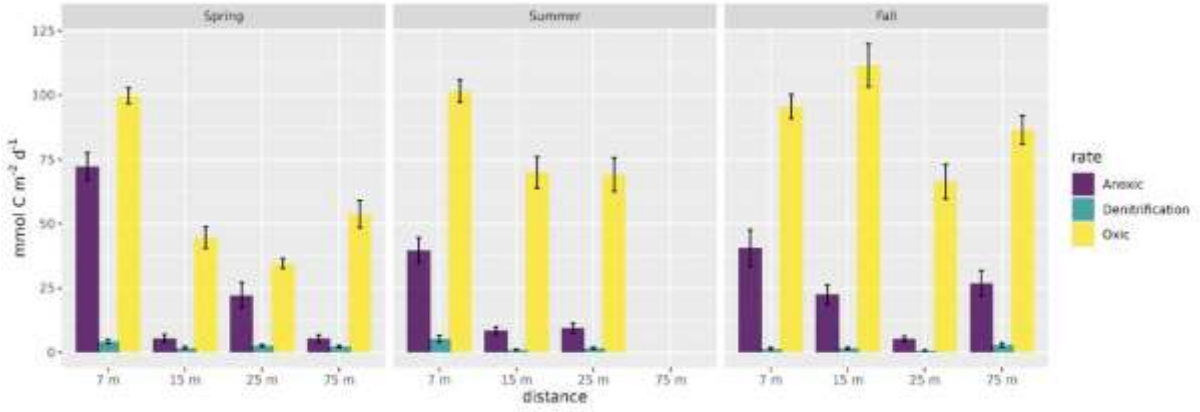

Figure 48. Carbon mineralization process rates (in mmol C m^{-2} d^{-1}, y-axis), grouped per season (panels) – distance (x-axis) from scour protection layer combination. Flags show standard deviation based on 2000 input parameter variations.

The dominant mineralization pathway throughout the study was oxic respiration, accounting for 59–92% of total mineralization, reflecting the efficient advective supply of oxygen within permeable sands. Anoxic mineralization contributed 7–41%, increasing in relative importance where permeability was lower or organic loads higher (particularly near the turbine). Denitrification represented a minor fraction of total carbon oxidation, typically 1–4.5%, but followed the same spatial pattern as anoxic mineralization, peaking closer to the turbine where organic matter availability and oxygen demand were highest.

The modelled oxygen and nutrient fluxes between sediment and overlying water followed these patterns. Sites nearest the turbine showed the highest O_2 uptake rates (up to 115 mmol O_2 m^{-2} d^{-1}) and ammonium effluxes, consistent with intensified remineralization of freshly deposited material. At greater distances, both oxygen consumption and nutrient release declined substantially.

Statistical analyses supported these spatial and biogeochemical trends. Total mineralization and anoxic mineralization rates decreased significantly with distance from the turbine, following power-law relationships (R^2 = 0.43 and 0.59, $p < 0.05$), confirming that mineralization activity was most intense closest to the turbine. The proportion of oxic mineralization showed a negative relationship with TOC content (R^2 = 0.22, p = 0.084), whereas anoxic mineralization increased significantly with TOC (R^2 = 0.30, p = 0.041**), reflecting the shift toward more reduced mineralization pathways in organic-rich sediments. Relationships with grain size followed the expected direction: oxic mineralization increased with coarser sediments, while the percentages of anoxic mineralization and denitrification declined (R^2 = 0.27–0.42, $p < 0.05$). Similarly, chlorophyll a and pheophorbide contents correlated with mineralization patterns: oxic mineralization was higher in sediments with low pigment

concentrations, whereas both anoxic and denitrifying pathways were enhanced at higher pigment levels, indicating a link between fresh organic input and oxygen demand.

d. Recommendations

The strong spatial gradients observed in sediment biogeochemistry highlight once more **that turbine induced effects are highly localized**, displaying high spatial variability and seasonality within a single wind farm. **Treating sediments at the wind farm scale as spatially uniform risks overlooking significant hotspots of mineralization and nutrient cycling that occur immediately adjacent to turbine structures**. Environmental monitoring and modelling should therefore be designed at a sufficiently fine spatial resolution to capture these near-field changes. Incorporating this small-scale heterogeneity into assessments will improve the accuracy of environmental impact predictions and better inform seabed management strategies around offshore wind infrastructure.

4.8 Spatial upscaling; field-based measurements

a. Water column structure

Vertical profiles of potential density revealed a predominantly well-mixed water column across all sampling sites, with only weak stratification events (Fig. 49). Midday to afternoon casts within the OWF (Simon Stevin) showed the strongest, though transient, density gradients caused by the intrusion of colder, more saline water at depth. Downstream of the OWF (Pelagia), temporary surface stratification appeared in early morning and late evening, driven by the formation of a warm, low-salinity surface lens. In all areas, daytime warming was quickly eroded by mixing, as supported by Brunt–Väisälä frequencies ($N^2 < 5 \times 10^{-4}\ s^{-2}$). These observations confirm that vertical structure during the study period was highly dynamic but overall weak, making it difficult to discern OWF-related effects on stratifications (if there are any).

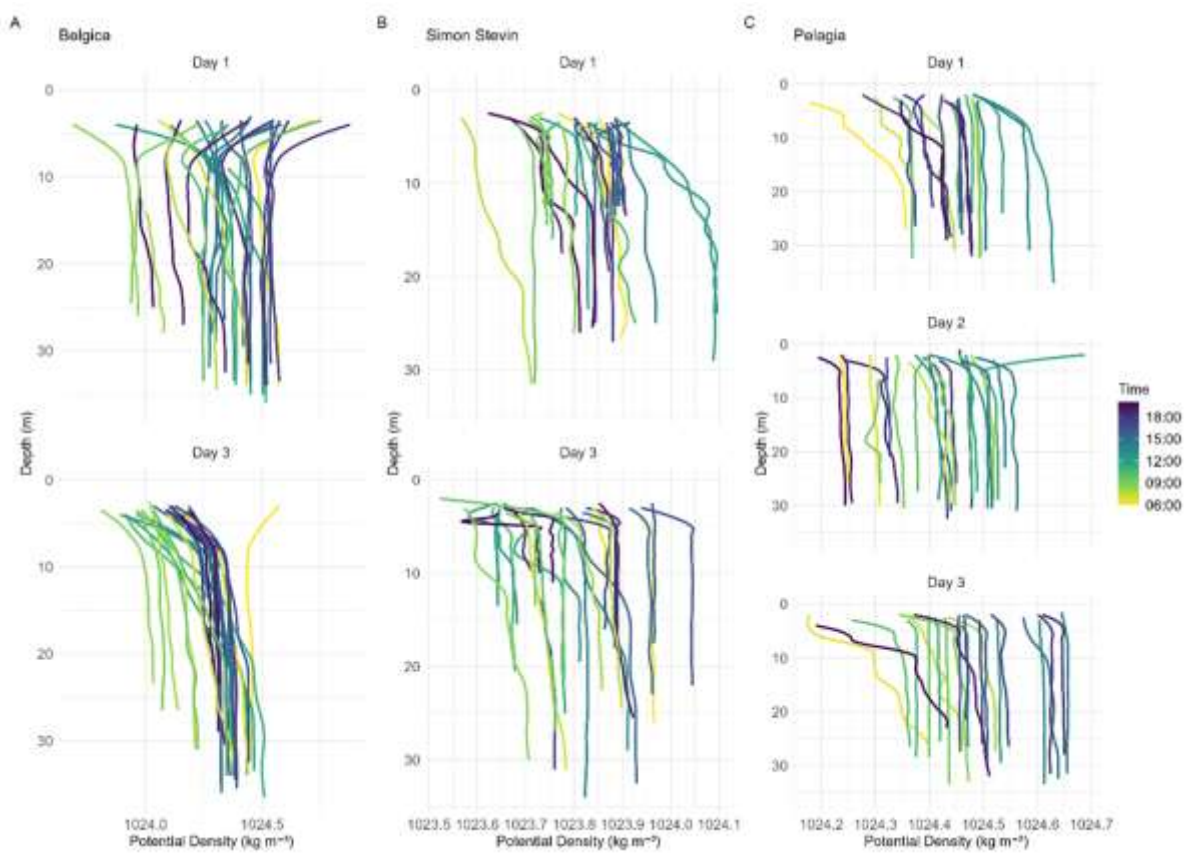

Figure 49. Potential density (ρ_0, kg m^{-3}, x-axis) with depth (m, y-axis) derived from CTD casts. Columns A-C show casts for each research vessels, and casts from different days are shown per row. Casts are coloured depending on the time of day they were collected (see colour legend).

b. Suspended particulate matter (SPM)

SPM concentrations differed significantly between sampling locations (Fig. 50, ANOVA, $p < 0.001$). The highest values occurred within the OWF (9.3 ± 5.3 mg L^{-1}), intermediate concentrations on its upstream border (5.5 ± 2.3 mg L^{-1}), and the lowest downstream (2.9 ± 1.1 mg L^{-1}). Surface samples contained slightly higher concentrations than bottom waters. These differences were captured well by the mixed-effects model ($R^2_{\text{fixed effects}} = 0.36$), confirming that spatial location was the dominant driver of SPM variability.

The elevated SPM within the OWF possible reflects enhanced local turbulence and sediment resuspension near turbine foundations, consistent with the high energy of the shallow, tidally dynamic setting. However, strong regional gradients particularly between the nearshore Scheldt-influenced waters and clearer offshore areas appear to dominate the overall pattern. The spatial contrast between south, within, and north of the OWF thus represents the superposition of coastal sediment inputs, tidal transport, and minor local mixing effects.

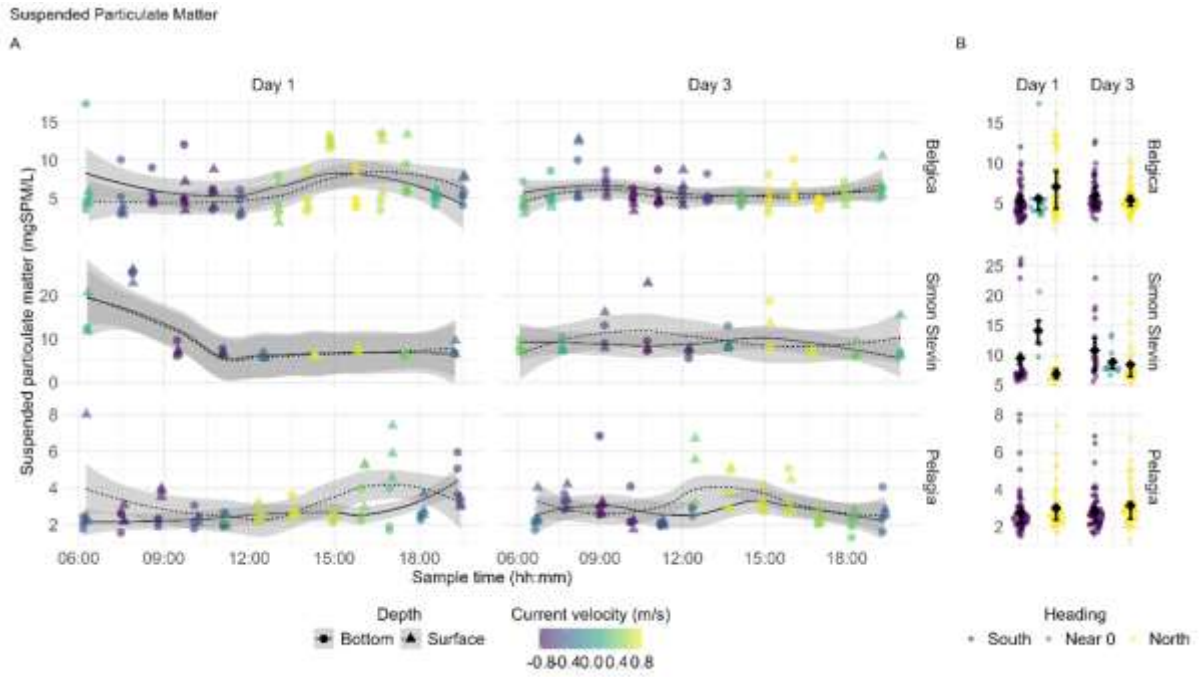

Figure 50. Suspended particulate matter (SPM, mgSPM L^{-1}) on the different sampling days and research vessels. (A) All measured concentrations for bottom (circles) and surface (triangles) samples, per day and per research vessel, coloured depending on the current velocity during sampling. Lines and grey shaded area represent a loess smoother to indicate trends in the data. (B) Distribution of SPM concentrations per day and per research vessel, grouped by the current direction while sampling in northward (yellow), near 0 (green, -0.2 – 0.2 m s^{-1}), and southward (purple) flowing currents. Black lines in point cloud indicate 0.25 to 0.75 quantile, with the mean indicated as a black diamond.

c. Chlorophyll *a* distribution

Chlorophyll *a* concentrations also differed significantly between locations, and between depth layers (Fig. 51). Mean values were highest upstream of the OWF (4.7 ± 1 µg L^{-1}), slightly lower within it (4.6 ± 1.6 µg L^{-1}), and lowest downstream (1.8 ± 0.4 µg L^{-1}). Surface waters generally contained more chlorophyll than bottom waters (mean difference ≈ 0.4 µg L^{-1}). Chlorophyll *a* declined with increasing mean current velocity but showed spatially varying relationships with current direction: concentrations rose with northward flow within the OWF but declined during southward phases. The mixed model ($R^2_{\text{fixed effects}}$ = 0.72) indicated that current strength and orientation explained most of the observed variability.

The chlorophyll patterns largely reflect the interaction of hydrodynamics and regional productivity gradients. The upstream transect, influenced by the nutrient-rich Scheldt plume, supported the highest phytoplankton biomass, while the OWF area displayed similar concentrations but also a stronger dependence on current direction, consistent with alternating advection of plume and offshore waters. The lowest values north of the OWF correspond to clearer, more oligotrophic conditions (also reflected in the measured nutrient concentrations).

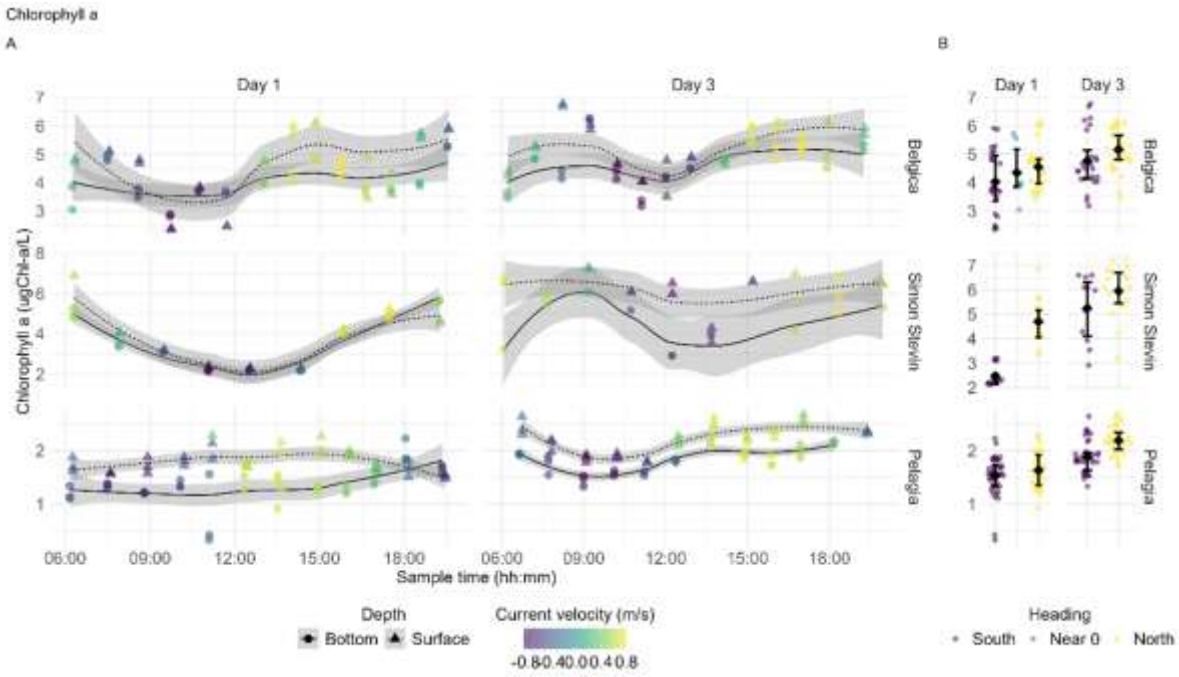

Figure 51. Chlorophyll a (Chl a, µgChl a L^{-1}) on the different sampling days and research vessels. (A) All measured concentrations for bottom (circles) and surface (triangles) samples, per day and per research vessel, coloured depending on the current velocity during sampling. Lines and grey shaded area represent a loess smoother to indicate trends in the data. (B) Distribution of Chl a concentrations per day and per research vessel, grouped by the current direction while sampling in northward (yellow), near 0 (green, -0.2 – 0.2 m s^{-1}), and southward (purple) flowing currents. Black lines in point cloud indicate 0.25 to 0.75 quantile, with the mean indicated as a black diamond.

d. Coupled variability and interpretation

Figures 49-51 collectively show that tidal transport and large-scale hydrodynamics control most of the variability in suspended matter and Chlorophyll *a* concentrations. Our data showed that the Scheldt river outflow has a significant effect on the observations during our sampling campaign. While SPM concentrations peaked within the OWF, this pattern largely aligns with the regional gradient rather than representing a strong turbine-related effect. The OWF may enhance local mixing and particle resuspension, but these influences are small compared with the dominant background of tidally driven exchange.

A residual northward coastal jet likely carried particle- and pigment-rich Scheldt plume waters past the OWF during flood tides, while ebb flows brought clearer offshore water in the opposite direction. This alternating advection, combined with the generally mixed vertical structure, explains much of the spatial and temporal variability in both SPM and Chlorophyll *a*.

e. Recommendation

We recommend the **development of (semi-)automated water column monitoring techniques**, to supplement the limited observations of this study with year-round data.

4.8 Spatial upscaling: modelling work

As a first note, we have to stress that the overall impact on the ecosystem at the considered scales is small, which is to be associated with the infrastructure scenario and the limited time scale of the simulations (one year). To give a broad sense of scaling, consider that a water column underlying a grid cell of our domain has a volume of m³ (500 m x 500 m x 20 m). A cell containing a turbine involves 200 m² of submerged hard substrate surfaces (2 x 4 m x 8 m). Given a biofouling density biomass of 1000 g.dw m^{-2} and an average clearance rate of 0.02 m³ $g.dw^{-1}$ d^{-1}, this amounts to a daily "cleared" volume of water of 4000 m³, or three orders of magnitude smaller than the said water column. In the upper 8 m of the water column, this volume corresponds to a cylinder extending 100m around the turbine, which provides an impression of the spatial scales at which effects can be observed in-situ in the water column. Of course, this volume is affected by tides and the effect induced by several turbines adds up. The spatial scale of the effect on the benthic layer is further constrained by the advection and sinking of the faecal pellets, as detailed below. Although small in amplitude, our results illustrate important mechanisms at play when considering the upscaling of the local effects induced by offshore infrastructure.

a. Pelagic variables

Phytoplankton groups are consumed by filtration in the OWF area, but their growth is supported by the nutrients emitted by the fouling fauna (Fig. 52).

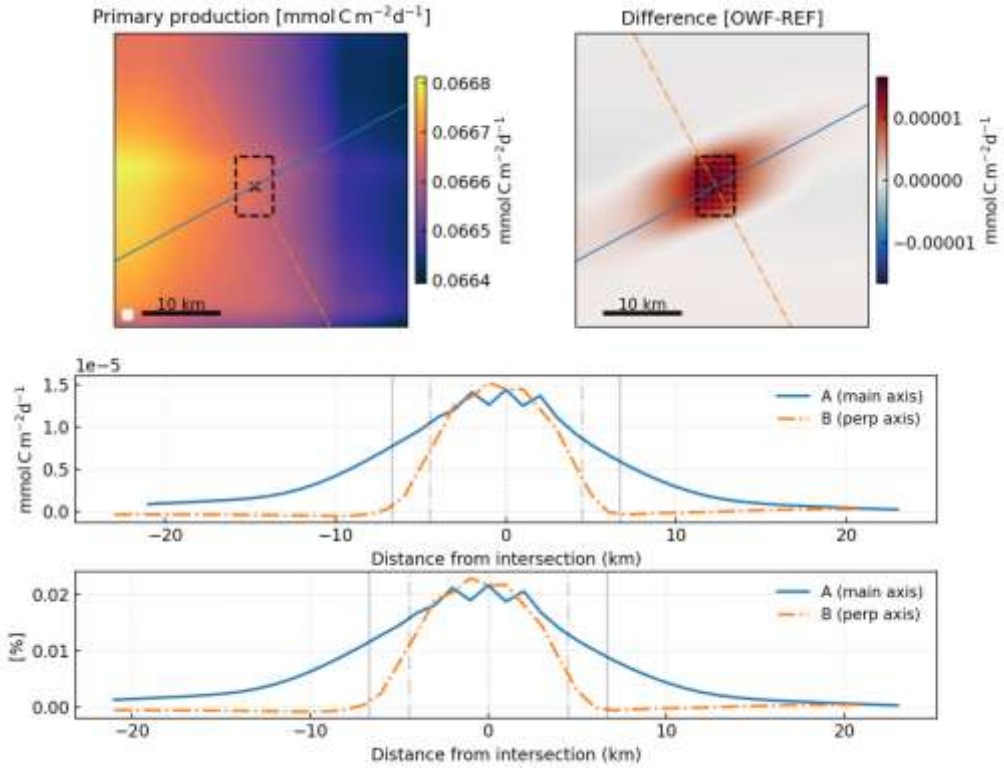

Figure 52. Time averaged primary production: (Upper panels) Absolute values for the OWF scenario and difference induced by the OWF scenario w.r.t the reference run. The transects depict the major and minor axes of the values, tidal ellipse. (Lower panels) Difference induced by the OWF scenario, in absolute and relative along the transects.

The spatial imprint of the OWF impact on phytoplankton biomass thus depicts a region of local reduction around the OWF, with an average radius of 7km (Fig. 53). Noteworthy, a local phytoplankton biomass increase can be seen at the edge of the central reduction zone, suggesting a central origin of the growth enhancing driver. In this simulation this local maximum is located at about 2 km offshore of the OWF in the lee side along the minor tidal axis, which most likely results from a balance between the residual flows and the ecological processes. It is indeed assumed in our model that the part of organic matter ingested by the bivalves that is not excreted in the form of faecal pellets is rapidly digested and returned in dissolved form to the water column (which is in line with the static biomass assumption). This release of nutrients as a source of enhanced primary production induces a non-linear response of the ecosystem to the OWF perturbation.

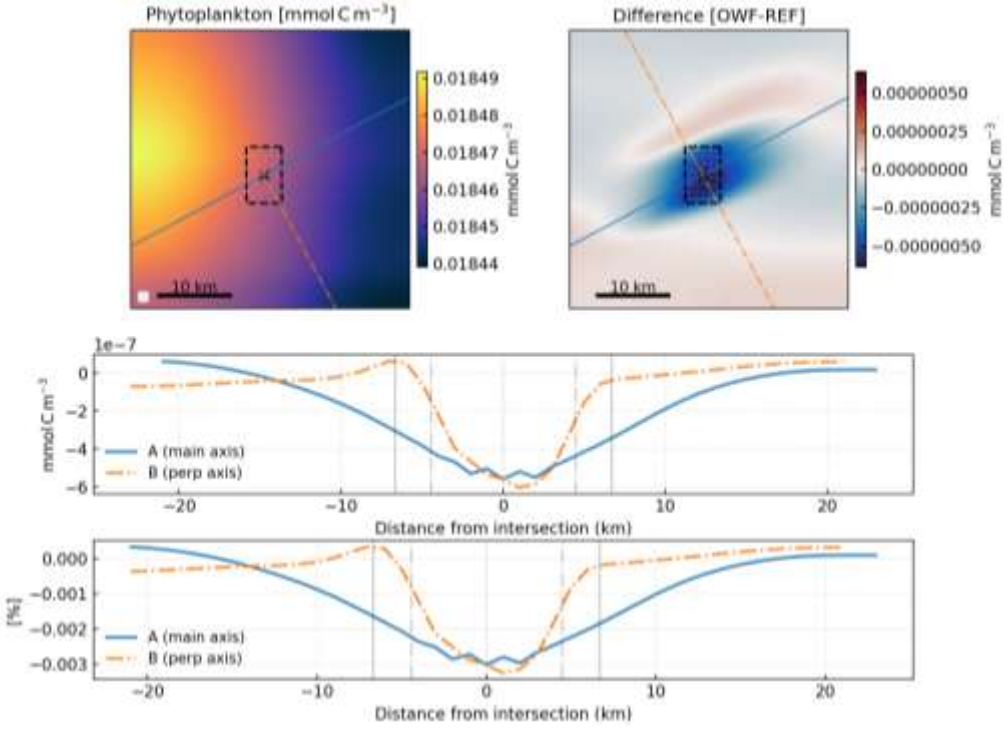

Figure 53. Time averaged phytoplankton biomass: (Upper panels) Absolute values for the OWF scenario and difference induced by the OWF scenario w.r.t the reference run. The transects depict the major and minor axes of the tidal ellipse. (Lower panels) Difference induced by the OWF scenario, in absolute and relative values, along the transects.

Zooplankton is consumed by filtration, and seems unable to benefit from the enhanced primary production at those scales (Fig. 54). The diminution is more in the lee side along the minor axis, which can also contribute to explain the patterns observed for phytoplankton by means of reduced grazing pressure.

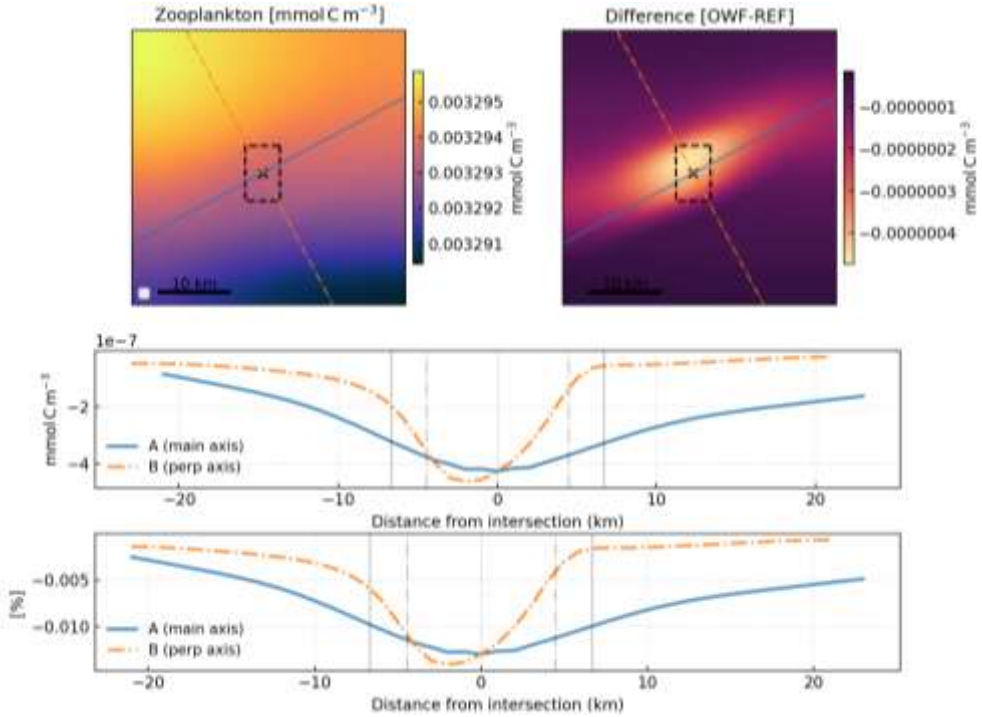

Figure 54. Time averaged zooplankton biomass: (Upper panels) Absolute values for the OWF scenario and difference induced by the OWF scenario w.r.t the reference run. The transects depict the major and minor axes of the tidal ellipse. (Lower panels) Difference induced by the OWF scenario, in absolute and relative values, along the transects.

A pattern similar to that of zooplankton characterizes the imprints of particulate organic matter pelagic stocks (not shown) : reduction in a tidal ellipse around the OWF area with a slight persistence in the lee side. Before proceeding further with the fate of particulate organic matter (POM), a few model specifications should be detailed. Both labile and semi-labile POM pools (POM_{fast} and POM_{slow}) have the same sinking velocity of 2 m d^{-1}. The lability of plankton-based detrital material is set by its repartition between and , which is set upon production by lysis to 90% and 10%, respectively. The faecal pellets differ from plankton-based detritus by two aspects. First, their sinking velocity is much faster, about 400 m d^{-1} (Fig. 55). Second, their lability is considered to be lower, with a repartition, upon deposition of 20% and 80%, for and , respectively.

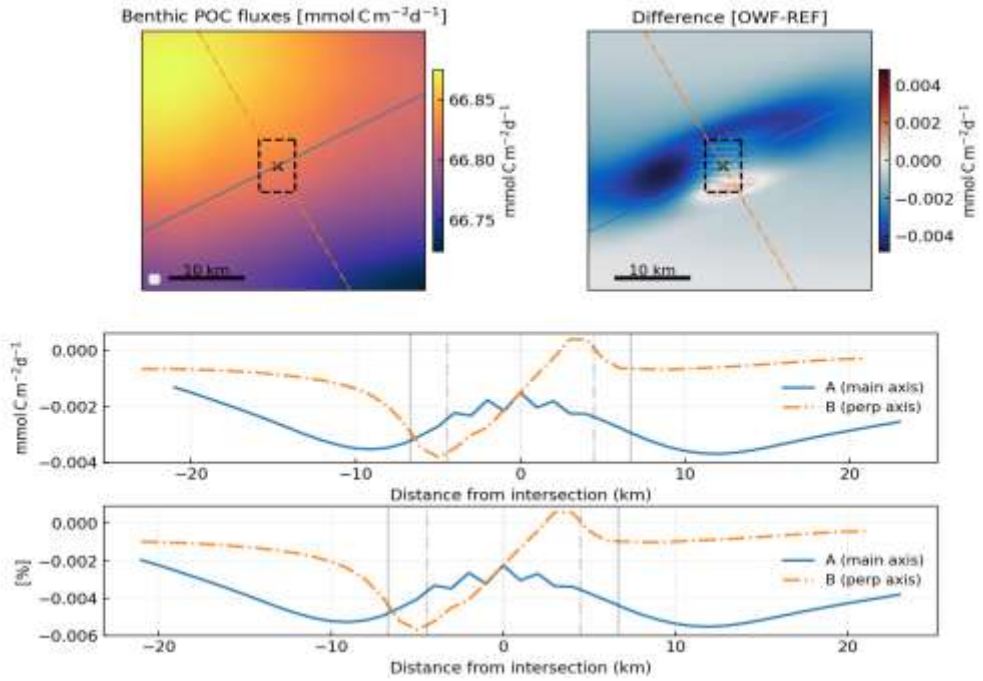

Figure 55. Time averaged particulate organic matter deposition: (Upper panels) Absolute values for the OWF scenario and difference induced by the OWF scenario w.r.t the reference run. The transects depict the major and minor axes of the tidal ellipse. (Lower panels) Difference induced by the OWF scenario, in absolute and relative values, along the transects.

The spatial imprints of POM deposition depicted in figure 56 includes both plankton-based material and faecal pellets. It thus combines a general reduction over an elliptic area scaling around 30 by 15 km and centred on the OWF, with an increase of deposit within the OWF. This corresponds to the deposit of faecal pellets) which is restricted to the OWF along the minor axis of the tidal ellipse, and extends at about 10km away from the OWF along the major axis. The difference in settling velocity between plankton-based detritus and faecal pellets results in a small spatial shift to the seafloor imprints of these phenomena. The “reduction” ellipse associated with plankton-based material (about 10 days to reach the seafloor) is slightly displaced northwest with the residual circulation, while faecal pellets sink in about an hour. This spatial shift likely explains the local maximum in carbon deposition southeast of the OWF domain.

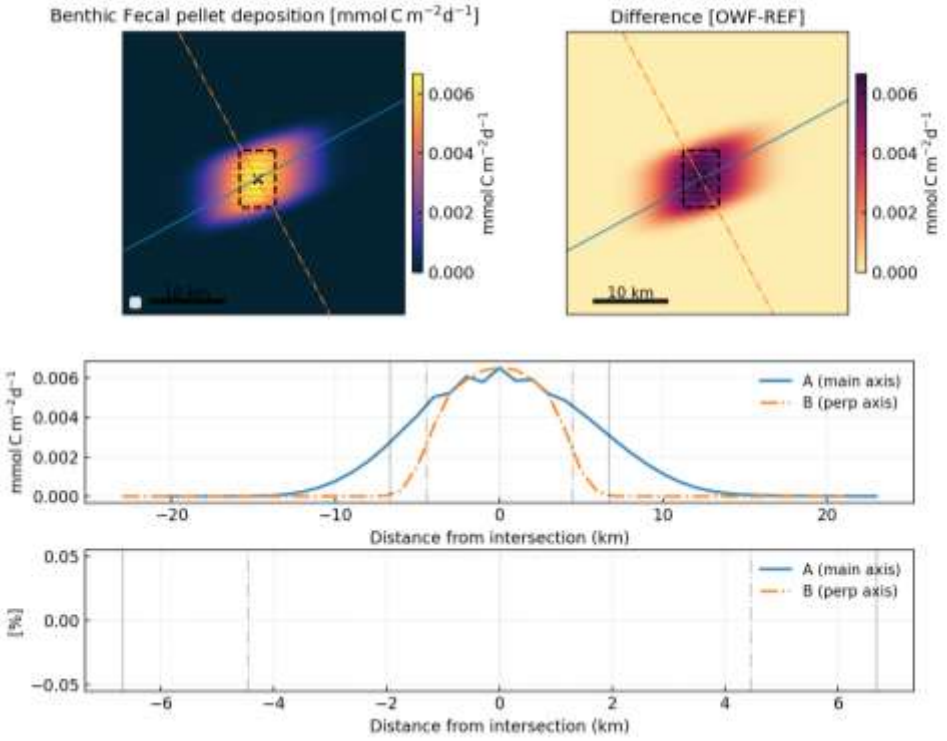

Figure 56. Time averaged fecal pellets deposition: (Upper panels) Absolute values for the OWF scenario and difference induced by the OWF scenario w.r.t the reference run. The transects depict the major and minor axes of the tidal ellipse. (Lower panels) Difference induced by the OWF scenario, in absolute and relative values, along the transects.

Finally, OWF impacts on benthic carbon stock, at the considered annual scale, proceed from the spatial pattern of deposition (Fig. 57). It should be noticed that the amplitude of the relative difference induced by the OWF scenario is lower on the benthic carbon stock than it is on the deposition fluxes. This relationship is indeed modulated by the alteration of the POM composition, from plankton-based material to faecal pellets, and expressed here by the relative proportions between the and pools. By weighting their respective mineralisation rates in these proportions, we can obtain an averaged mineralisation rate (Fig. 58) and illustrate the impact of the OWF scenario.

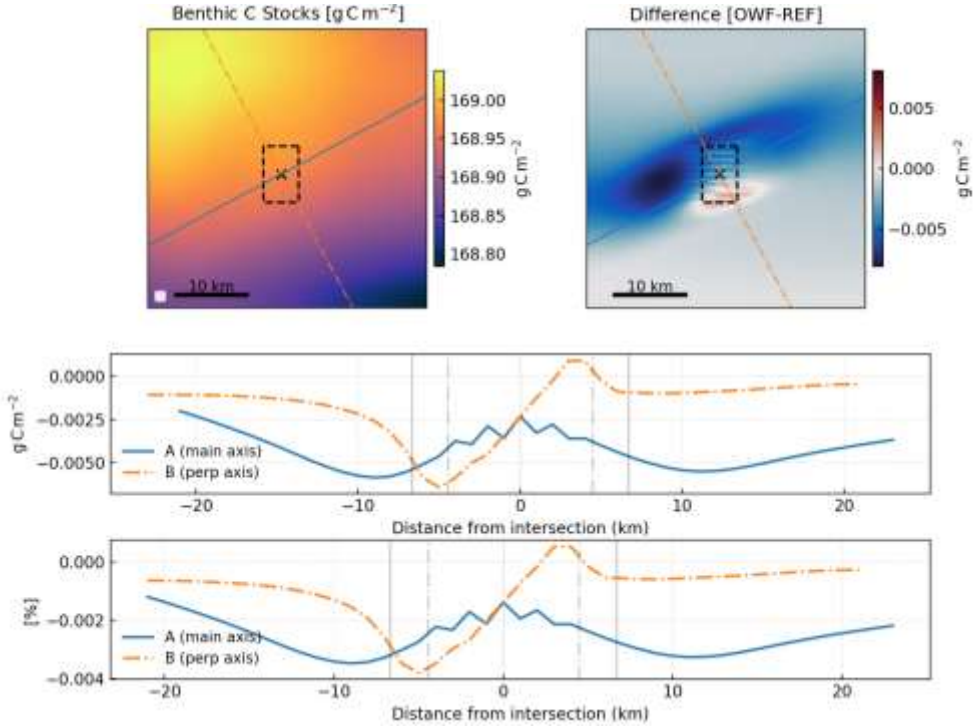

Figure 57. Time averaged benthic carbon stocks (last 50 days of the simulation): (Upper panels) Absolute values for the OWF scenario and difference induced by the OWF scenario w.r.t the reference run. The transects depict the major and minor axes of the tidal ellipse. (Lower panels) Difference induced by the OWF scenario, in absolute and relative values, along the transects.

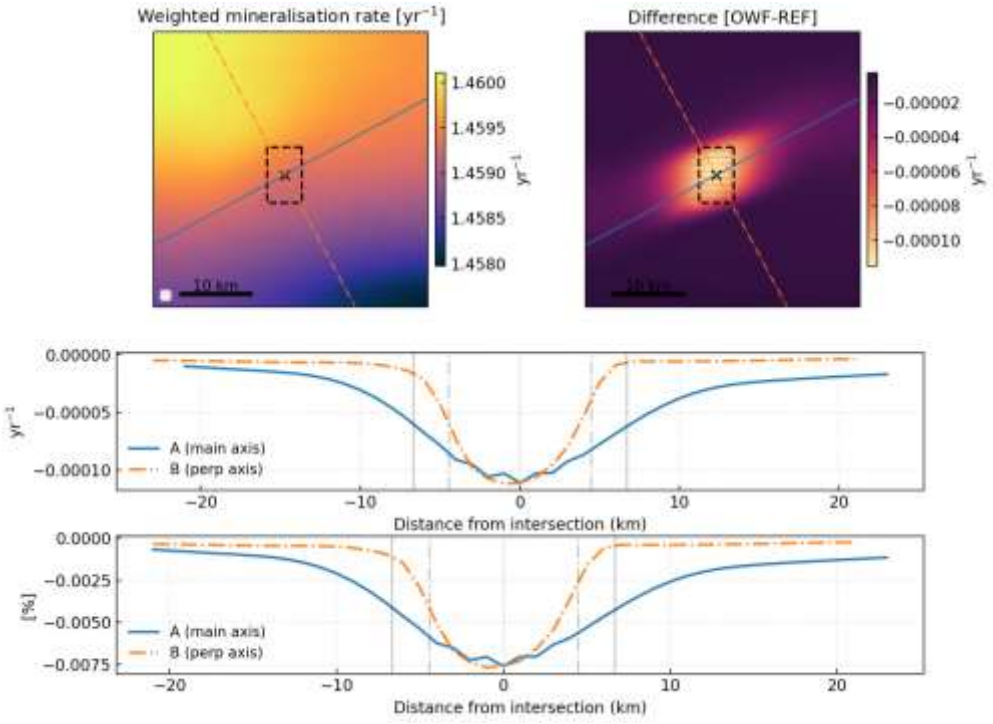

Figure 58. Time averaged benthic mineralisation rate (last 50 days of the simulation): (Upper panels) Absolute values for the OWF scenario and difference induced by the OWF scenario w.r.t the reference run. The transects depict the major and minor axes of the tidal ellipse. (Lower panels) Difference induced by the OWF scenario, in absolute and relative values, along the transects.

5. DISSEMINATION AND VALORISATION

Dissemination and valorisation activities were undertaken throughout the project with the goal of ensuring that OUTFLOW results reached both expert and non-expert audiences, contributed to international science, and strengthened the involvement of the OUTFLOW research teams in OWF research initiatives. Our approach combined targeted communication to the general public with focused exchanges within the scientific community.

Dissemination to the Public at Large

The wider public was engaged through easy accessible communication channels with high visibility to improve societal understanding of marine ecosystem effects of OWF deployment. Key messages and project outputs were shared via the official websites of the Royal Belgian Institute of Natural Sciences (RBINS), LinkedIn, and shared with the EMBRC-BE dissemination platforms. The food-web related components of the project gained significant public attention, culminating in a primetime RTBF television interview (Quel temps pour la planète) with OUTFLOW scientist Ulrike Braeckman (https://www.rtbf.be/article/sous-les-eoliennes-offshore-la-biodiversite-a-trouve-un-refuge-11562681) .

The project also reached a broad European audience through two documentary features. One documentary (Les éoliennes en mer, quelle cohabitation avec la nature ?) was produced for ARTE Europe where it remains accessible through their YouTube channel (https://www.youtube.com/watch?v=frm7rnlAa2U). A second one appeared on France 2 - Envoyé Social). As such, the OUTFLOW research was widely opened to an international audience.

The OUTFLOW project results were also presented during an interview from The North Sea Foundation with Ulrike Braeckman, following her participation in the expert group on ecosystem effects of offshore wind and policy in Zandvoort (NL) in May 2024. (https://www.noordzee.nl/interview-met-ulrike-braeckman-de-impact-van-offshore-windparken-op-mariene-ecosystemen/).

In addition, the project contributed to Ocean Literacy through structured teaching activities. These included a lecture delivered to the BEST community in September 2025 and two invited lectures at the University of Antwerp, which contributed to developing marine science awareness among students and early-career researchers.

Scientific Dissemination and Knowledge Valorisation

The project extensively shared its results with the scientific community through conference presentations, scientific networking, and peer-reviewed publications. In total, the OUTFLOW consortium produced **25 scientific contributions** at national and international conferences and symposia. Additionally, **3 scientific papers were published**, while **a considerable amount of manuscripts and a PhD are planned for** ensuring long-term valorisation of the project's research outputs.

A key component of valorisation consisted of using results and methodological insights from this project to enable scientific outflow into other initiatives. Knowledge developed here contributed directly to attracting additional international l funding for 4 projects:

-NYSERDA – Benthic Change (USA)

-NESTORE (France)

-EcoSTAR (UK)

-INSITE (UK)

These collaborations increased the impact of our research by enabling its application in broader geographic and methodological contexts.
Furthermore, scientific findings and data generated within this project facilitated new international collaborations, including the NWO-funded **FOOTPRINT project in the Netherlands**, highlighting the OUTFLOW funding and research as a catalyst for cross-border research synergies.

International Representation

The project significantly strengthened Belgium's scientific presence in international expert groups, allowing Belgian researchers to contribute to high-level advisory initiatives. Notably, project team members participated actively in:

- ICES Working Group on Marine Benthal Renewable Energy Developments.
- Workshop to compile evidence on the impacts of offshore renewable energy on fisheries and marine ecosystems (WKCOMPORE)
- ICES Workshop on Offshore Monitoring Optimization (WKOMO)
- Expert group on offshore wind energy ecosystem effects & policy, organised by The North Sea Foundation (NL)
-

6. PUBLICATIONS

Peer reviewed papers

We list three papers here that are currently published or in prep. Currently, PhD student Esther Cepeda Gamella is planning her PhD (at least 3 additional papers to be expected) and the upscaling work will be integrated in at least 2 papers, covering the field work at the one hand, and the modelling work at the other hand.

1. De Borger, E., van Oevelen, D., Mavraki, N, De Backer, A., Braeckman, U., Vanaverbeke, J. Offshore wind farms modify coastal food web dynamics by enhancing suspension feeder pathways. *Commun Earth Environ* **6**, 330 (2025). https://doi.org/10.1038/s43247-025-02253-w

2. Hendriks E, Langedock K, van Duren LA, Vanaverbeke J, Boone W, Soetaert K (2025) The impact of offshore wind turbine foundations on local hydrodynamics and stratification in the Southern North Sea. Front Mar Sci 12.
3. Lefaible N, Jammar C, Vanaverbeke J, Moens T, Van Haelst S, Norro A, Degraer S, Braeckman U. (2025) Laying out the foundations: Assessing the spatial extent and drivers of offshore wind turbine artificial reef effects on soft sediments. Journal of Sea Research:102631. https://doi.org/10.1016/j.seares.2025.102631

Oral presentations

1. Braeckman U, De Borger E, Vanaverbeke J (2024) Effects of OWFs on marine biodiversity and food webs. Expert Session The North Sea Foundation, Zandvoort (NL) 14/05/2024. INVITED
2. Braeckman U, Vanaverbeke J, De Borger E, Reynes Cardona A et al. (2024) Food web modelling can help linking benthos with higher trophic levels. 8 November 2024, Newport, USA, INVITED
3. Braeckman U, De Borger E, Cepeda Gamela E, Bodé S, Boeckx P, Van den Eynde D, Capet A, Lacroix G, Vanaverbeke J (2024). Quantifying the contribution of fouling fauna to the local carbon budget of an offshore wind farm. ECODAM Seminar RBINS, 19/11/2025
4. Braeckman U, Vanaverbeke J, Buyse J, Degraer S (2024) 30 years effects of OWFs on benthos and fish. Conference on Wind and Wildlife, Montpellier (F), 08/09/2025. INVITED
5. Braeckman U, De Borger E, Reynes Cardona A, Vanaverbeke J et al. (2025) Effects of OWF on marine biodiversity, carbon and nutrient cycling and food webs. OWF research networking event, Ghent University, 07/10/2025. INVITED
6. Cepeda, E., Bodé, S., Boeckx, P., Braeckman, U., Lizaga, I., & Vanaverbeke, J. Towards fouling fauna fingerprinting: What is their contribution to the marine organic matter pool of an offshore wind farm? JESIUM 2022, Kuopio, Finland, 13/08/2022.
7. Cepeda, E., Bodé, S., Boeckx, P., Braeckman, U., Lizaga, I., & Vanaverbeke, J. Determining the contribution of fouling fauna to the marine organic matter pool of offshore wind farms. VLIZ Marine Science Day, Oostende, Belgium, 01/03/2023.
8. Cepeda, E., Bodé, S., Boeckx, P., Braeckman, U., Lizaga, I., & Vanaverbeke, J. Use of compound-specific stable isotope analysis of amino acids to estimate the contribution of

fouling fauna to the marine organic matter pool in offshore wind farms. BASIS Symposium, Ghent, Belgium, 21/04/2023.

9. Cepeda, E., Bodé, S., Boeckx, P., Braeckman, U., Lizaga, I., & Vanaverbeke, J. Stable isotope fingerprinting through amino acid content in faecal pellets of fouling fauna from offshore wind farms. ASLO Aquatic Sciences Meeting, Palma de Mallorca, Spain, 05/06/2023.
10. Cepeda, E., Bodé, S., Boeckx, P., Braeckman, U., Lizaga, I., & Vanaverbeke, J. Towards assessing fouling fauna contribution to the organic matter pool of an offshore wind farm by their faecal pellet production. SIME Conference, Glasgow, UK, 27/06/2023.
11. Cepeda, E., Bodé, S., Boeckx, P., Braeckman, U., Lizaga, I., & Vanaverbeke, J. A fingerprinting approach to unravel the contributions to the organic matter pool at an offshore wind farm. ICES-ASC, Bilbao, Spain, 13/09/2023.
12. Cepeda, E., Bodé, S., Boeckx, P., Braeckman, U., Lizaga, I., & Vanaverbeke, J. INSITE-OUTFLOW: Quantifying the contribution of fouling fauna to the local carbon budget of an offshore wind farm. INSITE PhD Cohort Meeting, Aberdeen, UK, 25/01/2024.
13. Cepeda, E., Bodé, S., Boeckx, P., Braeckman, U., Lizaga, I., & Vanaverbeke, J. Faecal pellets as a carbon source: Unravelling their fate in offshore wind farms. MarBiol Symposium, Ghent, Belgium, 02/02/2024.
14. Cepeda, E., Bodé, S., Boeckx, P., Braeckman, U., Lizaga, I., & Vanaverbeke, J. Modelling the origin of faecal pellets: First steps towards biodeposit quantification in offshore wind farm ecosystems. MarBiol Symposium, Ghent, Belgium, 09/05/2025.
15. De Borger, E., et al. “Enhanced food web productivity after construction of an offshore wind farm in a shallow coastal sea”. (2024) ICES – Annual Science Conference. Gateshead
16. Hendriks E, Langedock K, Van averbeke J, Braeckman U, van Duren L, Herman P. Near-field measurements around offshore wind turbines show how they enhance hydrodynamics in their direct environment. ASLO Aquatic Science Meeting: Resilience and Recovery in Aquatic Systems, Palma de Mallorca, Spain 4-9 June 2023
17. Hendriks, E.; Langedock, K.; van Duren, L.; Vanaverbeke, J.; Boone, W.; Soetaert, K. (2024). Near-field measurements around offshore wind turbines show how they enhance hydrodynamics in their direct environment. EGU General Assembly, Vienna, Austria, 14-19 April 2024
18. Vanaverbeke J, Coolen J, Braeckman U, Danheim J, Degraer S et al. Offshore wind farms – so what? Symposium: From data to decisions: enhancing offshore wind farm ecosystems insights through data sharing. 8 November 2024, Newport,USA, INVITED
19. Vanaverbeke J, Van Maele TM, Degraer S. Taking into account biodiversity aspects of decommissioning of marine offshore wind farms. BIOWIND – Interregional workshop on sustainable approaches to wind turbine decommissioning. Leuven, 19 June 2024.
20. Vanaverbeke J, De Borger E, Braeckman U. Towards assessing the potential for carbon accumulation in offshore wind farm sediments at the Belgian part of the North Sea. ICES WKFISHCARBON, Online Workshop 24/4/2024

Poster presentations

1. Cepeda, E., Bodé, S., Boeckx, P., Braeckman, U., Lizaga, I., & Vanaverbeke, J. *How do faecal pellets from fouling fauna contribute to the marine organic matter pool in offshore wind farms?* VLIZ Marine Science Day, Online event, 02/03/2022.

2. Cepeda, E., Bodé, S., Boeckx, P., Braeckman, U., Lizaga, I., & Vanaverbeke, J. *Towards estimating the contribution of fouling fauna to the marine organic matter pool in offshore wind farms.* OD-Nature Day, Royal Belgian Institute of Natural Sciences, Belgium, 01/06/2022.
3. Cepeda, E., Bodé, S., Boeckx, P., Braeckman, U., Lizaga, I., & Vanaverbeke, J. *First steps to assess faecal pellet contribution from fouling fauna to the organic matter pool of an offshore wind farm.* SIME Conference, Glasgow, UK, 28/06/2023.
4. Cepeda, E., Bodé, S., Boeckx, P., Lizaga, I., Vanaverbeke, J., & Braeckman, U. *Tracking labelled faecal pellets and their effect on carbon dynamics in offshore wind farm sediments.* VLIZ Marine Science Day, Oostende, Belgium, 06/03/2024.

7. ACKNOWLEDGEMENTS

We would like to acknowledge BELSPO (contract B2/212/P1/OUTFLOW) for funding this project. We thank the crews of the scientific vessels RV Simon Stevin (VLIZ), RV Belgica, and RV Pelagia for their assistance during the collection of samples. The research could not have been completed without the Belgian Occupational Scientific Diving Team and the VLIZ Scientific Diving Team which operate as services provided by EMBRC Belgium. Francesca Passotti (UGent) joined the diving team upon request. *The research leading to results presented in this publication was carried out with infrastructure funded by **EMBRC Belgium** - FWO international research infrastructure I001621N.* PhD student Esther Cepeda Gamella was partly financed through the UK-INSITE programme. We sincerely thank the members of the Follow-Up Committee for their constructive comments during the course of the project.

8. REFERENCES

Ait Ballagh, F. E., Rabouille, C., Andrieux-Loyer, F., Soetaert, K., Elkalay, K., & Khalil, K. (2020). Spatio-temporal dynamics of sedimentary phosphorus along two temperate eutrophic estuaries: A data-modelling approach. *Continental Shelf Research, 193*, 104037. https://doi.org/10.1016/j.csr.2019.104037

Arndt, S., Jørgensen, B. B., LaRowe, D. E., Middelburg, J. J., Pancost, R. D., & Regnier, P. (2013). Quantifying the degradation of organic matter in marine sediments: A review and synthesis. *Earth-Science Reviews, 123*, 53–86. https://doi.org/10.1016/j.earscirev.2013.02.008

Belcher, A., Manno, C., Ward, P., Henson, S. A., Sanders, R., & Tarling, G. A. (2017). Copepod faecal pellet transfer through the meso- and bathypelagic layers in the Southern Ocean in spring. *Biogeosciences, 14*, 1511–1525.

BISAR database; Dannheim, J., Kloss, P., Vanaverbeke, J., … Coolen, J. W. P. (2025). Biodiversity Information of benthic Species at ARtificial structures – BISAR. *Scientific Data, 12*, 604.

Buchanan, J. B. (1984). In N. A. Holmes & A. D. McIntyre (Eds.), *Sediment Analysis* (2nd ed.). Blackwell Scientific Publications.

Buyse, J., Hostens, K., Degraer, S., De Troch, M., & De Backer, A. (2022). Increased food availability at offshore wind farms affects trophic ecology of plaice *Pleuronectes platessa*. *Science of The Total Environment*, 160730.

Chikaraishi, Y., Kashiyama, Y., Ogawa, N. O., Kitazato, H., & Ohkouchi, N. (2007). Metabolic control of nitrogen isotope composition of amino acids in macroalgae and gastropods: Implications for aquatic food web studies. *Marine Ecology Progress Series, 342*, 85–90. https://doi.org/10.3354/meps342085

Coates, D. A., Deschutter, Y., Vincx, M., & Vanaverbeke, J. (2014). Enrichment and shifts in macrobenthic assemblages in an offshore wind farm area in the Belgian part of the North Sea. *Marine Environmental Research, 95*, 1–2.

Coolen, J. W. P., Vanaverbeke, J., Dannheim, J., Garcia, C., Birchenough, S. N. R., Krone, R., & Beermann, J. (2022). Generalized changes of benthic communities after construction of wind farms in the southern North Sea. *Journal of Environmental Management, 315*, 115173.

Daewel, U., Akhtar, N., Christiansen, N., & Schrum, C. (2022). Offshore wind farms are projected to impact primary production and bottom water deoxygenation in the North Sea. *Communications Earth & Environment, 3*, 1–8.

Dannheim, J., Beermann, J., Coolen, J. W. P., Vanaverbeke, J., … Krone, R. (2025). Offshore wind turbines constitute benthic secondary production hotspots. *Journal of Environmental Management, 393*, 126922.

De Borger, E., Ivanov, E., Capet, A., Braeckman, U., Vanaverbeke, J., Grégoire, M., & Soetaert, K. (2021). Offshore Windfarm Footprint of Sediment Organic Matter Mineralization Processes. *Frontiers in Marine Science, 8*

De Borger, E., van Oevelen, D., Mavraki, N., … Vanaverbeke, J. (2025).
Offshore wind farms modify coastal food web dynamics by enhancing suspension feeder pathways. *Communications Earth & Environment, 6*(1), 1–16. https://doi.org/10.1038/s43247-025-02253-w

Degraer, S., Carey, D., Coolen, J., Hutchison, Z., Kerckhof, F., Rumes, B., & Vanaverbeke, J. (2020). Offshore Wind Farm Artificial Reefs Affect Ecosystem Structure and Functioning: A Synthesis. *Oceanography, 33*, 48–57.

De Mesel, I., Kerckhof, F., Norro, A., Rumes, B., & Degraer, S. (2015). Succession and seasonal dynamics of epifauna on wind turbine foundations. *Hydrobiologia, 756*. https://doi.org/10.1007/s10750-014-2157-1

Denis, P., Legrand, S., Capet, A., Ong, E. Z., & Vanaverbeke, J. (2025). Maps of faecal pellet deposition patterns around conceptual marine PV installations. *EcoMPV project report*.

Dickens, G. R., Koelling, M., Smith, D. C., Schnieders, L., & IODP Expedition 302 Scientists. (2007). Rhizon sampling of pore waters on scientific drilling expeditions. *Scientific Drilling, 4*, 22–25. https://doi.org/10.2204/iodp.sd.4.08.2007

Frontier, N., Marlow, J., Giles, A., Morley, S. A., Clark, M. S., & Peck, L. S. (2024). Growth and ecophysiology of two Antarctic benthic predators. *Journal of Experimental Marine Biology and Ecology, 579*, 152045.

Gogina, M., Zettler, A., & Zettler, M. L. (2021). Weight-to-weight conversion factors for benthic macrofauna. *Earth System Science Data Discussions*, 1–6.

Hannides, C. C., Popp, B. N., Landry, M. R., & Graham, B. S. (2009). Quantification of zooplankton trophic position using amino acid $\delta^{15}N$. *Limnology and Oceanography, 54*, 50–61.

Hannides, C. C. S., Popp, B. N., Choy, C. A., & Drazen, J. C. (2013). Midwater zooplankton dynamics from stable isotopes. *Limnology and Oceanography, 58*, 1931–1936.

Hannides, C. C., Popp, B. N., Close, H. G., Wallsgrove, N., Umhau, B., Palmer, E & Drazen, J. C. (2020). Seasonal dynamics of midwater zooplankton. *Progress in Oceanography, 182*, 102266.

HDR (2020). *Benthic and Epifaunal Monitoring During Wind Turbine Installation and Operation at the Block Island Wind Farm*. BOEM report.

Huettel, M., & Rusch, A. (2000). Transport and degradation of phytoplankton in permeable sediments. *Limnology and Oceanography, 45*(3), 534–549.

Jodo, M., Kawamoto, K., Tochimoto, M., & Coverly, S. C. (1992). Determination of nutrients in seawater via segmented-flow analysis. *Journal of Analytical Methods in Chemistry, 14*(5), 964507.

Joiris, C., Billen, G., Lancelot, C., Daro, M.H., Mommaerts, J.P., Bertels, A., Bossicart, M., Nijs, J., Hecq, J. H. (1982). A budget of carbon cycling in the Belgian coastal zone. *Netherlands Journal of Sea Research, 16*, 260–275.

Kerckhof, F., Rumes, B., Jacques, T., Degraer, S., & Norro, A. (2010). Early development of marine biofouling on windmill foundations. *Underwater Technology, 29*, 137–149.

Kerckhof, F., Rumes, B., & Degraer, S. (2019). A decade of fouling succession on Belgian wind turbines. In Degraer et al. (Eds.), *Environmental Impacts of Offshore Wind Farms*.

Kones, J. K., Soetaert, K., van Oevelen, D., & Owino, J. O. (2009). Are network indices robust indicators? *Ecological Modelling, 220*, 370–382.

Lancelot, C., Spitz, Y., Gypens, N., … Billen, G. (2025). Modelling diatom and *Phaeocystis* blooms with MIRO. *Marine Ecology Progress Series, 289*, 63–78.

Latorre, B., Lizaga, I., Gaspar, L., & Navas, A. (2021). Consistency analysis in sediment fingerprinting. *Science of the Total Environment, 789*, 147804.

Lefaible, N., Braeckman, U., Degraer, S., & Moens, T. (2023). A wind of change for soft-sediment infauna. *Marine Environmental Research, 188*, 106009.

Lefaible, N., Jammar, C., Vanaverbeke, J., Moens, T., Van Haelst, S., Norro, A., Degraer, S. & Braeckman, U. (2025). Spatial extent of artificial reef effects. *Journal of Sea Research*, 102631.

Legrand, S. (2024). Permanent alteration of hydrological conditions in the BPNS. *Mariene Strategie Deel 1*.

Legrand, S., De la Vallée, P., Fettweis, M., & Van den Eynde, D. (2018). Hydrographic changes. *Belgische Staat KRMS evaluatie*.

Lizaga, I., Latorre, B., Gaspar, L., & Navas, A. (2018). fingerPro: R package for sediment tracing. https://doi.org/10.5281/zenodo.1402029

Lizaga, I., Latorre, B., Gaspar, L., & Navas, A. (2020a). Consensus ranking to identify dissenting tracers. *Science of the Total Environment, 720*, 137537.

Lizaga, I., Latorre, B., Gaspar, L., & Navas, A. (2020b). FingerPro for sediment provenance. *Water Resources Management, 34*, 3879–3894.

Luyten, P. (Ed.). (2021). *COHERENS v2.12 User Documentation*. RBINS.

Luyten, P. (Ed.). (2025). *COHERENS v3.0.7 User Documentation*. RBINS.

Mavraki, N., De Mesel, I., Degraer, S., Moens, T., & Vanaverbeke, J. (2020a). Functional differences in trophic structure in OWFs. *Marine Environmental Research, 157*, 104868.

Mavraki, N., Degraer, S., & Vanaverbeke, J. (2021). OWFs and the attraction–production hypothesis. *Hydrobiologia, 848*(7), 1639–1657.

Mavraki, N., Degraer, S., Moens, T., & Vanaverbeke, J. (2020b). Organic matter assimilation at wind farms. *ICES Journal of Marine Science, 77*, 2681–2693.

Mavraki, N., Coolen, J. W. P., Kapasakali, D. A., Degraer, S., Vanaverbeke, J., &Beermann, J. (2022). Small suspension feeders drive carbon dynamics. *Marine Environmental Research, 178*, 105664.

Mavraki, N., Bos, O. G., Vlaswinkel, B. M., Roos, P., de & Coolen, J. W. P. (2023). Fouling community composition on floating solar. *Frontiers in Marine Science, 10*, 1223766.

McClelland, J. W., Holl, C. M., & Montoya, J. P. (2003). Low $\delta^{15}N$ of zooplankton linked to N_2 fixation. *Deep Sea Research I, 50*, 849–861.

Møller, E. F., Thor, P., & Nielsen, T. G. (2003). DOC production by *Calanus*. *Marine Ecology Progress Series, 262*, 185–191.

Pinheiro, J., Bates, D., & R Core Team. (2023). *nlme: Linear and Nonlinear Mixed Effects Models*. CRAN.

Popp, B. N., Graham, B. S., Olson, R. J., … Fry, B. (2007). Trophic ecology of yellowfin tuna. In Dawson & Siegwolf (Eds.), *Stable isotopes as indicators of ecological change*, 173–190.

Provoost, P., Braeckman, U., Van Gansbeke, D., Moodley, L., Soetaert, K., Middelburg, J.J. & Vanaverbeke, J. (2013). Modelling benthic oxygen consumption. *Estuarine, Coastal and Shelf Science, 120*, 1–11.

Reubens, J. T., Degraer, S., & Vincx, M. (2014). The ecology of benthopelagic fishes at offshore wind farms: A synthesis of 4 years of research. *Hydrobiologia, 727*, 121–136.

Ricciardi, A., & Bourget, E. (1998). Weight-to-weight conversion of benthic macroinvertebrates. *Marine Ecology Progress Series, 163*, 245–251.

Seeberg-Elverfeldt, J., Schlüter, M., Feseker, T., & Kölling, M. (2005). Rhizon sampling near the sediment–water interface. *Limnology and Oceanography: Methods, 3*, 361–371.

Sistermans, W. C. H., Hummel, H., Engelberts, A., & Markusse, M. M. (2004). *Inventarisatie macrofauna Westerschelde 2004*. NIOO/CEMO.

Slavik, K., Lemmen, C., Zhang, W., Kerimoglu, O., Klingbeil, K., & Wirtz, K. W. (2019). The large-scale impact of offshore wind farm structures on pelagic primary productivity in the southern North Sea. *Hydrobiologia*, 1–19.

Soetaert, K., Herman, P. M. J., & Middelburg, J. J. (1996). A model of early diagenetic processes. *Geochimica et Cosmochimica Acta, 60*, 1019–1040.

Soetaert, K., & van Oevelen, D. (2009). Modelling food web interactions: A guide. *Oceanography, 22*(1), 128–143.

Toussaint, E., De Borger, E., Braeckman, U., De Backer, A., Soetaert, K., & Vanaverbeke, J. (2021). Carbon and nitrogen cycling drivers in North Sea sediments. *Science of The Total Environment, 767*, 144994.

Van den Eynde, D. (2022). Residual currents and transports near the C-Power and Norther wind farms. Institute of Natural Sciences, Brussels, Belgium, 9 pp. Maximum bottom stresses in PE zone. In Degraer et al. (Eds.), *EDEN 2000*.

Van den Eynde, D. (2025). Calculation of deposition of faecal pellets around a wind turbine. Report OUTFLOW/X/DVDE/202512/EN/TR01. Institute of Natural Sciences, Brussels, Belgium, 43 pp.

Van den Eynde, D., Baeye, M., Kint, L., Van Lancker, V., & Luyten, P. (2023). A high-resolution 3D hydrodynamic model for the PE zone. In Degraer et al. (Eds.), *EDEN 2000*.

van Oevelen, D., Van den Meersche, K., Meysman, F. J. R., … Vézina, A. F. (2010). Quantifying food web flows via linear inverse models. *Ecosystems, 13*, 32–45.

Voet, H. E. E., Van Colen, C., & Vanaverbeke, J. (2022). Climate change effects on the ecophysiology and ecological functioning of an offshore wind farm artificial hard substrate community. *Science of The Total Environment, 810*, 152194.

Voet, H. E. E. (2023). *Combined effects of climate change, offshore wind farms and aquaculture on marine ecosystem functioning*. PhD thesis, Ghent University.

Wilson, R. J., Speirs, D. C., Sabatino, A., & Heath, M. R. (2018). A synthetic map of NW European shelf sediments. *Earth System Science Data, 10*, 109–130.

Wijsman, J. W. M., Herman, P. M. J., & Gomoiu, M. (1999). Sediment characteristics and benthic activity in the Black Sea. *Marine Ecology Progress Series, 181*, 25–39.

Wright, S. W., & Mantoura, R. F. C. (1997). Phytoplankton pigments methodology. In Jeffrey et al. (Eds.), *Phytoplankton pigments in oceanography* (p. 661). UNESCO.

Zuur, A. F., Ieno, E. N., Walker, N., Saveliev, A. A., & Smith, G. M. (2009). *Mixed effects models and extensions in ecology with R*. Springer. https://doi.org/10.1007/978-0-387-87458-6